Basic Studies on Persistent Current Compensator for Superconducting Magnet by Use of Linear Type Magnetic Flux Pump

June, 2007

Yoon Do Chung

Contents

List of Figures

List of Tables

Notation

$\boldsymbol{H}$	Magnetic field intensity	[A/m]
H_c	Critical magnetic field intensity	[A/m]
H_{c1}	Lower critical magnetic field intensity of superconductor	[A/m]
H_{c2}	Upper critical magnetic field intensity of superconductor	[A/m]
$\boldsymbol{E}$	Electric field	[V/m]
E_c	Electric field criterion	[V/m]
$\boldsymbol{J}$	Current density	[A/m^2]
J_c	Critical current density	[A/m^2]
$\boldsymbol{J_e}$	Eddy current density	[A/m^2]
$\boldsymbol{J_0}$	Force current density	[A/m^2]
$\mu_0 H_{c1}$	Lower critical magnetic flux density	[T]
$\mu_0 H_{c2}$	Upper critical magnetic flux density	[T]
$\mu_0 H$	Component of the magnetic flux density	[T]
$\mu_0 H_{peak}$	Peak value of magnetic flux density	[T]
$\boldsymbol{B}$	Magnetic flux density	[T]
B_m	Maximum of magnetic flux density by DC bias current	[T]
$\boldsymbol{F}_L$	Lorentz force	[N]
$\boldsymbol{F}_{LC}$	Lorentz force at threshold point	[N]
$\boldsymbol{F}_p$	Pinning force	[N]
μ_0	Magnetic permeability of vacuum	[H/m]
μ_r	Relative permeability	[H/m]
ρ	Resistivity value of normal spot	[Ωm]
T	Absolute temperature	[K]
T_c	Critical temperature	[K]
T_{op}	Operation temperature	[K]
V	Voltage	[V]
Φ	Magnetic flux	[Wb]
Φ_0	Quantized magnetic flux in superconductor	[Wb]
R	Resistance	[Ω]
R_0	Initial resistance of Nb foil	[Ω]
R_n	Resistance of Nb foil after enhancement of normal spot area	[Ω]
I	Current	[A]
I_c	Critical current	[A]

I_{R}	Induced current by normal spot on the Nb foil	[A]
I_{L}	Transport current of load magnet	[A]
I_{n}	Pumped current	[A]
I_0	Initial pumped current	[A]
$\Delta I_{\mathrm{decay}}$	Decreased amount of persistent current decay	[A]
I_{op}	Operating current of load magnet	[A]
I_{DC}	DC bias current of LTMFP	[A]
I_{AC}	AC current for AC coil in LTMFP	[$\mathrm{A_{peak}}$]
I_{DC1}	External DC current for DC bias coil in LTMFP	[A]
I_{DC2}	Heating current source of PCS	[A]
I_{inv}	Inverter output peak current	[A]
I_{rate}	Pumped current rate	[mA/s]
I_{cal}	Calculated pumping current	[A]
I_{mea}	Measured pumping current	[A]
I_{final}	Final calculated pumping current with estimated k value	[A]
I_{target}	Target current value in the feedback control circuit	[A]
I_{load}	Detected current of the load magnet by Hall sensor	[A]
C_{pr}	Pumping current rate in the LTMFP	[mA/s]
k	Enhancement rate of normal spot per frequency	[mm/Hz]
t	Elapsed time	[s]
t_0	Time duration of one cycle operation in LTMFP	[s]
t_{n}	Time duration after nth cycle operation in LTMFP	[s]
t_{md}	Characteristic time of magnetic diffusion in superconductor	[s]
s	Operating time	[s]
f	Driving frequency	[Hz]
f_{t}	Characteristic frequency of magnetic diffusion in superconductor	[Hz]
τ	Time constant	[s]
τ_{p}	Time constant of pumping current in the LTMFP	[s]
w_{a}	Average value of time duration for width of normal spot	[s]
v	Moving velocity of normal spot	[m/s]
v_0	Initial velocity of normal spot	[m/s]
D_{m}	Magnetic diffusivity in superconductor	[$\mathrm{m^2/s}$]
L	Self-inductance of load magnet	[H]
L_{dc}	Self-inductance of DC bias coil	[H]
L_{ac}	Self-inductance of AC coil	[H]
l	Self-inductance of Nb foil	[H]

l_n	Self-inductance of Nb foil after enhancement of normal spot area	[H]
l_sh	Self-inductance of Nb foil by shielding current	[H]
S	Penetrated area by applied magnetic field	[mm^2]
S_n	Penetrated area after enhancement	[mm^2]
S_0	Initial size of normal spot	[mm^2]
w	Width of normal spot	[mm]
w_0	Initial width of normal spot	[mm]
w_n	Enhanced width of normal spot after n^{th} cycle	[mm]
W	Width of superconducting Nb foil	[mm]
h	Length of normal spot	[mm]
z	Thickness of superconducting Nb foil	[mm]
d	Interval between slot and Nb foil in LTMFP	[mm]
g_1	Initial interval between normal spot areas in Nb foil	[mm]
g_2	Interval between normal spots after enhancement of normal spot	[mm]
l_p	Penetrated length by magnetic field in the Nb foil	[mm]
l_t	Total length of the superconducting Nb foil	[mm]
ϕ	Diameter	[mm]
ρ	Resistivity value of normal spot	[Ωm]
σ	Electric conductivity	[S/m]
σ_s	Equivalent electric conductivity	[S/m]
$\sigma_\mathrm{s\_new}$	Approached root value of electric conductivity	[S/m]
$\sigma_\mathrm{s\_old}$	Pre-estimated value of electric conductivity	[S/m]
$\boldsymbol{A}$	Magnetic vector potential	[Wb/m]
φ	Magnetic scalar potential	[A]
$\mathrm{S_{p1}}$	Slow-response superconducting persistent current switch	
$\mathrm{S_{p2}}$, $\mathrm{S_{p3}}$	Fast-response superconducting persistent current switch	
$\mathrm{S_1}$, $\mathrm{S_2}$	On-off switches according to the position of the normal spot in Nb foil	
n	Exponent in the power-law (J-E) relation of superconductor	

Chapter 1 Introduction

1.1 Discovery of Superconductivity

In 1911, Heike Kamerlingh-Onnes discovered that the resistivity of mercury (Hg) drops down to an extremely small value (at least less than 10^{-14} Ωm) at 4.15 K [1]. He named this phenomenon as 'superconductivity'. Furthermore, he and his co-workers also found that some other metals such as lead (Pb) and tin (Sn) are characterized by the abrupt disappearance of electrical resistance at 7.19 and 3.72 K, respectively. These metals, however, easily transit to the normal-conducting state even under smaller magnetic field at 5 mT. These metals are classified as Type I superconductors [2]. Therefore, at that time, the application of such materials in power systems was not realized.

However, the breakthrough for this obstacle was discovered in 1969. R. Hampshire, J. Sutton, and M.T. Taylor developed a transition alloy niobium-titanium (Nb-Ti), which retains the superconducting state until 9.6 K [3]. The technological advantage of this superconducting material is that it can be in the superconducting state at higher magnetic field 10 T at 4.2 K [4]. Followed by this development, from 1973, Nb_3Ge, Nb_3Sn, and Nb_3Al had also been fabricated as thin films. In the case of Nb_3Sn, it can generate higher magnetic fields, e.g., 21 T at 4.2 K without any energy dissipations and retains a superconducting state below 18 K [5]. The aforementioned superconductors are so-called the low temperature superconductor (LTS) in a category of Type II [6], and some of them (Nb-Ti and Nb_3Sn) have been commercialized.

In 1986, the breakthrough for the cooling problem was accomplished when B.G. Bednorz and K.A. Müller discovered that the La-Ba-Cu-O shows the superconducting phenomenon at 30 K. Furthermore, C.W. Chu found that Y-Ba-Cu-O shows a superconducting state at 90 K in 1987 [7]. Followed by these findings, many oxide materials such as Bi-, Tl-, and Hg-systems were found to show the superconducting properties around 100 K [8]. These materials are now classified as high temperature superconductor (HTS) of Type II.

Recently, technological advances have been made for the development of high quality as well as long length HTS wires. These technologies improved high current carrying capability and its good magnetic field dependent. Therefore, many kinds of HTS coils as magnets have been fabricated and studied for the purpose of the realization of high field applications such as Nuclear Magnetic Resonance (NMR) analyzer [9].

1.2 Fundamental Aspects of Superconductor

1.2.1 Zero resistivity

One of the most attractive properties of the superconductor is its zero resistance. When the temperature of the superconductor decreases below its critical temperature T_c, the resistance of the material is diminished. In this case, the dissipationless current can be flowed in the superconductor until the current reaches its critical value.

1.2.2 Meissner effect

Firstly, we consider the perfect conductor that is mentioned in subsection 1.2.1, i.e., zero resistance $R = 0$. If a conductor becomes a perfect one without magnetic field, the magnetic field will be expelled from the conductor by applying the external field. On the contrary, if a conductor becomes the perfect conductor with magnetic field, that field will be retained in the conductor.

However, Meissner and Ochsenfeld found in 1933 that the superconductor always expels the magnetic field from its interior. This is called Meissner effect. The Meissner effect has phenomenologically been explained by the London brothers [10].

1.2.3 Type I and Type II superconductors

The superconducting phase can exist at magnetic fields weaker than the critical magnetic field H_c. The schematic relation between magnetic field H and temperature T of the superconductor is shown in Fig. 1.1.

There exist two types of the superconductor with respect to the magnetic characteristics. Type I superconductors have single critical field, H_c. Whereas, Type II superconductors have two sorts of critical fields, i.e., the lower critical field H_{c1} and the

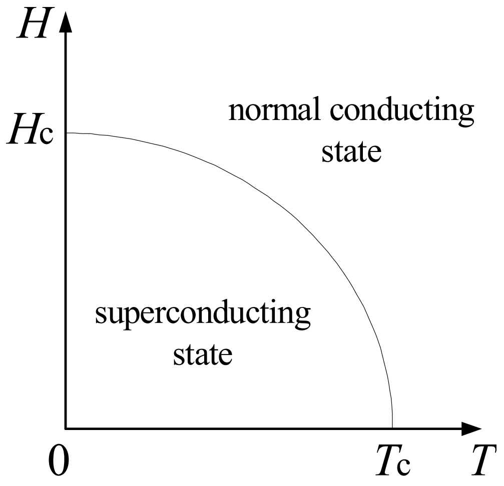

Fig. 1.1 Schematic relation between temperature T and magnetic field H.

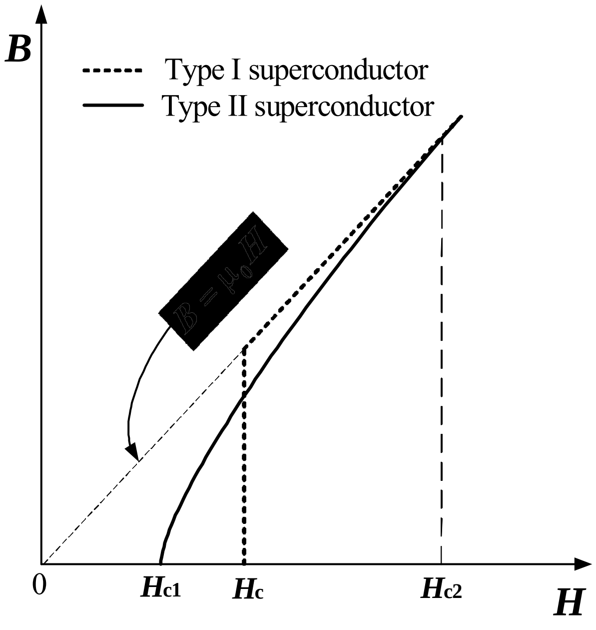

Fig. 1.2 Relation between magnetic flux density B and magnetic field H for Type I and Type II superconductors.

upper critical field H_{c2}. The relations between magnetic flux density $\boldsymbol{B}$ within the superconductor and magnetic field $\boldsymbol{H}$ for Type I and Type II superconductors are schematically shown in Fig. 1.2. The value of H_{c2} in a Type II superconductor is generally larger than that of H_c in a Type I superconductor.

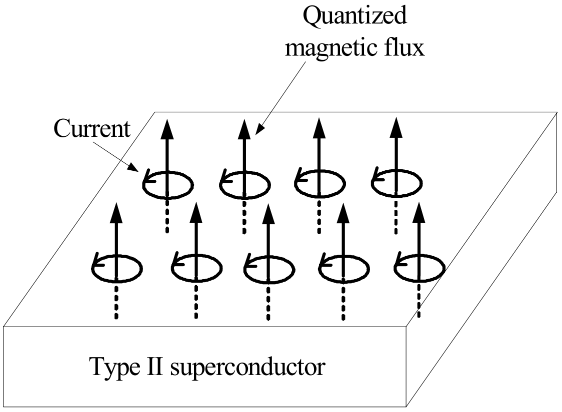

Fig. 1.3 Schematic diagram of the mixed state of Type II superconductor [12].

A Type I superconductor exhibits the Meissner state when $H < H_c$, and transits to normal-conducting state for $H \geq H_c$. The value of H_c in a Type I superconductor is fairly small, and this type of superconductor has not been utilized to power application systems.

A Type II superconductor also expels the entire magnetic field below H_{c1} (Meissner state). However, once the magnetic field exceeds the value of H_{c1}, this type of superconductor no longer expels the entire magnetic field. In this state, the quantized magnetic fluxes at Φ_0 (=2.07×10^{-15} Wb), i.e., fluxoids, penetrate into the superconductor [11]. The schematic diagram of this state is shown in Fig. 1.3. This is called the mixed state and is realized at the field between H_{c1} and H_{c2} [12].

1.2.4 Critical current

In the mixed state, when the transport current (current density $\boldsymbol{J}$) flows in a magnetic field $\boldsymbol{B}$, a Lorentz force $\boldsymbol{F}_\mathrm{L}\left(= \boldsymbol{J} \times \boldsymbol{B}\right)$ acts to move the fluxoids in a direction perpendicular to the current. If no obstacles to this force exist, the fluxoids move freely at the velocity $\boldsymbol{v}$, and then the electric field $\boldsymbol{E}\left(= \boldsymbol{B} \times \boldsymbol{v}\right)$ is generated in the superconductor. In the superconductor, however, the non-superconducting regions such as normal-conducting grains dislocations, etc., exist, and these regions resist the movement of the fluxoids. In other words, the force, which direction is always opposite to that of the Lorentz force, is acted on the fluxoids. In this case, the fluxoids do not move by the transport current, and then the dissipationless (no loss) current can flow. The aforementioned non-superconducting regions are called flux pinning centers, and the corresponding force $\boldsymbol{F}_{\mathrm{p}}$ is called the pinning force. If the Lorentz force exceeds $\boldsymbol{F}_{\mathrm{p}}$, the fluxoids begin to move (flux flow state). At this threshold point, the corresponding Lorentz force $\boldsymbol{F}_{\mathrm{LC}}$ is expressed as,

$$\boldsymbol{F}_{\mathrm{LC}} = \boldsymbol{J}_{\mathrm{c}} \times \boldsymbol{B}, \tag{1.1}$$

where $\left|\boldsymbol{J}_{\mathrm{c}}\right|$ denotes the critical current density (the maximum dissipationless current density), and can be determined by the following relation,

$$\boldsymbol{F}_{\mathrm{P}} = \boldsymbol{F}_{\mathrm{LC}} = \boldsymbol{J}_{\mathrm{c}} \times \boldsymbol{B}. \tag{1.2}$$

The enlargement of $\boldsymbol{J}_{\mathrm{c}}$ (or $\boldsymbol{F}_{\mathrm{p}}$) is one of the most important issues to the power applications [13].

1.2.5 AC loss

As is already mentioned, a superconductor below T_{c} has the ability to pass a current with practically no energy losses. However, this is only true for direct current (DC). Alternating currents (AC) and alternating magnetic fields cause energy dissipation in the superconductor. This energy dissipation is called the AC loss. The AC loss is dissipated as Joule heat in the superconductor, and must be reduced.

The AC losses are categorized as follows: hysteresis loss, eddy current loss, and coupling loss. These AC losses are briefly discussed as follows.

Hysteresis loss

Due to the flux pinning effect, the superconductor shows the hysteretic characteristics by applying the AC current and/or magnetic field. The corresponding energy dissipation is called hysteresis loss.

In addition, a transport current in a superconductor also generates a magnetic field around the superconductor, which is called the self-field. With an alternating transport current, the alternating self-field penetrates into the superconductor. Even if there is no external magnetic field, the variation of the self-field inside the material causes a hysteresis loss, which is called self-field loss [14].

Eddy current loss and coupling loss

In many cases, tape and wire structures are utilized as superconducting materials. In these structures, the normal-conducting sheath material (typically, silver or silver alloy) is attached to the superconducting material. The purposes for the sheath material are the better crystallization of the superconducting phase and the current sharing protection in case of the over current. When an external time-varying magnetic field penetrates into this normal-conducting matrix, this causes the eddy current. Due to the eddy current in the normal-conducting sheath, an ohmic energy dissipation occurs. This is called eddy current loss. Fig. 1.4 shows a cross section of a composite superconductor with superconducting filaments embedded in a normal-conducting matrix. An electric field, which opposes the change in the magnetic field, is induced when the time varying external field is applied. That field drives currents as indicated by the arrows as shown in Fig. 1.4. Induced current flows partly through the superconductor and partly normal-conducting matrix, and then such currents couple the filaments together like a single filament. The driving current is encountered with a resistance along the currents path through the normal-conducting matrix material. This ohmic loss in the normal-conducting matrix is called the coupling loss. The coupling loss can be decreased by applying a twist to the filaments [15], [16].

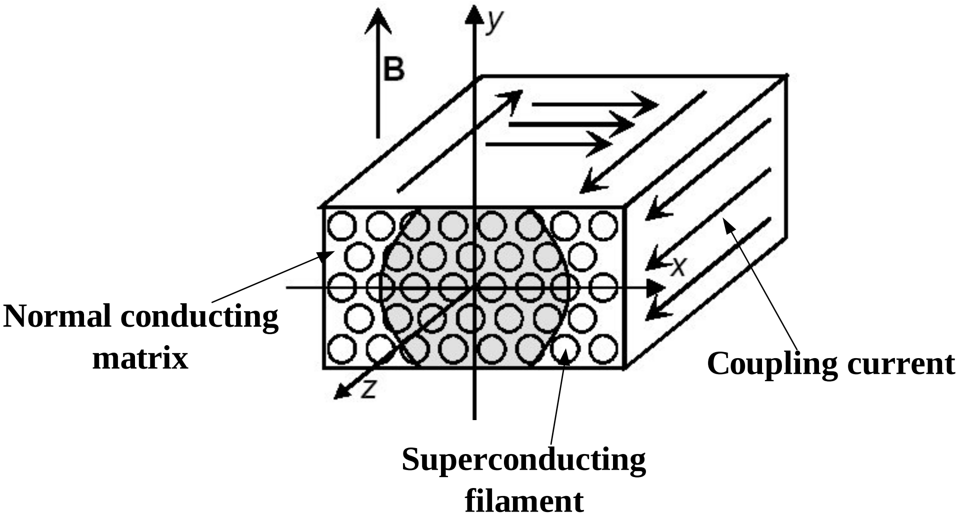

Fig. 1.4 Cross-section of a non-twisted multi-filament superconductor in a changing external field. The induced coupling current transports through the matrix [15].

1.2.6 Category of superconducting materials

There are roughly three categories of superconducting materials, i.e., tape (or wire), bulk, and thin film. The LTS bulk is impossible to be realized due to its thermal instability. The bulk shape is only available for HTS. The shape of thin film is usually utilized for the field of electronics. Actually, the shape of round wire is mostly utilized for LTS power applications because it is very useful for the fabrication of coils or magnets. However, HTS tapes have recently become available. The long length $Bi_2Sr_2Ca_2Cu_3O_x$ (Bi-2223) multifilamentary tape has been commercialized [17]. Further, $Y_1Ba_2Cu_3O_{7-y}$ (Y-123) coated conductor has also been developed as a national project for the next generation of high quality materials [18].

1.2.7 Comparison with LTS and HTS materials

The most distinct differences between LTS and HTS from the point of view of the material property are the critical temperature T_c, and the upper critical magnetic field $\mu_0 H_{c2}$. T_c as well as $\mu_0 H_{c2}$ in HTS (YBCO and BSCCO) is extremely higher compared to that in LTS (NbTi and Nb_3Sn) as shown in Fig. 1.5 (a) [19]. This means that the cooling cost for the HTS material will be dramatically reduced.

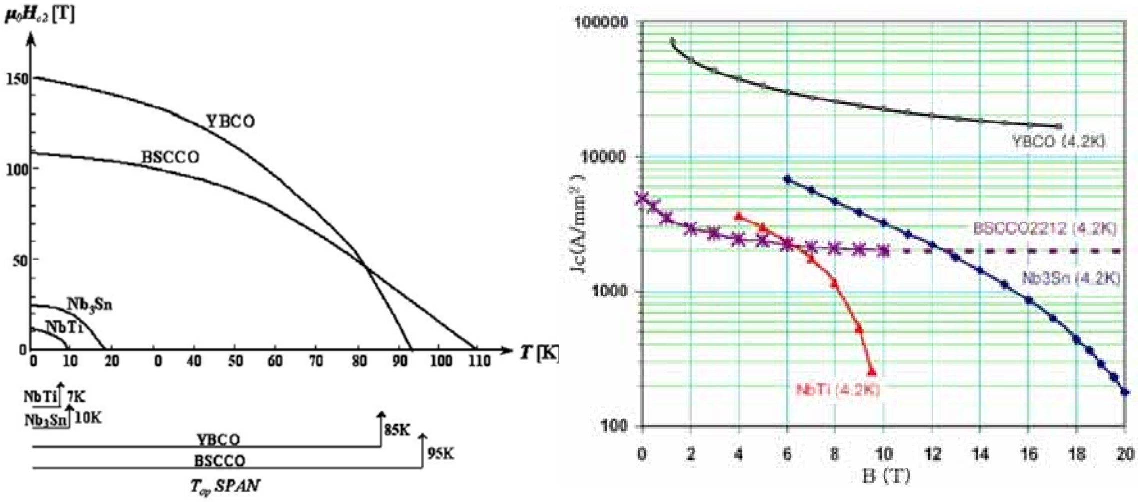

(a) typical upper critical magnetic field $\mu_0 H_{c2}$ versus temperature T plots

(b) critical current density J_c versus magnetic flux density B

Fig. 1.5 Comparison with LTS (Nb-Ti and Nb_3Sn) and HTS (BSCCO and YBCO) [19].

In addition, HTS has high potential for magnets compared to the LTS under the high field condition since HTS has excellent magnetic field dependency of critical current density as shown Fig. 1.5 (b). That means the high field (over 20 T) using HTS insert magnet is available.

Based on the aforementioned characteristics, power application apparatuses such as magnets fabricated using HTS can be promisingly applied. Therefore, a wide temperature range and excellent field dependency of current density can be considered for operation in case of HTS materials. From this reason, the technology of HTS may be used for many application fields in near future [20].

1.3 Development of Superconducting Magnet

1.3.1 Current status of development of power application systems with the use of superconducting magnets

One of the most interesting applications using the superconducting wire is the high field magnet. Especially, the dissipationless (zero resistance) current can flow in the 'closed' superconducting magnet in an ideal case. This operation mode is called "persistent current mode".

LTS wires (Nb-Ti and Nb_3Sn) have already been utilized for a high field magnet with persistent current mode, e.g., magnetically levitated (Maglev) train [21], magnetic resonance imaging (MRI) [22], and nuclear magnetic resonance (NMR) systems [23].

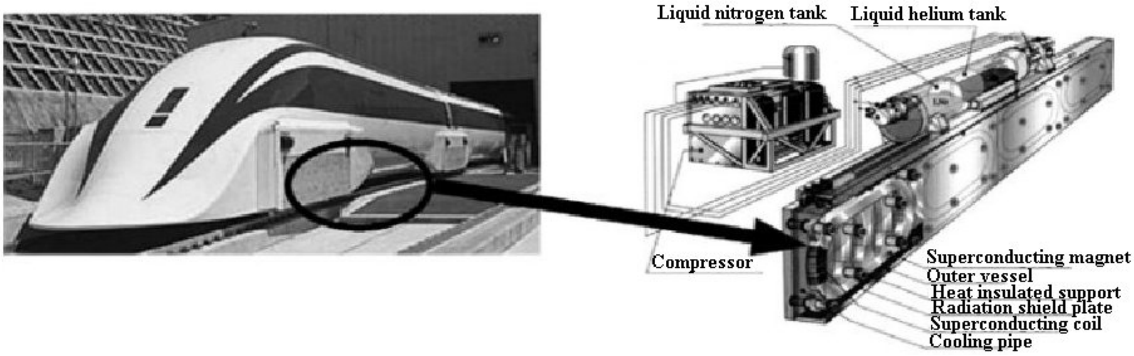

Fig. 1.6 LTS (Nb-Ti) coils installed in a superconducting magnet of Yamanashi Maglev system [21].

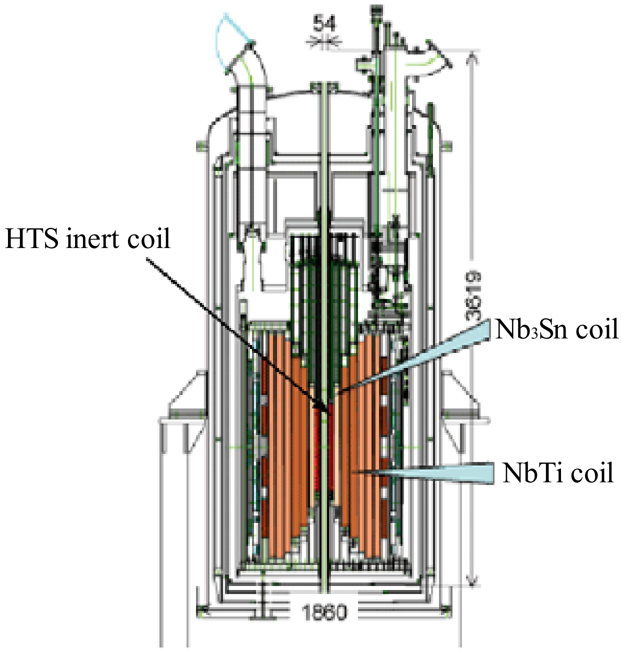

Fig. 1.7 Schematic sectional view of NMR spectrometer magnets [30].

Further, recent advances in fabrication technology of HTS wires have possibility for low cost power applications.

In the case of the Maglev train as shown in Fig. 1.6, it has been reported that the persistent current decay rate of the developed LTS magnet (inductance: 2.4 H) using Nb-Ti is less than 0.1 %/day. This magnet is cooled by liquid helium (4.2 K) [24]. On the other hand, HTS magnets using Ag-sheathed BSCCO-2223 tapes have also been developed and cooled by a cryocooler at higher temperature, e.g., 20 K. If we could replace the LTS magnet with an HTS magnet, the following advantages would be expected. Firstly, since T_c of the BSCCO wire is 110 K, the cooling cost would be reduced. Secondly, the cooling arrangement would be simplified because the structure of the system would become simple with the use of the cryocooler. However, one of the most serious problems is the persistent current decay in the magnet. The minimum rate required for one-day operation of the Maglev train is 10 %/day. It has recently been reported that the current decay of the HTS magnet for a Maglev train at operating current 532 A is less than 10 %/day (corresponding 0.42 %/hr) [25]. Therefore, in order to achieve the operation of the Maglev train continuously, the current decay needs to be compensated.

In the case of the NMR spectrometer, a very high magnetic field has to be required in order to improve the resolution. The central field of developed NMR magnets using LTS coils (Nb-Ti and Nb_3Sn) can achieve at most a field as high as 21.1 T at 1.8 K. This is a maximum limit of the central field by use of LTS wires [26]. It has been reported that the hybrid magnet using LTS coils and HTS insert coils (see Fig. 1.7) are promising to improve the resolution, because HTS coils have larger critical current density at 4.2 K even under the very high field (over 20 T) [27]. Recently, the central field at 23.5 T has been achieved [28]. Fig. 1.7 shows schematic sectional view of the combined magnets for NMR spectrometer [29]. Thus, the technology of inserted HTS magnet has been anticipated to be an excellent solution for the achievement of a very high field. However, HTS coils generate the current decay due to a small *n*-index value. The *n*-index value and persistent current decay of the superconductor are explained in subsection 1.3.2.

Consequently, a common problem for these applications using HTS coils is the compensation of the slight decay of the persistent current. Then, it has been expected that the compensation technology using a superconducting power supply is one of solutions in order to maintain such stable properties of HTS magnets [30], [31].

1.3.2 Persistent current decay in the superconducting magnet

If the current flowing in the superconducting loop is less than J_c, such current flows in the loop persistently in an ideal case. This is approximately realized for LTS magnets. In HTS magnets, however, the current decays mainly due to two reasons as follows. The

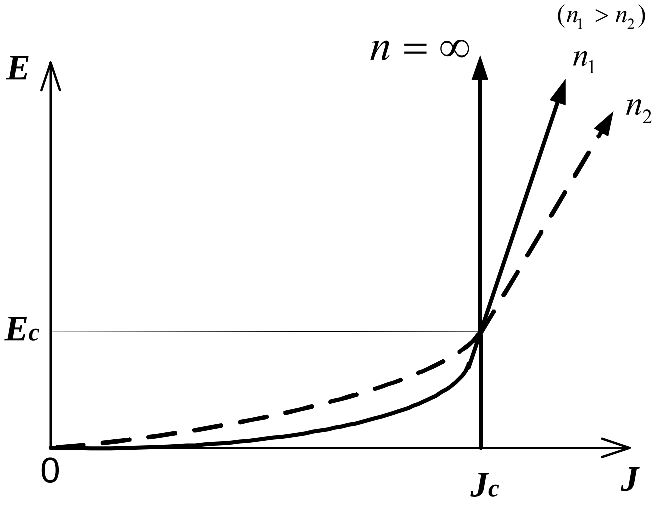

Fig. 1.8 Schematic *J-E* plots for superconductors with n=∞, n_1, and n_2 (n_1>n_2).

first reason is the joint resistance between the connections of the coils, i.e., the 'superconducting connections' are unavailable up to now.

Another reason is more intrinsic, i.e., nonlinear current transport characteristics. The index n value becomes an important specification parameter for 'persistent-mode' magnets. From the engineering point of view, the relation between electric field E versus current density J is empirically expressed as follows [32]:

$$E = E_{\mathrm{c}}\left(\frac{J}{J_{\mathrm{c}}}\right)^{n} \tag{1.1}$$

In this equation, E_{c} is the electric field criterion that defines a critical current density J_{c}. In practice, the value of E_{c} ranges from 0.1 to 1 μV/cm. The index n reflects the sharpness of the resistive transition, and such sharpness is related to the statistical distribution of critical currents and homogeneity of the superconductors; a high n-value is associated with good homogeneity.

Fig. 1.8 shows the schematic J-E plots for superconductor. If an ideal superconductor was realized, the corresponding n-value is infinite. Equation (1.1) implies that for 'real' superconductors, index n is finite value, i.e., the electric field is not zero even for current densities below J_{c} [33].

The LTS conductors have relatively high n-index values in 50-100 for Nb-Ti, and 40-80 for Nb_3Sn [34]. For HTS conductors such as YBCO and BSCCO, on the other hand, the n-index value typically ranges around 10-20 [35]. The low n-value is directly associated with the superconducting loop current decay. The HTS magnets have an intrinsically low n-value, and thus cause the persistent current decay in the closed superconducting loop [36]. From the reason, a current compensator system, i.e., the superconducting power supply is required for the HTS magnet.

1. 4 Purpose of This Study

Compared with LTS, however, since HTS has a low n value that is an intrinsic characteristic and the contact resistance, the closed superconducting magnet using HTS causes the persistent current decay [37]-[40]. Because superconducting flux pumps have been developed for a number of applications required the current generation for more than 40 years, they have currently been expected as an achievable solution for the persistent current decay in HTS magnets [41]-[45].

In this study, as a solution for the persistent current decay of superconducting magnets, we propose a new type of superconducting power supply called linear type magnetic flux pump (LTMFP). In order to accomplish the LTMFP, various investigations are carried out, i.e., theoretical approach for operating characteristic, simulation analysis using a 3-D finite element method (FEM), fabrication and assembly, and experimental performance. Further, as a practical application and a solution for current compensator, a new type of current compensator using LTMFP is accomplished. From these fundamental studies, a guideline of the new technology for the superconducting current compensator is established.

1.5 Outline of This Thesis

This thesis is composed of seven chapters and the content of each chapter is summarized as follows:

In chapter 1, the fundamental characteristics of superconductor, the necessity of the current compensator in HTS magnet systems, the current status of superconducting magnet development, and the purpose of this study are introduced.

In chapter 2, comparing with the operating mechanism of the already proposed flux pumps, the operating principle and the performance merit of the proposed LTMFP are described. Further, in order to explain the operating characteristics of the LTMFP in a wide range of the driving frequency, the already reported equations of pumping current are modified based on the phenomenon of the enhancement of the normal spot in the moving flux. From these modified equations, the operating characteristics of the LTMFP are analytically estimated under the various conditions.

In chapter 3, the magnetic flux distributions of the LTMFP by DC bias current and AC current are numerically simulated by a 3-D FEM. Further, the phenomenon of the enhancement of the normal spot in the moving flux in chapter 2 is numerically confirmed, and then increment rate is estimated.

In chapter 4, all components of current pumping system, i.e., LTMFP, two kinds of load magnets, and thermal type PCS, have been fabricated. The dimension of the LTMFP is consistent with the simulation model (chapter 3).

In chapter 5, the operating characteristics of the assembled LTMFP system are examined by experimental performances under the various conditions. In addition, calculated results of the pumping current based on the modified analytical equations in chapter 2 are compared to those of the measurement. Moreover, the operating characteristics as to frequency dependency in LTMFP are explained based on the phenomenon of enhancement of the normal spot in the moving flux (chapter 2). Its enhancing rate is estimated based on the measured values of the pumping action and the modified equation in chapter 2. The FEM simulation results for pumping tendency are confirmed with the experimental result. Further, as a basic observation for the current compensator, the pumping-up and down performances of the LTMFP are carried out under the operating load current of 10 A.

In chapter 6, as one of the solutions for the persistent current decay in the superconducting magnets, a new current compensator using LTMFP is introduced. The structure and function of the current compensator are described. As a basic investigation, the operating characteristics of the assembly system are evaluated. Further, as a practical test, the compensating action using the current compensator is demonstrated under the persistent current mode.

Finally, in chapter 7, the obtained results for every chapter and the subjects for their future study are summarized.

Chapter 2 Operating Principle and Theoretical Analysis of LTMFP

2.1 Introduction

In this chapter, the fundamental aspects of the LTMFP are explained and discussed. In general, the flux pump is inductively energized [46] and supplies current to the superconducting magnet that is operated with persistent current mode. The unique point and the operating merit of the LTMFP are explained by comparing with the already developed superconducting flux pumps. Further, in order to explain the operating principle of the LTMFP, the modified analytical equations of current pumping are introduced and discussed.

2.2 Classification of Flux Pumps

Superconducting flux pumps had been classified into two types, i.e., rotating-type and rectifier-type. As the rotating-type flux pumps are operated based on the movement of magnetic flux across the superconducting sheet, the mechanical rotating system and the superconducting sheet are important components in order to produce the required current [47]. On the other hand, rectifier-type flux pumps are operated without moving flux mechanism [48], [49]. Since the rectifier-type flux pump controls the generated current by use of a pair of superconducting persistent current switches (PCS), realization of such a switch is an important technology for the control of the required current [50]-[53]. In the following subsection, detailed principles for the respective flux pumps are explained.

2.2.1 Rotating-type flux pump

There have been some reports on the power systems using the rotating-type flux pump, i.e., the superconducting dynamo by D.V. Houwelingen and H.V. Beelen

[54]-[57], the superconducting alternator by O.K. Mawardi et al. [58], [59] and the fully superconducting generator by I. Muta et al. [60]-[64]. This type of flux pump has also been developed for charging up the current. D.V. Houwelingen, for instance, succeeded in charging up in excess of 12 KA. It has been expected that the rotating-type flux pumps are applicable to the superconducting power supply with larger current value.

The rotating-type flux pump is generally composed of a permanent magnet, a rotating system, and a superconducting niobium (Nb) foil as shown in Fig. 2.1 [65]. The superconducting Nb foil and the load magnet are connected with superconducting wires in order to form the superconducting loop. The magnetic flux applied by the rotating permanent magnet penetrates into the superconducting Nb foil, and this penetrated area is so-called ‘normal spot’ as shown in Fig. 2.1 (a). When the adequate amplitude of the moving magnetic flux, i.e., a value between lower critical field $\mu_0 H_{c1}$ and upper critical field $\mu_0 H_{c2}$ of the Nb foil penetrates into the Nb foil, the region of the normal spot in the Nb foil keeps the mixed state. In this case, the phase of the normal spot is in the dissipative state (flux flow state). It should be noted, on the other hand, that the area except for the normal spot is still in a superconducting state.

The superconducting closed loop is always realized even in the case of formation of the normal spots. By moving the normal spot from outside of the superconducting Nb foil into the superconducting loop, the shielding current surrounding the normal spot is pumped into the loop [66]. This is the basic concept of current pumping.

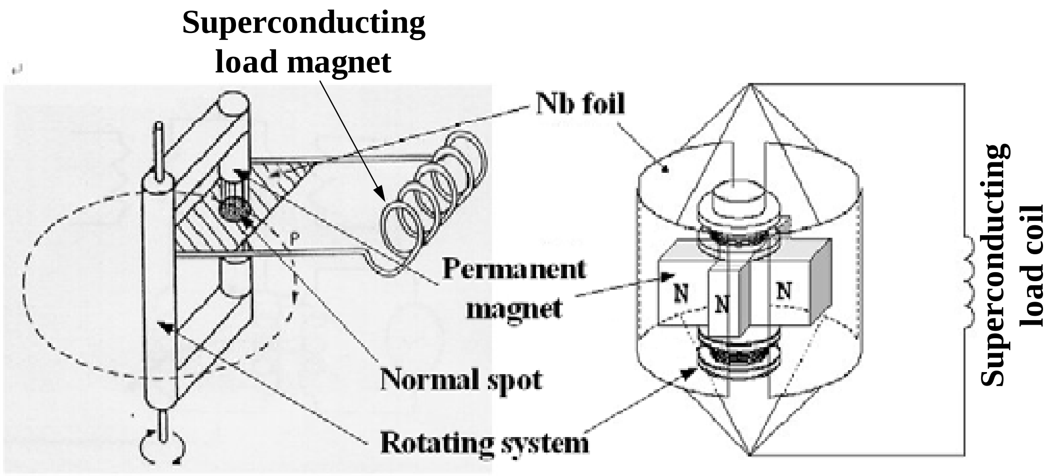

(a) schematic diagram

(b) illustration for developed rotating type flux pump with permanent magnets

Fig. 2.1 Principle of rotating-type superconducting flux pump [65].

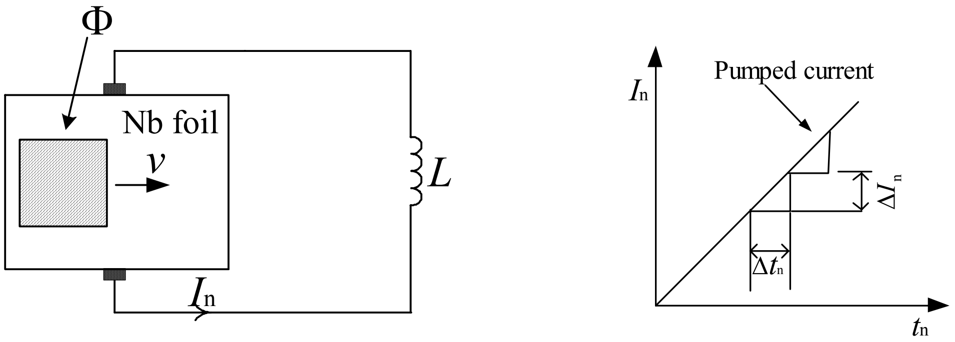

(a) pumping action (b) plot of pumped current I_n as a function of time

Fig. 2.2 Pumping mechanism of rotating-type flux pump and plot of pumped current [67].

Fig. 2.2 shows the schematic diagram of the pumping action [67]. The symbols of I_n, Φ, L, v, and t denote, respectively, the pumped current, the applied magnetic flux, the self-inductance of load magnet, the moving velocity of normal spot, and operating time. When the normal spot due to Φ is pumped into the superconducting Nb foil, the pumped current I_n flows in the load magnet as shown in Fig. 2.2 (a). By repeating above-mentioned action, the current is linearly pumped up as shown in Fig. 2.2 (b). The values of ΔI_n and Δt_n represent, respectively, the increasing rate of the pumped current and the corresponding operation time for one pumping action.

2.2.2 Rectifier-type flux pump

Various kinds of the rectifier-type flux pump have been proposed as follows; transformer-type by Y. Iwasa et al. [68], [69], heater trigger-type by T.K. Ko et al. [70]-[72], and cryotron switch-type by S.K. Jeong [73].

As the rectifier-type flux pump controls the current pumping by means of a pair of fast-response PCSs, various technologies for PCSs that have been fabricated by the use of superconducting wire have been developed. As an example, the circuit diagram of the transformer-type superconducting flux pump is introduced as shown in Fig. 2.3 [68]. In the figure, the symbols of I_n, I_{DC1}, and I_{op}, correspondingly, represent the pumped current, the external DC current, and the operating load current.

The load magnet is fabricated using the superconducting wire (Nb-Ti). In addition, S_{p1} is a slow-response PCS, while S_{p2} and S_{p3} are fast-response PCSs. In order to supply the current to the load magnet, I_{DC1} is shunted with open S_{p1}. Then, the persistent current mode is realized by the turning on S_{p1} (switch off). The current pumping is controlled by a pair of PCSs (S_{p2} and S_{p3}). The detailed sequences are explained as follows [74], [75]:

(Step 1): the load magnet is initially energized by the current source I_{DC1} (S_{p1} and S_{p2}: open, and S_{p3}: closed), and then the operating current I_{op} flows through Loop 1. Of course, I_{op} is equal to I_{DC1} in this case.

(Step 2): Loop 1 forms persistent current loop (S_{p1} and S_{p3}: closed, S_{p2}: open).

(Step 3): the persistent current loop (Loop 2) is formed by S_{p2} closed and S_{p3} open. In this case, I_n sums up I_{op}.

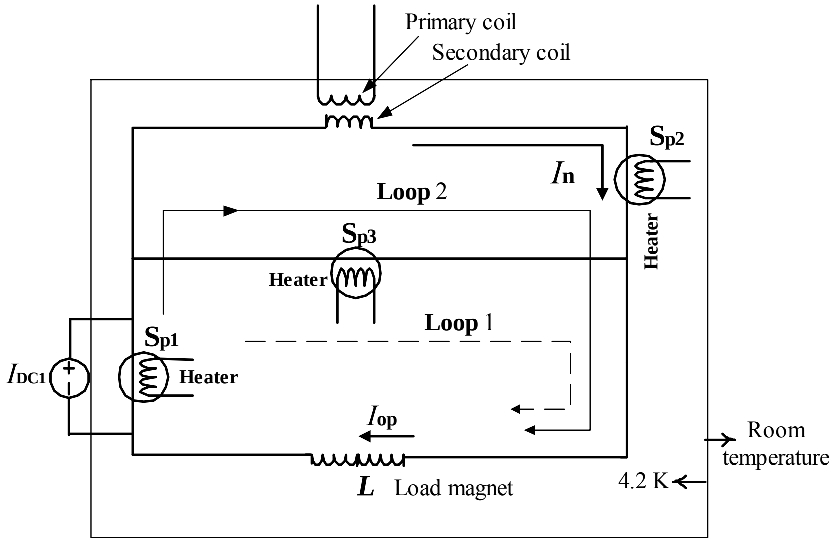

Fig. 2.3 Circuit diagram of transformer-type superconducting flux pump [68].

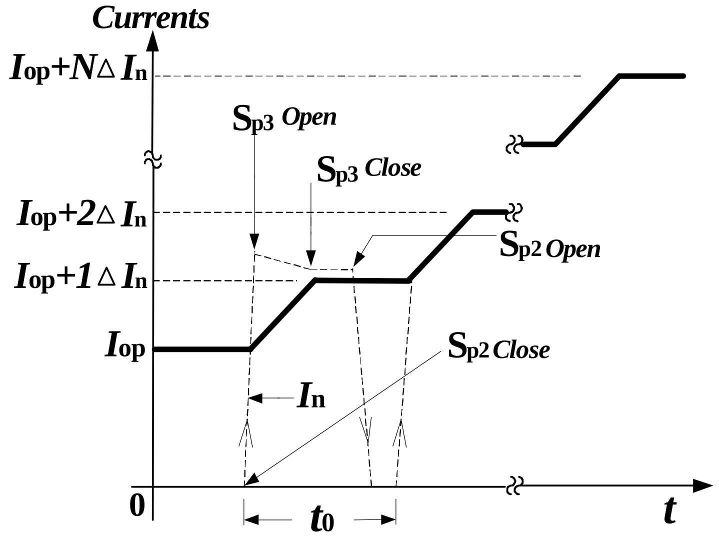

Fig. 2.4 Schematic plot of current pumping by PCS operations [68].

(Step 4): Loop 1 is formed (S_{p2}: open, S_{p1} and S_{p3}: closed). Loop 1 keeps I_n added to I_{op}.

(Step 5): the cycles of step 3 and step 4 are repeated for the current compensation.

Fig. 2.4 shows the schematic drawing of the pumping up sequence. The symbols of ΔI_n and t_0 represent the enhancement rate of pumped current and the period for one operation, respectively. In the flux pump, the superconducting closed loops (Loop 1 and Loop 2) are easily switched by the operations of S_{p2} and S_{p3}.

I_{op} at load magnet is periodically pumped by the operations of S_{p2} and S_{p3}; I_n starts pumping by S_{p2} closed and reaches maximum by S_{p3} open. In order to switch off the PCS, however, the heater attached to superconducting wire has to be energized. And then, the corresponding heat loss becomes a problem in liquid helium (4.2 K) [76].

2.2.3 Proposal for the linear-type magnetic flux pump

As a new type of the superconducting flux pump, we have proposed the linear-type magnetic flux pump (LTMFP), which utilizes traveling magnetic fields [77]. Fig. 2.5 illustrates the schematic diagram of the primary side, in which the traveling field is generated by means of the 3-phase armature current. The structure of the armature windings looks like that of linear induction motor; this magnetic flux pump is called 'linear-type' [78], [79].

The schematic diagram of the proposed LTMFP current pumping system is shown in Fig. 2.6. In this figure, the LTMFP consists of a couple of DC bias coils, 3-phase armature windings, a laminated iron core, and a piece of superconducting Nb foil. The current pumping system is formed by the above-mentioned LTMFP, a PCS (S_{p1}), an external DC current source (I_{DC1}), and a superconducting load magnet. The Nb foil, S_{p1}, and the load magnet are connected using superconducting wires, and these attain a closed superconducting current loop.

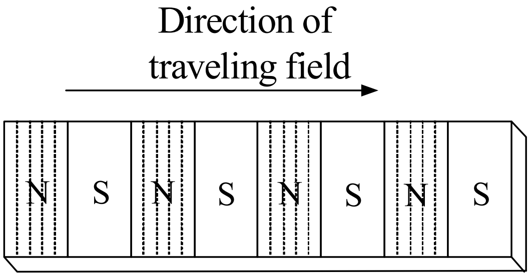

Fig. 2.5 Schematic diagram of primary side in LTMFP.

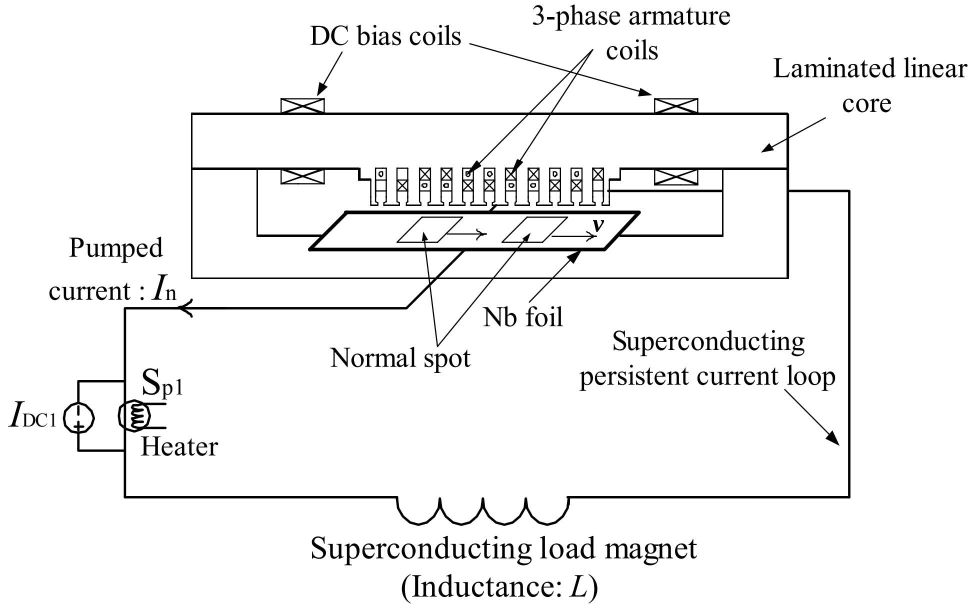

Fig. 2.6 Schematic diagram of LTMFP current pumping system.

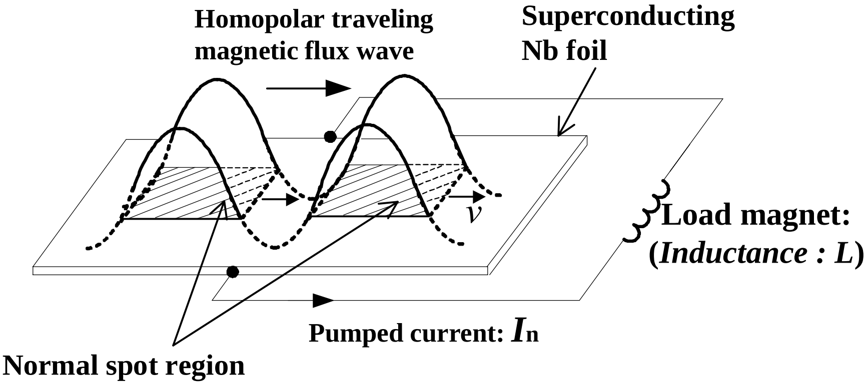

Fig. 2.7 Schematic illustration of normal spot area produced by the homo-polar traveling magnetic flux wave on the Nb foil.

The traveling magnetic field is realized by means of three phase armature windings. The amplitude of the field is also moved up to the positive value with the use of the DC bias coils; the homo-polar traveling magnetic field is produced and applied to the superconducting Nb foil, which is located in the air gap of the LTMFP. Fig. 2.7 shows the schematic illustration of the homo-polar traveling magnetic field (its velocity: v) applied to the Nb foil that is connected to the superconducting load magnet. The magnetic field penetrates into the Nb foil in the region, at which the amplitude of the field is between lower critical magnetic field ($\mu_0 H_{c1}$) and upper critical magnetic field

($\mu_0 H_{c2}$) of the Nb foil. The current pumping mechanism of the LTMFP is similar to that of the rotating type. However, the proposed LTMFP has the following merits:

[1] Compared with the rotating-type flux pump, the proposed LTMFP produces the traveling magnetic field without a mechanically rotating system, i.e., static system. From this merit, the LTMFP can reduce mechanical vibration and electric noise [80].

[2] The speed of the traveling magnetic field, i.e., current pumping rate, is easily and swiftly controllable by means of the inverter.

[3] Compared with the rectifier-type flux pump, the control sequence in the proposed LTMFP becomes simpler [81].

2.3 Theoretical Analysis of LTMFP

The already reported analytical equation for flux pumps [82] partially explained the operating characteristics of the rotating-type flux pump. The suggested equation, however, assumed that the normal spot size does not change during the operation of the flux pump [83]. The reported equation could only explain the operating characteristics of rotating-type flux pumps in lower speed movement of normal spot (below 20 Hz) [84]. In order to examine faster speed operation, a new analytical equation that takes into account the detailed behavior of the normal spot is necessary.

In this section, the already reported analytical equation is modified in order to express the higher frequency operation of the flux pump; the key point of the modification is that the size of the normal spot is assumed to be changeable depending on the driving frequency.

2.3.1 Pumping sequence

As already mentioned, the operational mechanism of the proposed LTMFP is similar to that of the rotating-type. In this subsection, the current pumping sequence is explained in more detail based on the position of the normal spots. Fig. 2.8 shows the schematic diagram of (a) invasion of the normal spot in the Nb foil and (b) the corresponding equivalent circuit. In the figure, the superconducting Nb foil is connected with the superconducting load magnet, allowing the realization of the superconducting circuit. Further, the parameters l and L denote the self-inductance of superconducting Nb foil and the load magnet, respectively.

The pumped current I_n is induced by moving magnetic flux Φ in the superconducting Nb foil. The increment rate of the induced pumping current can be expressed as [85],

$$\Delta I_n = \frac{\Phi}{L} \tag{2.1}$$

As is shown in Fig. 2.8 (b), the normal spot apparently plays an on-off switching element according to its position. In this figure, the loops ABEF and BCDE, respectively, include an Nb foil and the load magnet.

Fig. 2.9 illustrates the schematic diagram of the current pumping operation. If the switches S_1 and S_2 are turned on in the state (that means the normal spot is not yet invaded in the Nb foil), the I_0 flows in the loop ACDF. Also, the current of the loop ABEF and that of BCDE should be equal as shown in Fig. 2.9 (a). In addition, in the

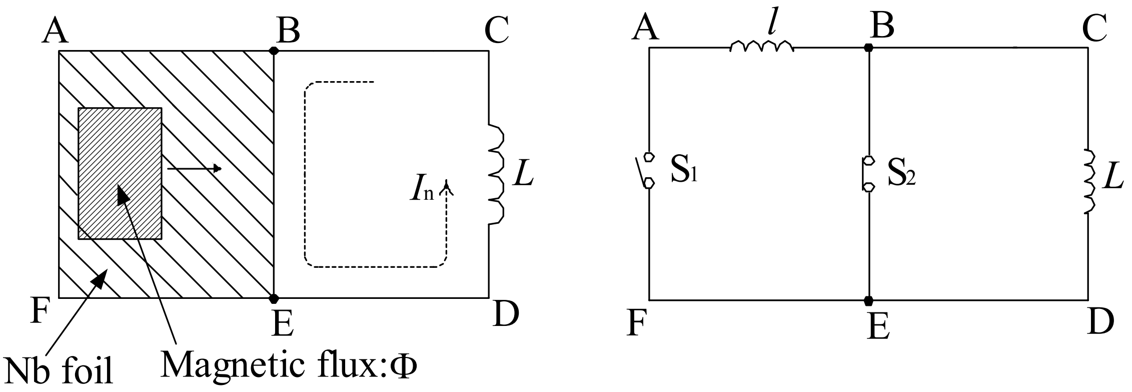

(a) connection diagram (b) equivalent circuit

Fig. 2.8 Schematic diagram of the invasion of the normal spot and corresponding equivalent circuit [84].

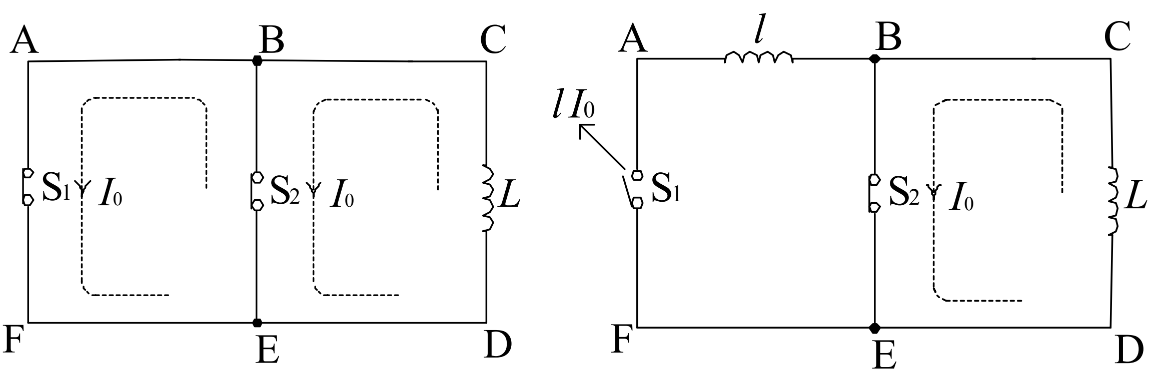

(a) the normal spot is outside of the Nb foil (b) the normal spot is inside of the Nb foil

Fig. 2.9 Schematic diagram of the current pumping operation [86].

case of S_1 opening, the value of magnetic flux $\Phi_0 = l \cdot I_0$ is released per one cycle as shown in Fig. 2.9 (b). Consequently, the resultant value of the pumped current, $\triangle I_n$, through the persistent current loop is expressed as [86],

$$\Delta I_{\mathrm{n}} = \frac{\Phi - l \cdot I_0}{L} \tag{2.2}$$

Fig. 2.10 illustrates the basic pumping sequences according to the positions of the normal spot. Table 2.1 also shows the variations of the magnetic flux $\Delta\Phi$ and the load current I_L with the switching conditions for each step. The descriptions of these steps are as follows:

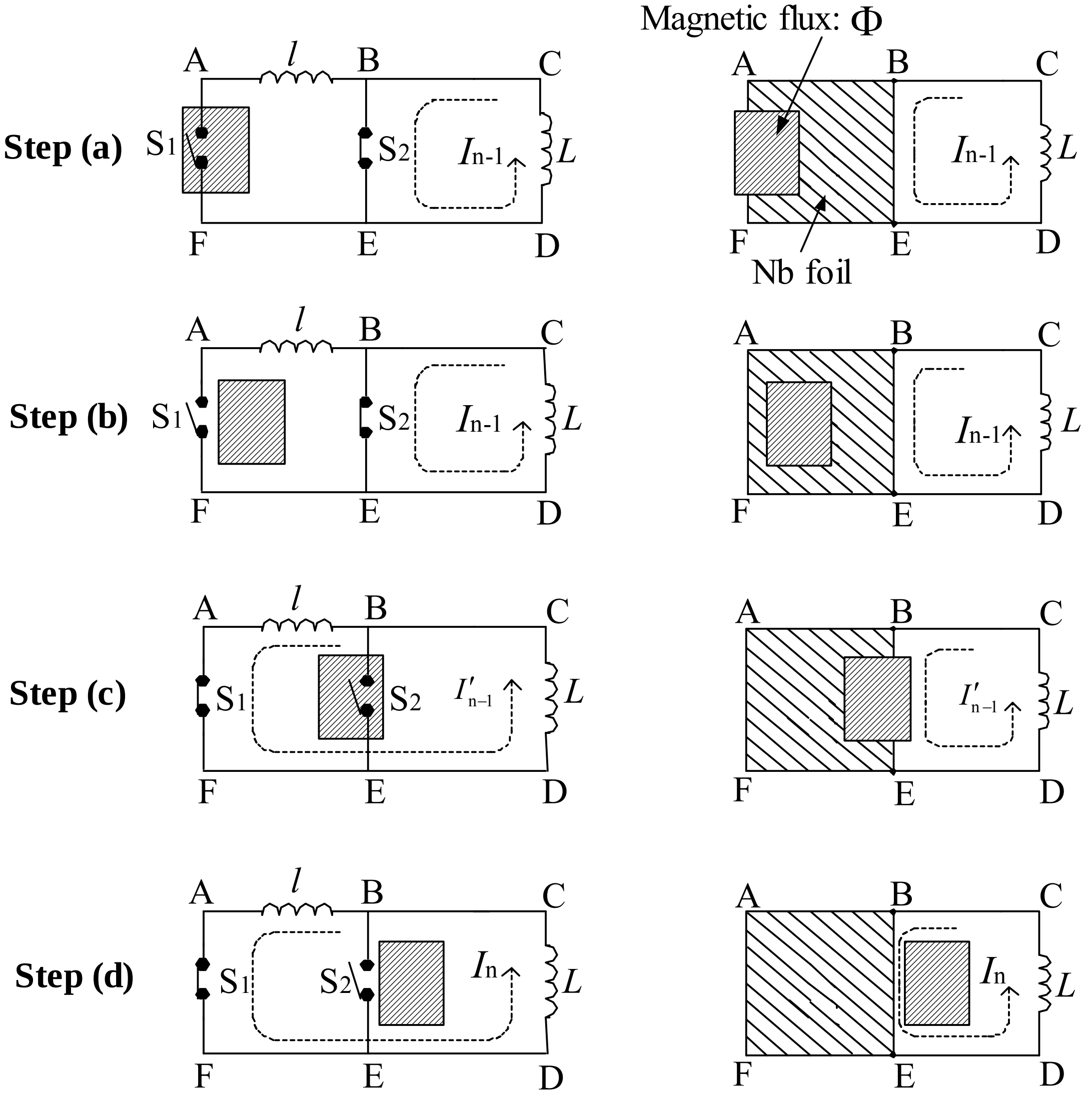

Fig. 2.10 Basic pumping sequences of the LTMFP according to the position of normal spot.

Table 2.1 Variations of the magnetic flux $\Delta\Phi$ and the load current I_L with the switching condition for each step in LTMFP.

Step	S_1	S_2	$\Delta \Phi$	I_L
(a)	off	on	$\Phi - l \cdot I_{n-1}$	I_{n-1}
(b)	off	on	$\Phi - l \cdot I_{n-1}$	I_{n-1}
(c)	on	off	$\Phi - l \cdot I_{n-1}$	I'_{n-1}
(d)	on	off	$\Phi - l \cdot I_{n-1}$	I_n

Step (a): the current I_{n-1} initially flows through the loop BCDE. The magnetic flux Φ begins to enter the Nb foil at this step (S_1:open). The changed value of magnetic flux is $\Phi - l \cdot I_{n-1}$.

Step (b): Φ is now in the Nb foil. The I_{n-1} flows through the loop BCDE. The S_1 is still open due to the time delay for recovery from normal to superconducting transition.

Step (c): Φ begins to leave the Nb foil. The S_1 is now in on state. The induced current I'_{n-1} flows through the loop ACDF since S_2 is opened. Here, the current I'_{n-1} is obtained as follows:

$$I'_{n-1} = \frac{L}{L+l} I_{n-1} \tag{2.3}$$

Step (d): Φ leaves the Nb foil. The induced I_n flows through the loop ACDF since S_2 is still open due to the time delay for recovery from normal to superconducting transition.

The changed amount of magnetic flux, $\Delta\Phi$, is expressed as,

$$\Delta\Phi = \Phi - l \cdot I_{n-1} \tag{2.4}$$

The pumped current at the nth cycle, I_n, can then be given by

$$I_n = I'_{n-1} + \frac{\Delta\Phi}{L+l} \tag{2.5}$$

By using equations (2.3) and (2.4), the equation (2.5) becomes

$$\begin{aligned} I_n &= I'_{n-1} + \frac{\Phi - l \cdot I_{n-1}}{L+l} \\ &= \frac{L}{L+l} I_{n-1} + \frac{\Phi - l \cdot I_{n-1}}{L+l} \end{aligned}$$

$$= I_{\mathrm{n}-1} + \frac{\Phi - 2l \cdot I_{\mathrm{n}-1}}{L + l} \tag{2.6}$$

For example, the temporal development of the pumped current, $I_0 \rightarrow I_1 \rightarrow I_2 \rightarrow I_3$, with the condition at $I_0 = 0$ can be expressed as follows

$$I_1 = I_0 + \frac{\Phi - 2l \cdot I_0}{L + l}$$

$$= \frac{\Phi}{L + l}$$

$$I_2 = I_1 + \frac{\Phi - 2l \cdot I_1}{L + l}$$

$$= \frac{\Phi}{L + l}\left(1 + \frac{L - l}{L + l}\right)$$

$$I_3 = I_2 + \frac{\Phi - 2l \cdot I_2}{L + l}$$

$$= \frac{\Phi}{L + l}\left\{1 + \frac{L - l}{L + l} + \left(\frac{L - l}{L + l}\right)^2\right\} \quad \cdots$$

Generalizing this result, we have

$$I_{\mathrm{n}} = \frac{\Phi}{L + l}\left\{\sum_{k=1}^{n}\left(\frac{L - l}{L + l}\right)^{k-1}\right\} \tag{2.7}$$

Finally, we obtain

$$I_{\mathrm{n}} = \frac{\Phi}{2l}\left\{1 - \left(\frac{L - l}{L + l}\right)^{\mathrm{n}}\right\} \tag{2.8}$$

The pumped current is generated by repeating the above-mentioned pumping sequence. In addition, the relation between the pumped current and the operating period is shown in Fig. 2.11. The increment of the current, ΔI, is realized for one cycle (its period is T). The digitized operation time t_{n} is expressed as nT. For two arbitrary points $(t_{\mathrm{n}}, I_{\mathrm{n}})$ and $(t_{\mathrm{n}+1}, I_{\mathrm{n}+1})$, the increased value can be expressed as,

$$\frac{\Delta I}{\Delta t} = \frac{I_{\mathrm{n}+1} - I_{\mathrm{n}}}{t_{\mathrm{n}+1} - t_{\mathrm{n}}} = \frac{\Delta I}{T} \tag{2.9}$$

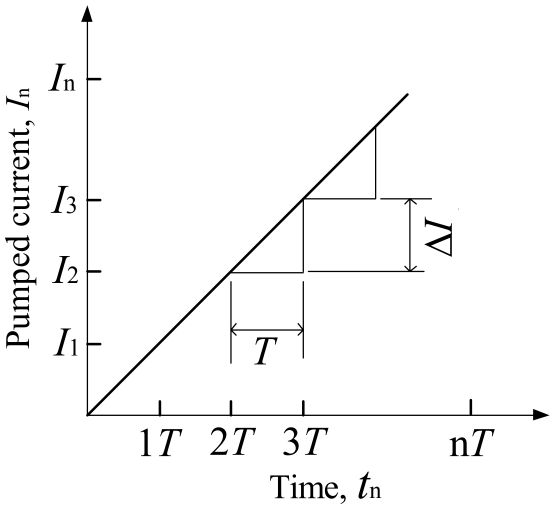

Fig. 2.11 Plot diagram between pumped current I_n and operating period t_n.

From the equations (2.6) and (2.9), the value of *dI*/*dt* is written as,

$$\frac{dI(t)}{dt} = \frac{\Phi - 2l \cdot I(t)}{L + l}\frac{1}{T} \tag{2.10}$$

Solving equation (2.10), we have

$$I(t) = \frac{\Phi}{2l}\left\{1 - \exp\left(-\frac{2l}{T(L+l)}t_{\mathrm{n}}\right)\right\} \tag{2.11}$$

Since the operating time t_n is nT, from the equation (2.11) we obtain

$$\exp\left(-\frac{2l}{T(L+l)}t_{\mathrm{n}}\right) = \exp\left(-\frac{2l}{(L+l)}\mathrm{n}\right) = \left(\exp\left(-\frac{2l}{L+l}\right)\right)^{\mathrm{n}}$$

$$= \left\{1 - \frac{1}{1}\left(\frac{2l}{L+l}\right) + \frac{1}{2}\left(\frac{2l}{L+l}\right)^2 - \frac{1}{3}\left(\frac{2l}{L+l}\right)^3 + \cdots\right\}^{\mathrm{n}} \tag{2.12}$$

Because L is always larger than l ($L \gg l$), the sum below the third term of equation (2.12) can be ignored. The equation (2.12) can then be rewritten as

$$\left\{1 - \frac{1}{1}\left(\frac{2l}{L+l}\right) + \frac{1}{2}\left(\frac{2l}{L+l}\right)^2 - \frac{1}{3}\left(\frac{2l}{L+l}\right)^3 + \cdots\right\}^{\mathrm{n}} = \left(\frac{L-l}{L+l}\right)^{\mathrm{n}} \tag{2.13}$$

We can express the equation (2.12) as

$$\exp\left(-\frac{2l}{T(L+l)}t_{\mathrm{n}}\right) = \left(\frac{L-l}{L+l}\right)^{\mathrm{n}} \tag{2.14}$$

Using equation (2.14), the equation (2.11) can be rewritten as

$$I(t) = \frac{\Phi}{2l}\left\{1 - \left(\frac{L-l}{L+l}\right)^{\mathrm{n}}\right\} \tag{2.15}$$

2.3.2 Basic equations of pumped current in LTMFP

In this subsection, the expressions of the current pumping in the LTMFP are introduced based on the already reported discussions.

Fig. 2.12 shows the schematic diagram of moving the normal spot in the Nb foil of the LTMFP. The symbols of z, d, v, W, R_{n}, w, and h represent the thickness of Nb foil, the gap between slot and Nb foil, the moving velocity of normal spot, the total width of the Nb foil, the resistance of normal spot, the width of normal spot, and the length of normal spot, respectively.

In the Nb foil, induced electromotive force $\nabla \boldsymbol{E}$ is expressed as,

$$\nabla \boldsymbol{E} = ((-v)\times B)\cdot h \tag{2.16}$$

B is the magnetic flux density that is applied perpendicular to the surface of the Nb foil. Thus, the induced current I_{R} for one normal spot is

$$I_{\mathrm{R}} = -\frac{B\cdot v\cdot h}{R_{\mathrm{n}}}\cdot\frac{w}{\mathrm{W}} \tag{2.17}$$

By using the relations of magnetic flux $\Phi = B\cdot h\cdot w$ and the period of one pumping action T=W/v, the equation (2.17) can be written as

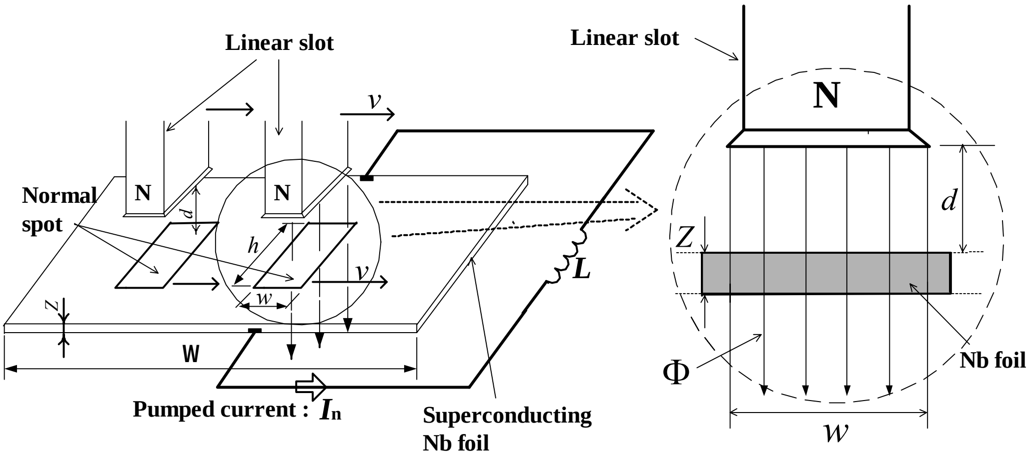

Fig. 2.12 Schematic diagram of traveling normal spot on the superconducting Nb foil in the LTMFP.

$$I_{\mathrm{R}} = \frac{\Phi}{R_{\mathrm{n}}\, T} \tag{2.18}$$

By using the current at the (n-1)th cycle, $I_{\mathrm{n-1}}$, the changing rate of the magnetic flux $\Delta\Phi$ is expressed as,

$$\Delta\Phi = \left(\Phi - \frac{\Phi}{R_{\mathrm{n}}\, T} l - l \cdot I_{\mathrm{n-1}} \right) \tag{2.19}$$

As the LTMFP always produces two normal spots at the Nb foil, due to the 4-pole configuration in our system, the corresponding total changed amount of the magnetic flux $\Delta\Phi_{\mathrm{LTMFP}}$ can be expressed as,

$$\Delta\Phi_{\mathrm{LTMFP}} = \left(2\Phi - \frac{2\Phi \cdot 2l}{2R_{\mathrm{n}}\, T} - 2l \cdot I_{\mathrm{n-1}} \right) \tag{2.20}$$

Referring to the equation (2.5), at the nth cycle, the pumped current I_{n} becomes

$$I_{\mathrm{n}} = \frac{\Delta\Phi_{\mathrm{LTMFP}}}{L+2l} + I'_{\mathrm{n\text{-}1}} \tag{2.21}$$

Also, referring to the equation (2.3), $I'_{\mathrm{n-1}}$ can be written as

$$I'_{\mathrm{n-1}} = \frac{L}{L+2l} I_{\mathrm{n-1}} \tag{2.22}$$

Therefore, using equations (2.20) and (2.22), the equation (2.21) becomes

$$I_{\mathrm{n}} = \frac{1}{L+2l} \left\{ 2\Phi - \frac{2\Phi l}{R_{\mathrm{n}}\, T} - 2l \cdot I_{\mathrm{n-1}} \right\} + \frac{L}{L+2l} I_{\mathrm{n-1}}$$

or

$$I_{\mathrm{n}} = 2\Phi \left(1 - \frac{l}{R_{\mathrm{n}}\, T} \right) \frac{1}{L+2l} + \frac{L-2l}{L+2l} I_{\mathrm{n-1}} \tag{2.23}$$

From the equation (2.23), a general form can be rewritten with the condition at I_0=0 as,

$$I_1 = 2\Phi \left(1 - \frac{l}{R_{\mathrm{n}}\, T} \right) \frac{1}{L+2l}$$

$$I_2 = I_1 + \frac{L-2l}{L+2l} I_1$$

$$I_3 = I_1 + \frac{L-2l}{L+2l} I_1 + \left(\frac{L-2l}{L+2l} \right)^2 I_1 \;\; , \ldots$$

Generalizing these results, we have

$$I_{\mathrm{n}} = \frac{\Phi}{2l}\left(1 - \frac{l}{R_{\mathrm{n}}\,T}\right)\left\{1 - \left(\frac{L-2l}{L+2l}\right)^{\mathrm{n}}\right\} \tag{2.24}$$

Referring to equations (2.12) and (2.13), the equation (2.24) can be rewritten as,

$$I(t) = \frac{\Phi}{2l}\left(1 - \frac{l}{R_{\mathrm{n}}\,T}\right)\left[1 - \exp\left\{-\frac{4l}{T(L+2l)}t_{\mathrm{n}}\right\}\right] \tag{2.25}$$

Since the *f* is defined as $1/T$, the pumped current $I\,(t)$ is expressed as,

$$I(t) = \frac{\Phi}{2l}\left(1 - \frac{f\,l}{R_{\mathrm{n}}}\right)\left[1 - \exp\left\{-\frac{4f\,l}{L+2l}t_{\mathrm{n}}\right\}\right] \tag{2.26}$$

The expressions of l, R_{n}, and Φ are defined as follows; $l = \mu_0 \cdot S_{\mathrm{n}} / d$, ($S_{\mathrm{n}} = w \cdot h$: area of the normal spot, μ_0 (=$4\pi\times10^{-7}$ H/m): magnetic permeability of the vacuum) [87], $R_{\mathrm{n}} = \rho \cdot h / z \cdot w$ (ρ (=1×10^{-8} Ωm): resistivity of the normal spot) [88], and $\Phi = B \cdot S_{\mathrm{n}} = B \cdot w \cdot h$. The above-mentioned equation is introduced based on the simple assumption that the size of the normal spot is always constant during operation.

2.3.3 Phenomenon of the enhancement of the normal spot

In order to discuss about the experimental results of the already developed flux pumps, the size of the 'normal spot' has been regarded as the constant value [89]. In our preliminary study, however, we can not explain the results by using such assumption when the driving frequency becomes higher. Then, we propose the modified theory with that the 'normal spot' size is changeable depending on the frequency. This is based on the phenomenon of magnetic diffusion in superconductor [90]. In this subsection, the above-mentioned theory is explained. The validity of our assumption will be shown later by comparing with the simulation as well as experimental results.

As is already mentioned in subsection 1.2.3 and 1.2.4, quantized magnetic fluxes experience the Lorentz force when the transport current flows in the superconductor.

When the time varying magnetic field is applied to the superconductor, the penetrated magnetic fluxes are diffused with following relation.

$$D_{\mathrm{m}}\nabla^2 B = \partial B / \partial t \tag{2.27}$$

where D_m ($=\rho/\mu_0$; ρ : resistivity of superconductor and μ_0 : magnetic permeability of the vacuum) is the magnetic diffusivity.

In the case of the slab, the equation of characteristic time of magnetic diffusion in superconductor t_md, is expressed as [91]

$$t_\mathrm{md} = \frac{(2\mathrm{a})^2}{\pi^2 D_\mathrm{m}} \tag{2.28}$$

where 2a represents the width of the superconductor. The corresponding frequency of magnetic diffusion can be estimated as f_t ($f_\mathrm{t} = \frac{1}{t_\mathrm{md}}$). That is, if the driving frequency of the traveling magnetic field f exceeds f_t in the superconductor, the changing speed of the normal spot cannot follow that of the moving field. This means that the flux penetrated region (normal spot area) is enhanced. This is the phenomenon of the enhancement of the normal spot in the penetrated moving flux.

Fig. 2.13 illustrates the schematic diagrams of the enhanced normal spot on the superconductor by the moving magnetic field. When the transport current I flows in a superconductor with a traveling magnetic fields ($B > \mu_0 H_\mathrm{c1}$), a Lorentz force F_L acts to move the fluxoids. If the speed of the varying magnetic field is low ($v = v_1$) as shown in Fig. 2.13 (a), the bundles of fluxoids are also moved due to the F_L. This means that the corresponding driving frequency f is lower than f_t. On the other hand, Fig. 2.13 (b) shows the normal spot area in the superconductor at high speed $v = v_2$, i.e., $v_2 > v_1$. In this

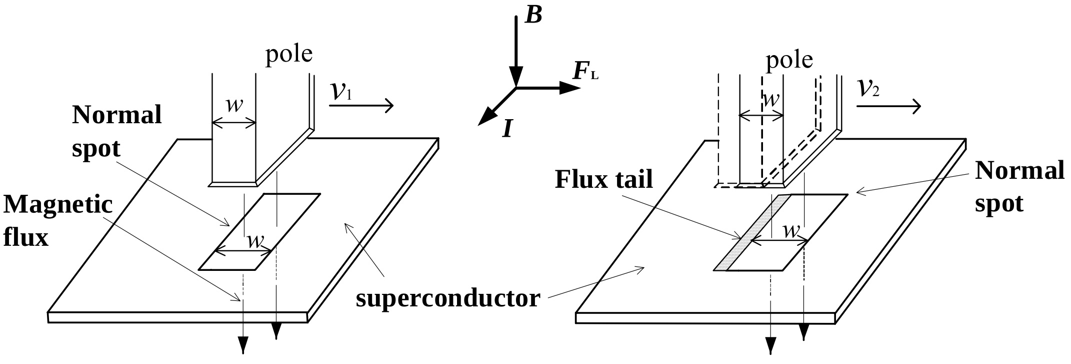

(a) $v = v_1$ (low speed)　　(b) $v = v_2$ (high speed)

Fig. 2.13 Illustration for the area of normal spot on the superconductor according to velocity of the moving magnetic field.

case, the corresponding f is higher than f_t. Under this condition, since the moving velocity of the traveling magnetic field exceeds the diffusion velocity of the fluxoids, the normal spot size will be enlarged. Here, the superconducting-to-normal transition surface is called the 'flux front' and normal-to-superconducting transition surface is called the 'flux tail' in Fig. 2.13 (b).

This phenomenon can apply to the performance of the LTMFP. Fig. 2.14 shows the simplified diagrams of the enhancement of the normal spot in the LTMFP according to the moving velocity of magnetic flux. When the moving speed of the magnetic flux is low v_1 (the corresponding frequency of traveling magnetic field f is below f_t), the enhancement rate of the normal spot is small as shown in Fig. 2.14 (a) (the variation of g_1 is small enough). On the other hand, when the moving velocity of magnetic fluxes progresses at high speed v_2 (the corresponding frequency of traveling magnetic field f exceeds f_t), the distance between two normal spots g_2 is continuously decreased, due to the enhancement of normal spots as shown in Fig. 2.14 (b).

Thus, when the width of the normal spot is enhanced according to the driving frequency, referring to the equation (2.26), the resistance of the normal spot R_n is influenced by the enhanced width w_n. Then, the following expressions are assumed as a function of the frequency f.

$$w_n(f) = w_0 + kf = \alpha,\ R_n(f) \propto 1/\alpha, \text{ and } l_n(f) = l_{sh} + l_0 \cong l_{sh} = \text{constant} \qquad (2.29)$$

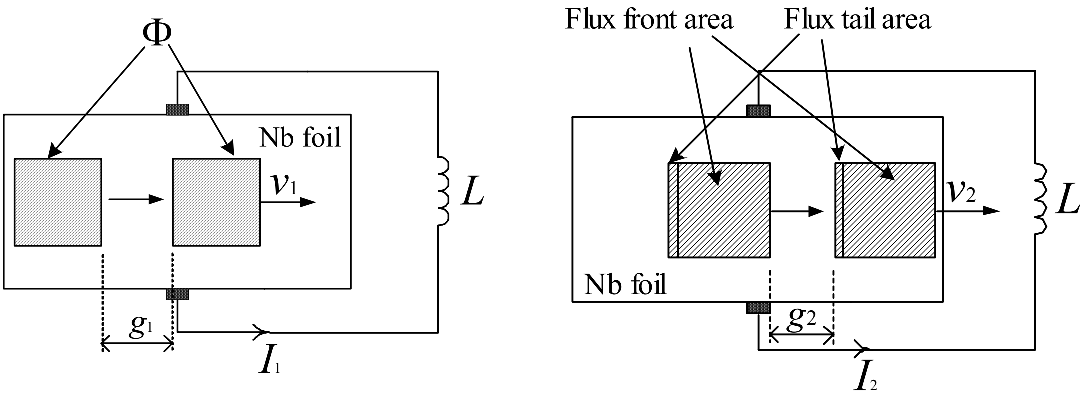

(a) $v = v_1$ (low speed) (b) $v = v_2$ (high speed)

Fig. 2.14 Pumping mechanism by the phenomenon of enhancing the normal spot in the LTMFP during the movement of two poles.

Where, w_{n} and l_{n} are the total enhanced width of the normal spot and total inductance of normal spot during the operating time, respectively. These symbols of w_0, l_{sh}, and l_0 denote the initial width of normal spot, inductance of the Nb foil by shielding current, and initial inductance of Nb foil, respectively. The initial condition means that there exists no enhancement of the normal spot. Further, the parameter k represents the enhancement rate of the moving normal spot. In the case of the inductance of normal spot, l_0 is increased by the enhanced normal spot. However, since l_{sh} is larger than l_0, total inductance l_{n} is same with l_{sh}. That means l_{n} keeps constant even under the phenomenon of magnetic diffusion.

Consequently, from equations (2.26) and (2.29), the modified analytical equation of the pumping current for the LTMFP can be derived as,

$$I(t) = \frac{\Phi}{2l_{\mathrm{n}}}\left(1-\frac{f\,l_{\mathrm{n}}}{R_{\mathrm{n}}}\right)\left[1-\exp\left\{-\frac{4f\,l_{\mathrm{n}}}{L+2l_{\mathrm{n}}}t_{\mathrm{n}}\right\}\right] \tag{2.30}$$

In addition, based on the equation (2.30), the equation for pumped current rate at $t = 0$ becomes

$$\left.\frac{dI}{dt}\right|_{t_{\mathrm{n}}=0} = \frac{2f\,\Phi}{L+2l_{\mathrm{n}}}\left(1-\frac{f\,l_{\mathrm{n}}}{R_{\mathrm{n}}}\right) \tag{2.31}$$

These expressions of the enhancement of the normal spot are confirmed by means of the FEM simulation for the magnetic behavior of Nb foil in chapter 3.

2.3.4 Operating characteristics of the LTMFP based on the analytical equation

In this subsection, the operating characteristics of the LTMFP are analytically discussed. These analytical characteristics are based on the modified equation of the pumping current (equation (2.30)).

Fig. 2.15 displays the schematic drawing of the current pumping according to the inductance of load magnet L. For the cases of $L_1 > l$ and $L_2 \gg l$ (l means self inductance of Nb foil), the analytical curves of the pumped current are illustrated, respectively. The increasing rate of pumping current can be characterized as $\tau_{\mathrm{p}}\left(=\frac{L+2l_{\mathrm{n}}}{4f\,l_{\mathrm{n}}}\right)$.

The total flux Φ is defined as inductance L and flowing current I as follows

$$\Phi = L \cdot I, \qquad I = \frac{\Phi}{L} = \frac{B \cdot S}{L} \tag{2.32}$$

where B and S denote the magnetic flux density and the area of applied magnetic field.

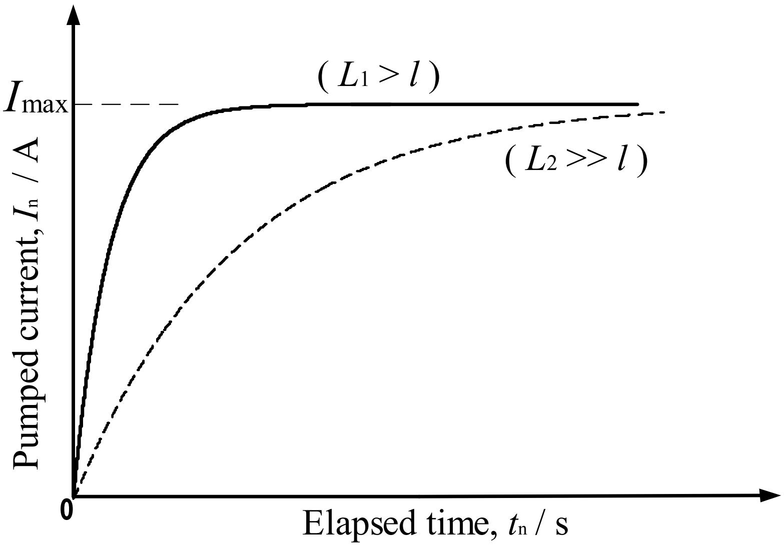

Fig. 2.15 Schematic drawing of the relation between the current pumping and the inductance value of load magnet L.

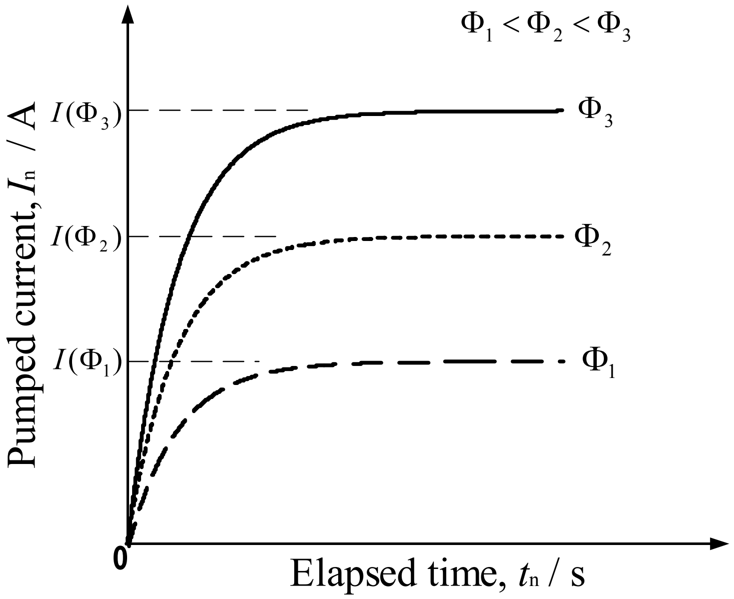

Fig. 2.16 Schematic drawing of the relation between the maximum value of current pumping and the applied magnetic flux Φ.

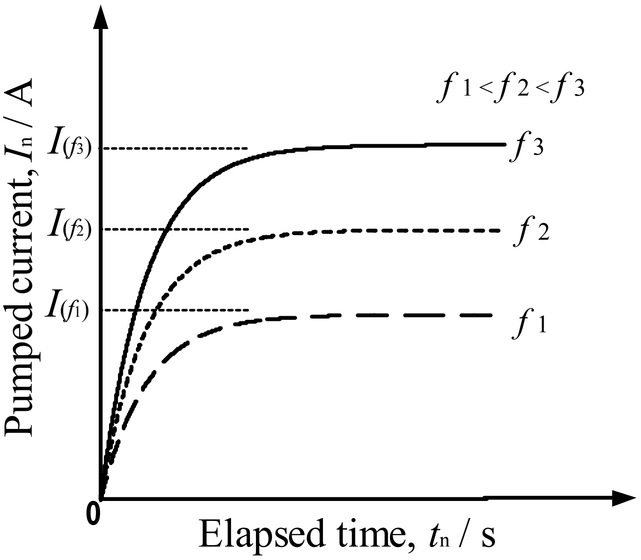

Fig. 2.17 Schematic drawing of the relation between the current pumping and the driving frequency *f*.

Fig. 2.16 shows the relation between the maximum value of the pumped current and the amplitude of the applied magnetic flux, based on the modified equation (2.30). If the values of L and f are constant, the pumped current is changed in proportion to the amplitude of Φ in the figure.

Fig. 2.17 displays the relation between the current pumping and the driving frequency based on the modified equation (2.30). The pumping current is proportional to the driving frequency. In the LTMFP, the higher frequency operation surely results in the larger total fluxes at the same operation time.

The above-mentioned characteristics of the LTMFP based on the analytical equations are confirmed by means of the various experiments carried out in chapter 5.

2.4 Summary

In this chapter, the LTMFP has been proposed as a new type of superconducting power supply. The operating merits of the LTMFP have been explained. In addition, the theoretical equation of the pumping current has been introduced in order to explain operating characteristics in various conditions of operating speed. The obtained results are summarized as follows:

(1) Compared with earlier developed the rotating type flux pump, the LTMFP system has two merits; firstly, mechanical vibration and electric noise can be reduced because a rotating system is not required. Secondly, as the LTMFP is operated by the driving frequency of 3-phase current, the system doesn’t need two PCSs any more. For this reason, no thermal loss is generated by the operation.

(2) The already suggested analytical equation could not explain the current pumping characteristics under the wide range of driving frequencies. In order to solve the problem, analytical pumping equations were modified by the use of the phenomenon of the enhancement of the normal spot in the moving penetration flux. This phenomenon can explain the enlargement of the region of the normal spot according to the moving speed of the applied magnetic field, i.e., driving frequency. This conceptual phenomenon is based on the magnetic diffusion of the superconductor.

Chapter 3 Analysis of Magnetic Behavior in the Superconducting Nb Foil

3.1 Introduction

In this chapter, the magnetic behavior of the superconducting Nb foil that is utilized for the LTMFP is analyzed based on the 3-dimensional finite element method (3D-FEM). The fabricated structure of the LTMFP (see chapter 4) is directly modeled for precise analysis. Because the electromagnetic phenomenon of the superconducting Nb foil is complicated and nonlinear depending on the experienced magnetic field, the phenomenological *J-E* constitutive equation is introduced. The profiles of the magnetic flux density in the fabricated LTMFP are investigated based upon FEM analysis. Further, the operating conditions such as driving frequency of AC current are discussed for the determination of the operation condition. The validity of phenomenon of enhancing the normal spot in superconductor (chapter 2), which is based on the magnetic diffusion, is also confirmed and discussed.

3.2 Analysis Method

The analysis is carried out by the commercial simulation programs: FEMAP® for pre- and post-processor and Photo-series EDDY® for the solver.

3.2.1 Governing equation

The governing equations for the electromagnetic field analysis are expressed based on Maxwell's equations as follows [92],

$$\nabla \times \boldsymbol{H} = \boldsymbol{J}_{\mathbf{0}} + \boldsymbol{J}_{\mathbf{e}} \tag{3.1}$$

$$\nabla \times \boldsymbol{E} = -\frac{\partial \boldsymbol{B}}{\partial \boldsymbol{t}} \tag{3.2}$$

$$\nabla \cdot \boldsymbol{J}_{\mathbf{e}} = 0 \tag{3.3}$$

$$\nabla \cdot \boldsymbol{B} = 0 \tag{3.4}$$

where $\boldsymbol{E}$ is the electric field intensity, $\boldsymbol{H}$ the magnetic field intensity, $\boldsymbol{B}$ the magnetic flux density, $\boldsymbol{J_0}$ the forced current density, and $\boldsymbol{J_e}$ the eddy current density, respectively. The displacement current has been neglected in this study.

The vectors $\boldsymbol{B}$ and $\boldsymbol{H}$ are related with the aid of the permeability μ (H/m) of the medium as,

$$\boldsymbol{B} = \mu\boldsymbol{H} = \mu_0\mu_r\boldsymbol{H} \tag{3.5}$$

where μ_0 and μ_r are the permeability for vacuum ($4\pi\times10^{-7}$ H/m) and relative permeability (μ_r for iron is around 1000), respectively. $\boldsymbol{J_e}$ is related to $\boldsymbol{E}$ through the electrical conductivity σ (S/m) as,

$$\boldsymbol{J_e} = \sigma\boldsymbol{E} \tag{3.6}$$

The magnetic vector potential $\boldsymbol{A}$ (Wb/m) is defined as follows.

$$\boldsymbol{B} = \nabla\times\boldsymbol{A} \tag{3.7}$$

Applying equation (3.7) to equation (3.2) yields

$$\nabla\times(\boldsymbol{E} + \frac{\partial\boldsymbol{A}}{\partial t}) = 0 \tag{3.8}$$

Considering scalar potential φ and using $\nabla\times\nabla\varphi = 0$, then we obtain

$$E = -\frac{\partial\boldsymbol{A}}{\partial t} - \nabla\varphi \tag{3.9}$$

Also, from equations (3.5) and (3.7), we obtain

$$\boldsymbol{H} = \frac{\nabla\times\boldsymbol{A}}{\mu} \tag{3.10}$$

Applying equation (3.10) to equation (3.1)

$$\nabla\times\left(\frac{1}{\mu}\nabla\times\boldsymbol{A}\right) = \boldsymbol{J_0} + \boldsymbol{J_e} \tag{3.11}$$

From equations (3.6) and (3.9), equation (3.11) becomes

$$\nabla\times\left(\frac{1}{\mu}\nabla\times\boldsymbol{A}\right) = -\sigma\left(\frac{\partial\boldsymbol{A}}{\partial t} + \nabla\varphi\right) + \boldsymbol{J_0} \tag{3.12}$$

Applying the vector identity,

$$\nabla\times(\nabla\times\boldsymbol{A}) = \nabla(\nabla\cdot\boldsymbol{A}) - \nabla^2\boldsymbol{A} \tag{3.13}$$

and Coulomb gauge

$$\nabla\cdot\boldsymbol{A} = 0, \tag{3.14}$$

the equation (3.12) is finally converted to

$$\frac{1}{\mu}\nabla^2 \boldsymbol{A} = \sigma\left(\frac{\partial \boldsymbol{A}}{\partial t} + \nabla\varphi\right) - \boldsymbol{J}_0 \tag{3.15}$$

3.2.2 *J-E* constitutive relation

Since the properties of the nonlinear superconductors are typically characterized as current density ***J***, vs. electric field ***E***, (*J-E*) constitutive relation, the following power law expression is usually utilized for convenience.

$$E = E_{\mathrm{c}}\left(\frac{|\boldsymbol{J}|}{J_{\mathrm{c}}(\mu_0|\boldsymbol{H}|)}\right)^n \frac{\boldsymbol{J}}{|\boldsymbol{J}|} \tag{3.16}$$

where the parameter n is the power-law index and denotes the sharpness of the take-off of the *J-E* curve. In other words, n shows the nonlinearity of the superconducting properties. The parameter E_{c} means the electric field criterion for the definition of the critical current density J_{c}, which is varied as a function of $\mu_0\boldsymbol{H}$. Typical value of E_{c} is 1 µV/cm. The parameter $\mu_0\boldsymbol{H}$ denotes the magnetic field. The component of $\mu_0\boldsymbol{H}$ with respect to ***J*** only contributes to the energy dissipation, and the so-called force-free term, i.e., $\boldsymbol{J}|\mu_0\boldsymbol{H}|$ is disregarded. Further, as can be seen in equation (3.16), it is assumed that the direction of ***E*** is always parallel to that of ***J***. Therefore the equivalent electric conductivity σ_{s} is given as [93], [94]

$$\sigma_{\mathrm{s}} = \left|\frac{\boldsymbol{J}}{\boldsymbol{E}}\right| = \frac{J_{\mathrm{c}}(\mu_0|\boldsymbol{H}|)}{E_{\mathrm{c}}}\left(\frac{J_{\mathrm{c}}(\mu_0|\boldsymbol{H}|)}{|\boldsymbol{J}|}\right)^{n-1} \tag{3.17}$$

3.2.3 Newton-Raphson method

In this numerical analysis, in order to solve the induced current of the superconducting Nb foil, the Newton-Raphson method for nonlinear equation is applied using an iterative process. Generally, the first derivative of the function $f\ (x)$ is expressed with the use of the n^{th} and $(n+1)^{\mathrm{th}}$ steps as follows

$$\boldsymbol{f}'(\boldsymbol{x}_n) = \frac{\boldsymbol{f}(\boldsymbol{x}_{n+1}) - \boldsymbol{f}(\boldsymbol{x}_n)}{\boldsymbol{x}_{n+1} - \boldsymbol{x}_n} \tag{3.18}$$

The small increased quantity of electric conductivity $\Delta\sigma$ in the superconductor is estimated by use of equation (3.19). Based on the iterative process of the Newton Raphson method, the approached root value of electric conductivity σ_{s_new} is calculated by the use of pre-estimated value of electric conductivity σ_{s_old} as shown in equation (3.20).

$$\Delta\sigma = \Delta\sigma(E,J) = \frac{\partial\sigma}{\partial E}\Delta E + \frac{\partial\sigma}{\partial J}\Delta J \qquad (3.19)$$

$$\sigma_{s\_new} = \sigma_{s\_old} + \Delta\sigma \qquad (3.20)$$

The induced current of superconductor is calculated by the estimated value of electric conductivity through the above-mentioned iterative process [95].

3.2.4 Modeling and conditions

As is already mentioned, the 3-D FEM analysis is performed with the use of the full scale structure of the LTMFP component in this study.

In order to solve the model including superconducting Nb foil effectively, the symmetrical mesh geometry for half part of the full scale of LTMFP along z-axis is modeled as shown in Figs. 3.1 (a) and (b). Figure (a) shows the symmetrical half size of the total system that includes the iron core, DC bias coils, 3-phase AC coils, and air gap. It should be noted that the region of the air gap in between the iron teeth and the Nb foil is subdivided into fine meshes in order to improve its calculation accuracy. Figure

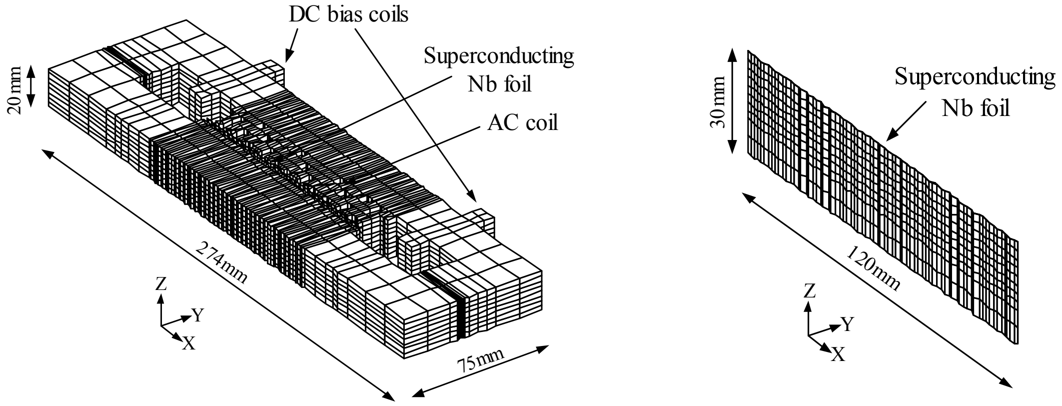

(a) symmetrical half size of total geometry (b) half size of Nb foil (thickness: 20 μm)

Fig. 3.1 3-D meshing geometry of LTMFP.

Table 3.1 Node and element numbers for the half size of LTMFP.

Items	Node number	Element number
Iron core	12916	11278
DC bias and AC coils	9688	8458
Nb foil	4306	3760
Total	26910	23496

(b) shows the half size of the superconducting Nb foil. Table 3.1 provides the information of the mesh geometry of the half of the LTMFP.

In addition, the relative permeability of the iron core and vacuum is 1000 and 1, respectively. The actual properties of the iron core such as hysteretic magnetic behavior and magnetic saturation are not considered for simplicity. The electrical conductivity of the iron is assumed to be 1×10^7 S/m, and that of vacuum is exactly 0 S/m. The DC bias current and AC current for DC and AC coils are, respectively, applied as forced current density (A/m^2). The analysis is performed for different values of AC and DC bias currents. Since the superconducting Nb foil that is utilized for the LTMFP is analyzed, the nonlinear *J-E* expression of the Nb foil (equation (3.16)) is taken into account in order for the precise analysis.

3.3 Results and Discussion

3.3.1 Magnetic flux distributions without the Nb foil

In the case of AC current

In this subsection, the magnetic flux distributions of the iron core and the air-gap are studied by exciting the 3-phase AC current as a first step. Here, the property of the Nb foil is disregarded for simplicity; the property of the mesh in the Nb foil is considered to be that of the air.

Fig. 3.2 shows the magnetic flux distribution of the iron core for the 3-phase AC current at 6 A_{peak} without the DC bias current. This figure is shown as the typical profile of the magnetic flux distribution. The maximum value of the magnetic flux density in the iron core is 569 mT, which is located at x=137 and y=33 mm. It has been observed that the magnetic flux density is concentrated on the central yoke of the iron core at this phase angle.

Fig. 3.3 (a) shows the spatial distributions of the magnetic flux density in the air-gap for various values of AC current. The analysis position is indicated in Fig. 3.2 (from 77 to 197 mm along x-axis in the air gap). As can be seen, the pole pitch is estimated to be 30 mm, and then the validity of the analysis model is confirmed.

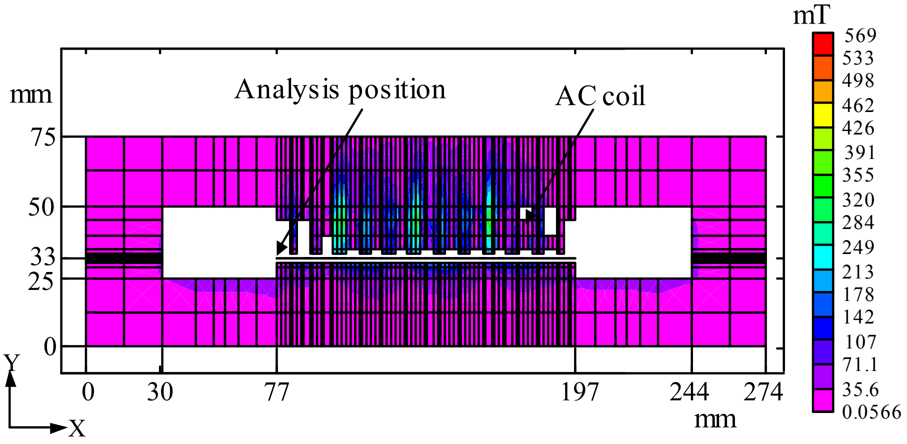

Fig. 3.2 The distribution of magnetic flux density with AC current at 6 A_{peak} in the iron core. The analysis position is also shown as a line.

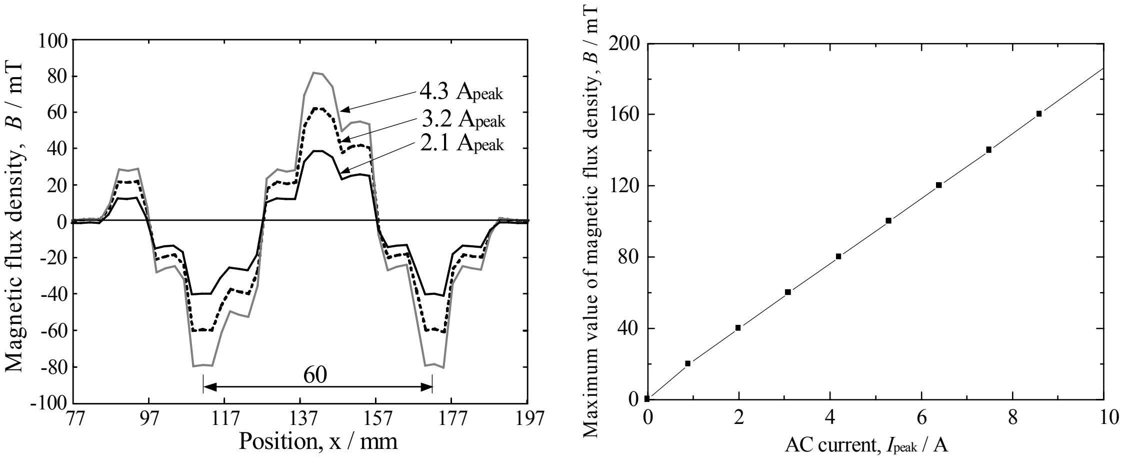

(a) magnetic flux distributions in the air gap

(b) relation between maximum value of magnetic flux density and AC current

Fig. 3.3 Spatial variations of the magnetic flux density for various AC currents in the marked position of Fig. 3.2.

Fig. 3.3 (b) also shows the relation between the maximum values of magnetic flux density and the amplitudes of AC current. Since the nonlinear property as well as saturation of the iron cores is disregarded in this study, this relation is surely linear.

In the case of DC bias current

The relation between amplitude of the magnetic field and DC bias current in the air gap as well as the iron core is also examined based on the analysis.

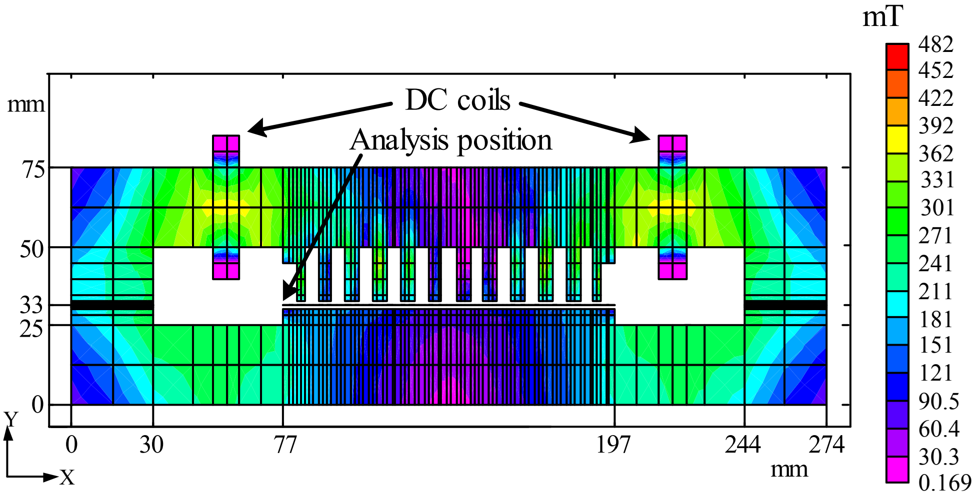

Fig. 3.4 The distribution of magnetic flux density with DC bias current at 10 A in the iron core. The analysis position is also shown as a line.

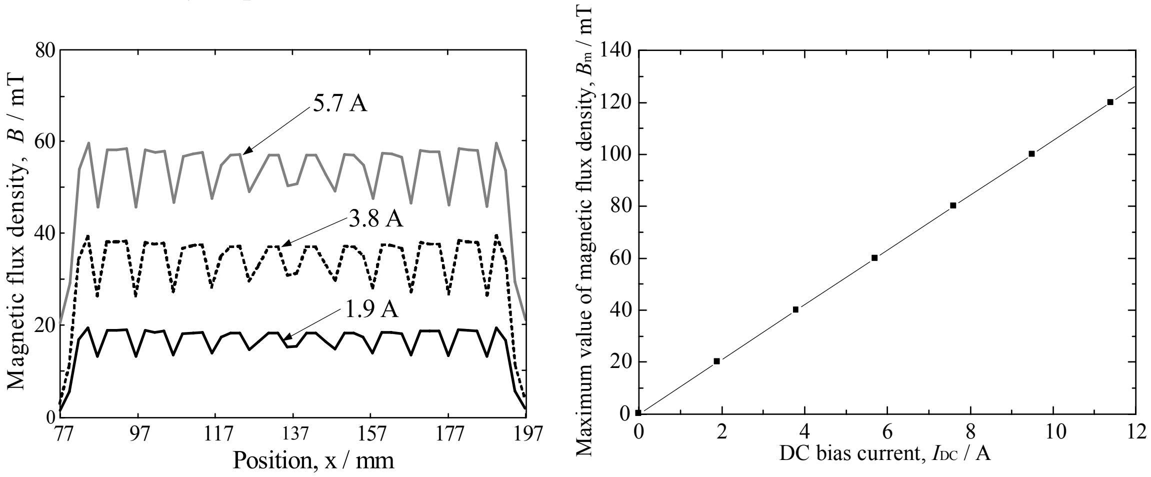

(a) magnetic flux distributions at the air gap (b) relation between maximum values of magnetic flux density and DC bias current

Fig. 3.5 Spatial variations of the magnetic flux density with various AC currents in the marked position of Fig. 3.4.

Fig. 3.4 shows the typical results of the magnetic flux distribution in the core at the *x*-*y* plane with the DC bias current at 10 A. The maximum value of magnetic flux density in the iron core is 482 mT at x= 142 and y=35 mm. As shown, the symmetrical profiles of the magnetic fluxes are surely observed on the left and right hand side.

Fig. 3.5 (a) shows spatial variations of the magnetic flux density for various DC bias currents as typical results. The analysis position for Fig. 3.5 (a) is also illustrated in Fig. 3.4 (from 77 to 197 mm along x-axis in the air gap). The variation of the magnetic flux profiles is due to the teeth of the iron yoke. In addition, Fig. 3.5 (b) shows the relation between the maximum values of magnetic flux densities and the amplitudes of DC current. The relation between B_m and I_{DC} is 10.42 mT/A. Since the appropriate range of the DC bias current realizes the homo-polar traveling magnetic field, these FEM results are utilized for determination of the operation condition of the LTMFP in chapter 5.

In the case of DC bias current and AC current

Here, both the DC bias and AC current are applied as a practical condition and then the magnetic flux distributions are investigated.

Fig. 3.6 shows the contour plots of the magnetic flux density in the iron core for the DC bias current at 10 A and AC current at 6 A_{peak}. Under these current conditions, the maximum value of the magnetic flux density in the iron core is 615 mT. As shown, the contour plot of the magnetic flux is focused on the central teeth of the yoke.

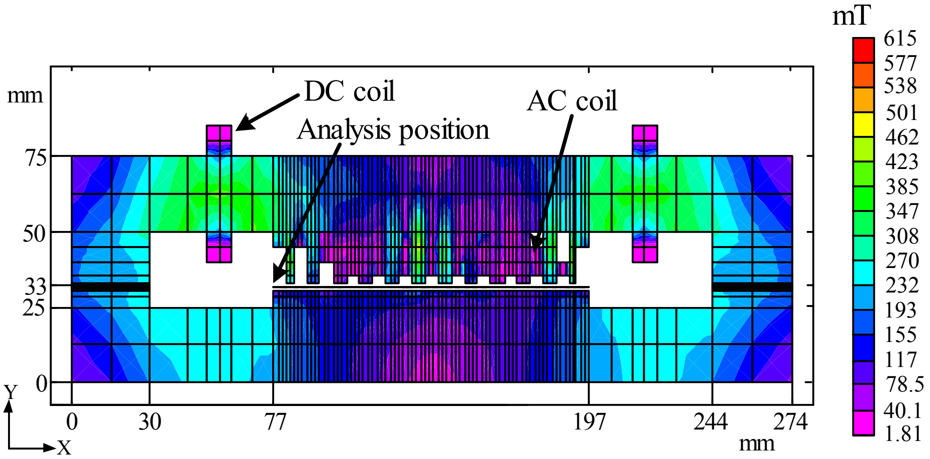

Fig. 3.6 The distribution of magnetic flux density with DC bias current at 10 A and AC current at 6 A_{peak} in the iron core. The analysis position is also shown as a line.

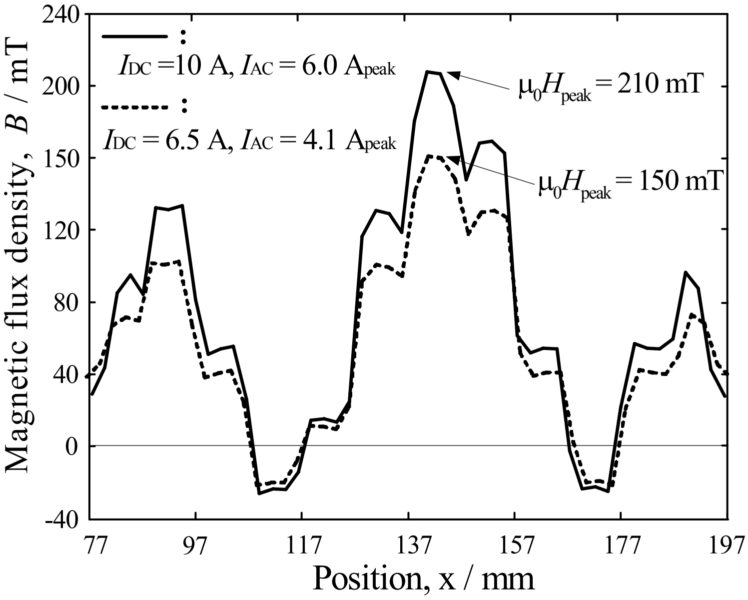

Fig. 3.7 Spatial variations of the magnetic flux density in marked position of Fig. 3.6.

Fig. 3.7 illustrates spatial distributions of the magnetic flux density. The analysis position is shown as the line in Fig. 3.6 (from 77 to 197 mm along x-axis in the air gap). As the superconducting Nb foil is installed in the air gap, if the DC bias current and/or the AC current are so large, the Nb foil will transit into the normal-conducting state. Therefore, the appropriate range of the traveling magnetic field (this value must be between $\mu_0 H_{c1}$ (~100 mT) and $\mu_0 H_{c2}$ (~300 mT)) is a crucial factor to realize the flux pumping behavior. From the simulation results, confirmation of the DC bias current and the AC current is shown in Fig. 3.7. By the combined values of the DC bias current and the AC current, the peak value of traveling magnetic field becomes 210 mT when the DC bias is 10 A and AC current is 6 A_{peak}. The obtained current conditions are referred to the experimental performance in chapter 5.

In addition, the peak value of traveling magnetic field becomes 150 mT when the DC bias is 6.5 A and AC current is 4.1 A_{peak}. The variations are also shown in Fig. 3.7. The obtained current conditions are referred to the experimental performance in chapter 6.

3.3.2 Magnetic flux distributions in the superconducting Nb foil

The electromagnetic characteristic of the superconducting Nb foil is one of the most important issues for the flux pumping performance. In this subsection, such characteristics are simulated by means of the model, which is developed in subsection 3.2.4. Equation (3.17) is utilized for the nonlinear conductivity of the superconducting Nb foil.

In order to obtain the critical current of Nb foil, the experimental observation of the voltage vs. current (*V-I*) curve is performed as shown in Fig. 3.8. A short sample, 20 mm in length, 2 mm in width, is cut from the original foil, and the measurement is carried out by using a transport method with a four-point configuration at 4.2 K. As can be seen, the clear boundary between superconducting and normal-conducting states exists, with the critical current at 16.28 A. The corresponding critical current density at this temperature is 4.07×10^{8} A/m^2.

From the experimental result and reference [96], the magnetic field dependent of critical current density $J_{\mathrm{c}}\left(\mu_0|\boldsymbol{H}|\right)$ is estimated as follows,

$$J_{\mathrm{c}}\left(\mu_0|\boldsymbol{H}|\right)=4.07\times10^{8}-4.77\times10^{9}\cdot\mu_0|\boldsymbol{H}|\ \ [\mathrm{A/m^2}] \tag{3.21}$$

At the moment, the exact index value n is unknown, so we specify 20 as an adequately large value. The magnetic behavior of the superconducting Nb foil is simulated with above-mentioned J_{c} expression.

Fig. 3.9 shows the contour plots of the magnetic flux density of the superconducting Nb foil. These analyses were performed for the conditions of the DC bias current at 10 A and

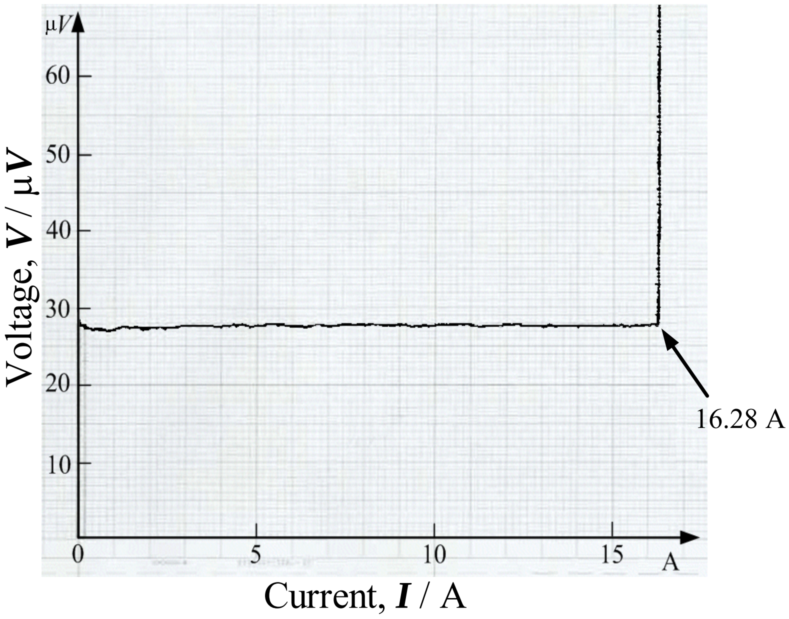

Fig. 3.8 Measured *V-I* curve of the Nb foil at 4.2 K (20 mm × 2 mm × 20 μm).

the AC current at 6 A_{peak}. The driving frequencies are changed from 5 to 60 Hz. The upper surface of each figure is a symmetrical plane; the half of the superconducting Nb foil is only shown in the figure. The analysis time for every frequency is about 26 hours.

As shown, two peaks of the penetrated areas of the magnetic fluxes in the Nb foil are realized because of the invasion of traveling magnetic fluxes. It can be seen that the region at which the magnetic fluxes invade in the foil slightly enlarges with increase in driving frequency. Especially, the regions at 40 and 60 Hz are larger than those at the lower frequencies. This is due to the diffusion properties of the invaded magnetic fluxes in the superconducting Nb foil. In other words, the moving magnetic fluxes experience a viscous force. Then, the characteristic diffusion time is necessary in order to respond to the variation of the traveling magnetic field.

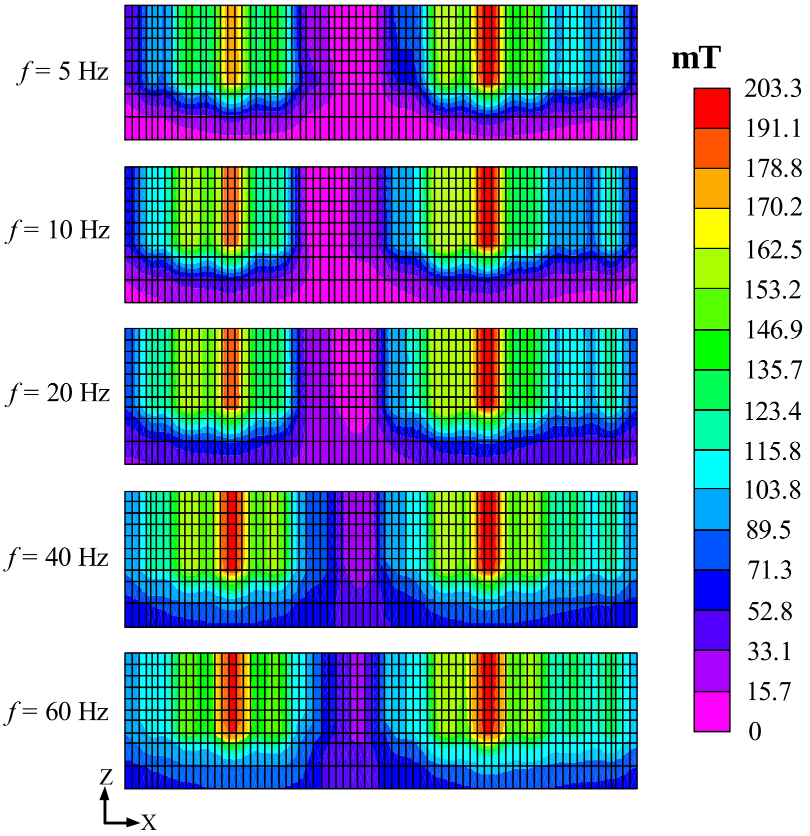

Fig. 3.9 Contour plots of the magnetic flux density in the Nb foil for different driving frequencies with the DC bias current at 10 A and the AC current at 6 A_{peak}. The upper surface is the symmetrical plane of the upper part. The electrical angle of the A-phase is 120^{o}.

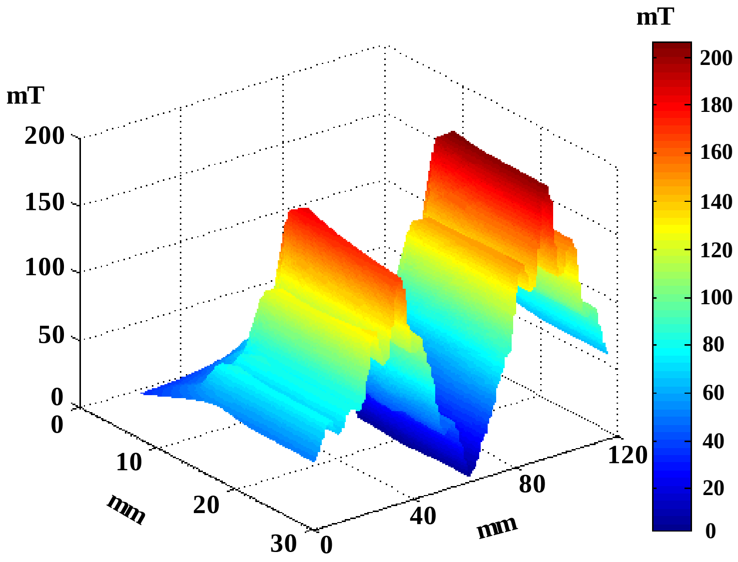

Fig. 3.10 Spatial distribution of the magnetic flux density at f = 60 Hz obtained from Fig. 3.9.

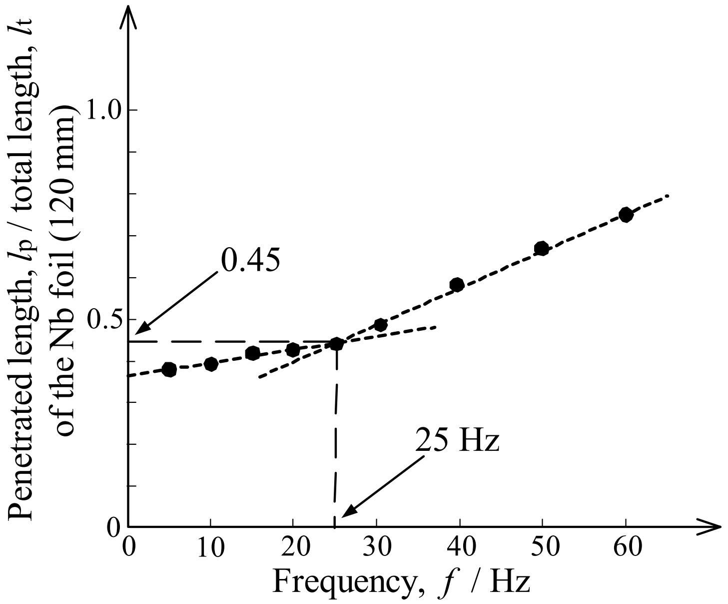

Fig. 3.11 Calculated results of the invaded magnetic flux normalized by the total length of the Nb foil (120 mm). The criterion for the definition of the invaded area is 100 mT ($\mu_0 H_{c1}$).

Fig. 3.10 also shows the corresponding spatial waveform of the magnetic flux density for f = 60 Hz as a typical result in a traveling magnetic field. Here, the invasion areas of the magnetic fluxes are estimated for the different frequencies at the criterion of 100 mT as shown in Fig. 3.11.

Fig. 3.11 shows the calculated results of the invaded flux length as a function of the frequency. The penetrated length is normalized by the total length (120 mm) of the Nb foil. The symbols of l_p and l_t represent the penetrated length and the total length of the superconducting Nb foil, respectively. As can be clearly seen, the gradient of l_p / l_t vs. f curve varies at 0.45 at 25 Hz. That is, when the frequency is lower than 25 Hz, the ratio of l_p / l_t slightly increases. The increment rate in this case is 0.095 mm/Hz.

On the other hand, the increment rate becomes larger in case that the frequency is higher than 25 Hz. The ratio of l_p / l_t reaches 0.76 at 60 Hz, and the corresponding increment rate is 0.324 mm/Hz. This means the increment rate changes to have different value around 25 Hz. That is, the characteristic time of magnetic diffusion t_{md} in the Nb foil of the LTMFP is about 40 ms ($=\frac{1}{25\ \mathrm{Hz}}$).

We can roughly calculate the characteristic time of the magnetic diffusion of the Nb foil in the LTMFP using equation (2.28) as follows

$$t_{md} = \frac{(2a)^2}{\pi^2 D_m} = \frac{(2a)^2}{\pi^2 \left(\frac{\rho}{\mu_0}\right)} = \frac{(0.06\mathrm{m})^2}{\pi^2 \times \left(\frac{1\times10^{-8}\,\Omega\mathrm{m}}{4\pi\times10^{-7}\,\mathrm{H/m}}\right)} = 46\,\mathrm{ms} \tag{3.22}$$

where, the width of Nb foil, 2a is 60 mm, and the magnetic diffusivity is $D_m = \rho / \mu_0$ (ρ (=1×10^{-8} Ωm): electrical resistivity in the normal-conducting Nb foil, μ_0 (= $4\pi\times10^{-7}$ H/m): permeability in vacuum).

This means that the corresponding characteristic frequency f_t is 21.7 Hz ($=\frac{1}{46\ \mathrm{ms}}$). This value agrees with the simulation results, and the validity of the simulation code is confirmed.

Furthermore, the assumption in chapter 2, at which the normal spot in the superconducting Nb foil will be enhanced depending on the driving frequency, is realized numerically.

3.4 Summary

In this chapter, the simulation code of the characteristics of the superconducting Nb foil in the LTMFP is developed based on the 3-D FEM. The nonlinear *J-E* constitutive relation of the superconducting Nb foil is approximated by widely used power law curve, and the magnetic field dependent of the critical current of the Nb foil is taken into account based on the experimental results. The obtained results are summarized as follows:

(1) The appropriate conditions of the DC bias and AC current are determined in order to realize homo-polar traveling magnetic fields through the observation of the temporal variation of the magnetic flux distribution in the air-gap.

(2) The normal spot size at which the magnetic fluxes penetrate into the superconducting Nb foil changes depending on the driving frequency. Its size enlarges with increase in frequency. The normal spot size is estimated by the criterion, at which the magnetic flux reaches 100 mT. The rate of increase is 0.095 mm/Hz for $f \leq 25$ Hz. On the other hand, when the frequency increases beyond 25 Hz, the rate becomes larger at 0.324 mm/Hz. This means that the characteristic time of magnetic diffusion of the moving magnetic field t_{md} is 40 ms $(= \frac{1}{25\ \mathrm{Hz}})$.

(3) The simulated result of characteristic time t_{md} 40 ms $(= \frac{1}{25\ \mathrm{H}z})$ coincided with the calculated result 46 ms $(= \frac{1}{21.7\ \mathrm{H}z})$, and this value agrees with simulation result. This phenomenon is to be experimentally confirmed in chapter 5.

Chapter 4 Fabrication of the LTMFP System

4.1 Introduction

In this chapter, the fabrication procedures of the proposed LTMFP system and their assembly are described in detail. In addition, two types of superconducting magnets and a thermal-type PCS have been fabricated in order to estimate the operating characteristics of LTMFP. Our experimental LTMFP system includes three components as shown schematically in the connection diagram of Fig. 4.1.

The first component is the main body of the LTMFP that produces a pumped current. The symbols I_n, l, I_{DC}, and I_{AC} represent the pumped current, the inductance of superconducting Nb foil, the DC bias current, and the 3-phase AC current, respectively. The second is a superconducting Nb-Ti load magnet (L denotes self-inductance of load magnet), which is connected directly to the LTMFP. The third one is a slow-response thermal-type PCS system S_{p1}, in which the “on” or “off” state is controlled by the use of heater’s current I_{DC2}. The external current source I_{DC1} is also connected to the above-mentioned system for setting the operating current, which is supplied to the load magnet in combination with S_{p1}.

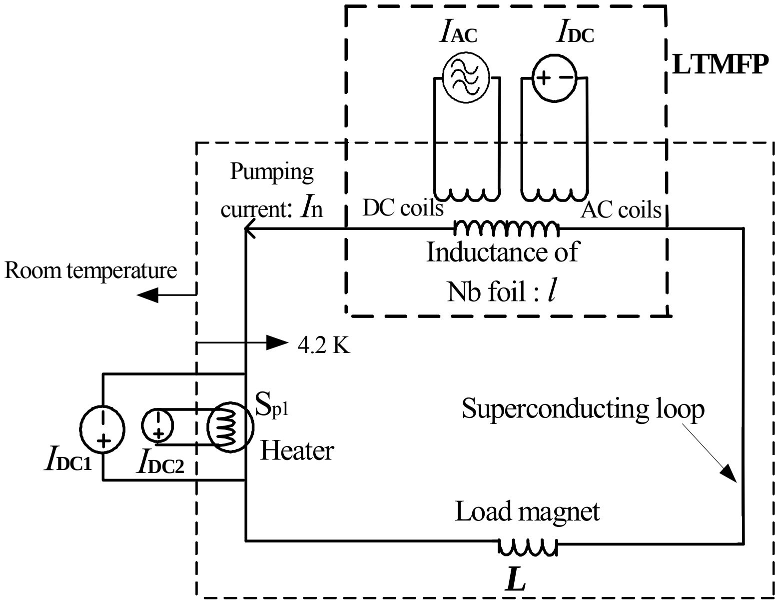

Fig. 4.1 Connection diagram of LTMFP system.

The area surrounded in the dotted square is cooled in a cryogenic temperature at 4.2 K (atmospheric boiling point of liquid helium). The outside of this area is in room temperature. In the following sections, the detailed procedures are presented.

4.2 Structure of LTMFP

The LTMFP is mainly composed of four components as follows; a laminated silicon steel core, a 3-phase superconducting armature coil, a couple of superconducting coils for DC bias, and a superconducting Nb foil. These components are assembled as shown schematically in Fig. 4.2. The superconducting armature coils are wound around the iron teeth with 3-phase and 4-pole configuration [97], [98], and this winding produces a traveling magnetic field. In addition, two DC bias coils are also wound around the upper yoke in order to realize the homo-polar magnetic field, i.e., the traveling magnetic field is pushed up by using the DC bias field. It should be noted here that these DC windings have to be wound in an opposite direction to each other in order to focus the DC bias field on the iron teeth (see Fig. 4.2). The strip of Nb foil is installed in between the iron teeth and the lower iron core with the air gap length at 3 mm. A more detailed explanation is described from subsection 4.2.1 to 4.2.5.

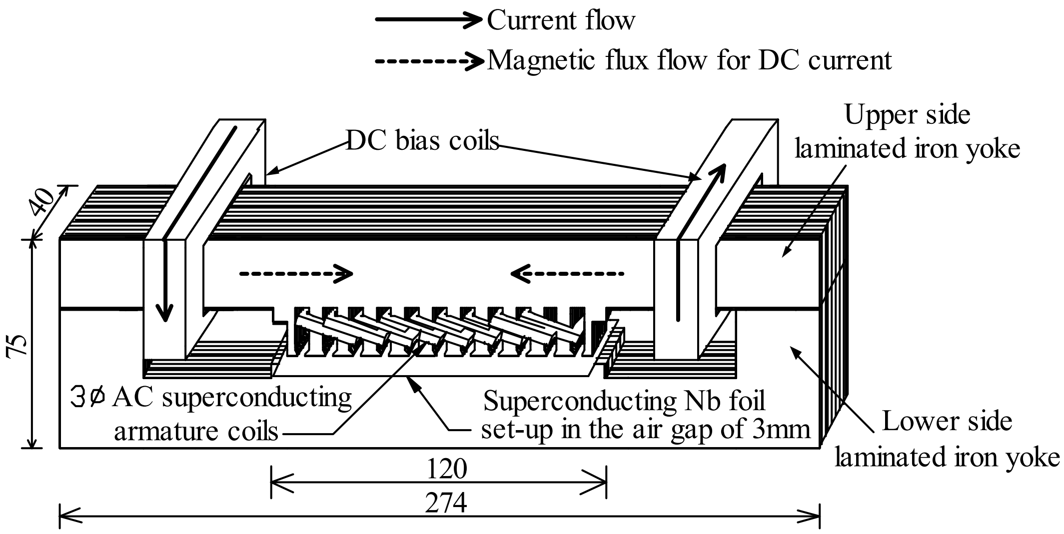

Fig. 4.2 Schematic diagram of the LTMFP (unit: mm).

4.2.1 Laminated silicon steel core

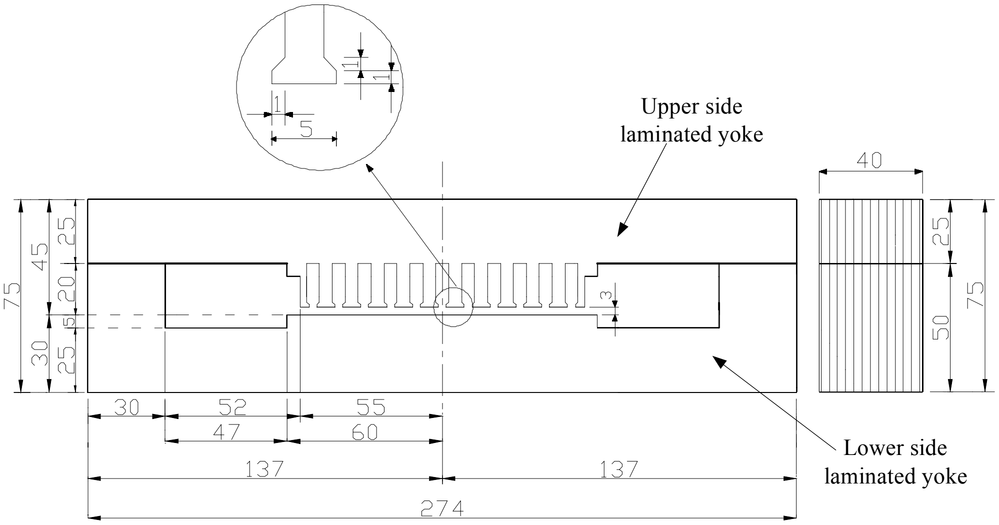

Fig. 4.3 Design diagram of laminated silicon steel core (unit: mm).

The laminated steel core was originally manufactured by a typical discharge process. Silicon steel, 0.35 mm in thickness, is utilized for the fabrication of the cores in order to reduce core-loss. The detailed design diagram is shown in Fig. 4.3. The dimensions of the laminated silicon steel core are 274 mm in length, 75 mm in height, and 40 mm in width. First, the core is cut into the upper and lower parts in order to conveniently wind the DC bias coil. These cores are connected to each other by using a supporting frame. For the winding of the AC coils, there are 12 teeth, and the slot depth and width are 15 mm and 5 mm, respectively.

4.2.2 Three-phase superconducting armature coils

Fig. 4.4 shows the configuration of the segments for the 3-phase armature windings. The current direction is also illustrated with arrows in the same figure. A short-pitch and double-layer method is introduced for the 3-phase and four pole armature winding,

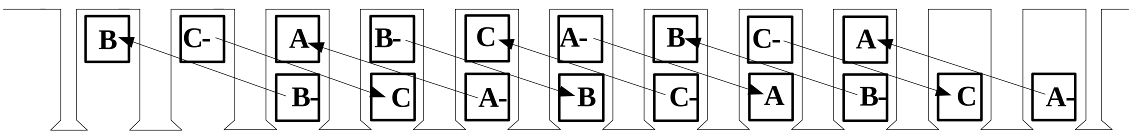

Fig. 4.4 Schematic diagram of the AC winding arrangement.

Table 4.1: Parameters and specifications of the Nb-Ti superconducting AC wire.

Wire/Cu	Nb-Ti (1/ 0.16)
Critical current I_c	42 $A_{\mathbf{peak}}$ @ 4.2 K, 50 Hz
Bare wire diameter	0.6 mm
Structure	6(+1)
Diameter including insulation part	0.71 mm
Twist pitch, direction	1.4 mm, S
Diameter of matrix	0.2 mm
R_{295k} / R_{10k}	8.5

DC magnetic field	**DC critical value @ 4.2 K**	**AC critical value (@ 4.2 K , 50 Hz)**
0 T	160 A	67 $\mathbf{A}_{\mathbf{peak}}$
0.5 T	67 A	57 $\mathbf{A}_{\mathbf{peak}}$
1 T	33 A	42 $\mathbf{A}_{\mathbf{peak}}$
2 T	13 A	20 $\mathbf{A}_{\mathbf{peak}}$
3 T	5.9 A	11 $\mathbf{A}_{\mathbf{peak}}$
4 T	3.7 A	-
5 T	2.0 A	-

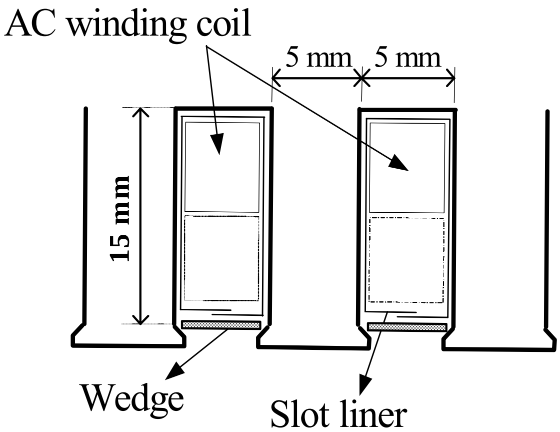

Fig. 4.5 Magnification diagram of 3-phase armature winding and laminated slots.

which produces a traveling magnetic field. The moving speed of the magnetic field is in proportion to the frequency of the 3-phase current. Therefore, the speed of the magnetic field can be controlled by the use of the 3-phase inverter [99], [100].

The copper stabilized Nb-Ti wires fabricated for the purpose of AC applications are used for windings. The turn number and length per phase of the wire are 40 and 25 m, respectively. Table 4.1 provides specifications of the subject wire.

Fig. 4.5 shows the enlarged diagram for the slotted windings. The wedge's function is to fix the AC armature coil. The slot liner, which is made of a thin plastic film, keeps the electrical insulation between the laminated silicon steel core and the armature coil [101]. The thickness of the slot liner is 0.14 mm.

4.2.3 Superconducting DC bias coils

Fig. 4.6 illustrates the schematic diagram of the magnetic flux flow in a laminated silicon steel core by means of a couple of DC bias coils. In order to focus the magnetic flux into the air gap, the direction of the DC current is opposite one another as shown in the figure [102].

The structure of the bobbin for the DC bias coil is shown in Fig. 4.7. It is commonly known that the current transport properties of the superconducting wires degrade when the wires bent with steep angle. Therefore, the space bars, which are made of Bakelite, are put near the edges of the bobbin in order to enlarge the bending angle. These dimensions of the bar are 5 mm in width, 20 mm in length, and 0.5 mm in thickness, respectively.

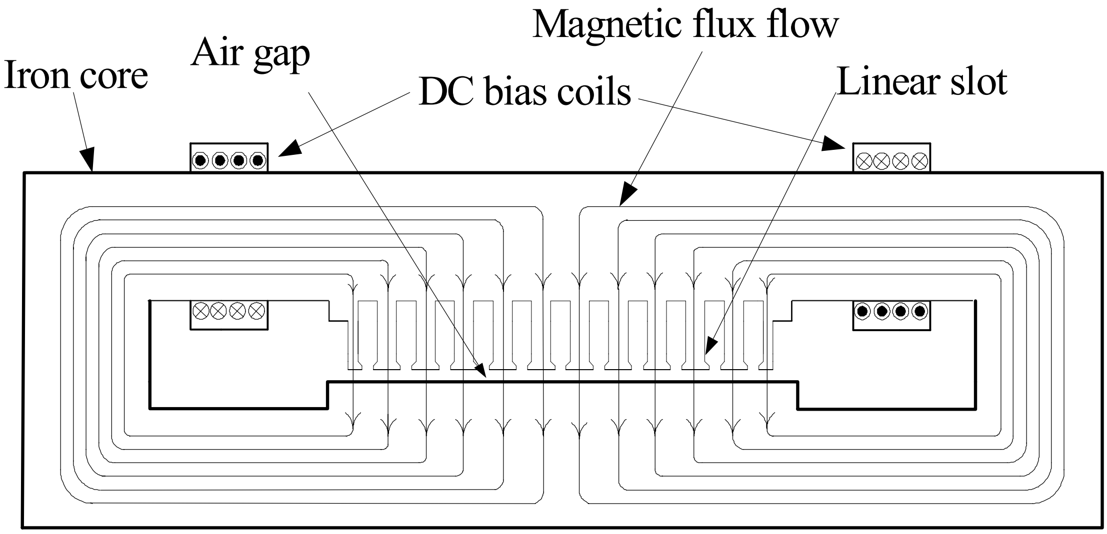

Fig. 4.6 Schematic diagram of the magnetic flux flow by DC bias currents.

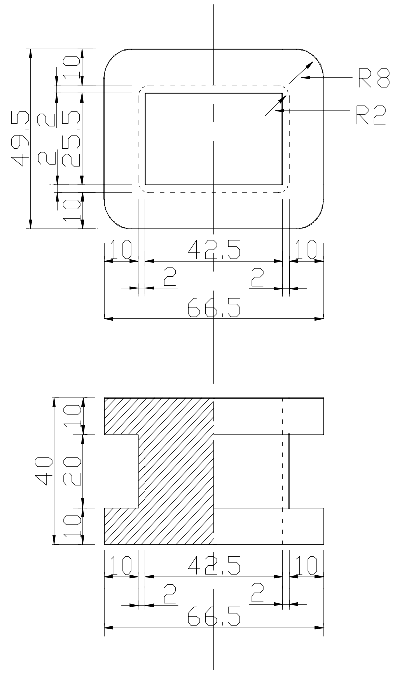

Fig. 4.7 Design diagram of the bobbin for DC bias coil.

Table 4.2 Parameters and specifications of the Nb-Ti superconducting DC wire.

Wire	Nb-Ti /Cu (1/3.2)
Wire diameter	0.9 mm
Turns / coil	132
Length / coil	23 m
Inside dimension	3 mm × 4.6 mm
Outside dimension	4.8 mm × 6.2 mm
Twist pitch, direction	26 mm, S
Filament number	40
Filament diameter	62 μm
DC critical current	930 A / @ 1 T, 620 A / @ 2 T,
	310 A / @ 4 T, 250 A / @ 5 T

The DC bias coils are fabricated by the use of the Nb-Ti superconducting wire for DC use. The surface of every layer of the Nb-Ti coil is covered with Stycast® 1266 to prevent wire movement during operation. Table 4.2 provides specifications of the superconducting DC wire.

4.2.4 Superconducting Nb foil

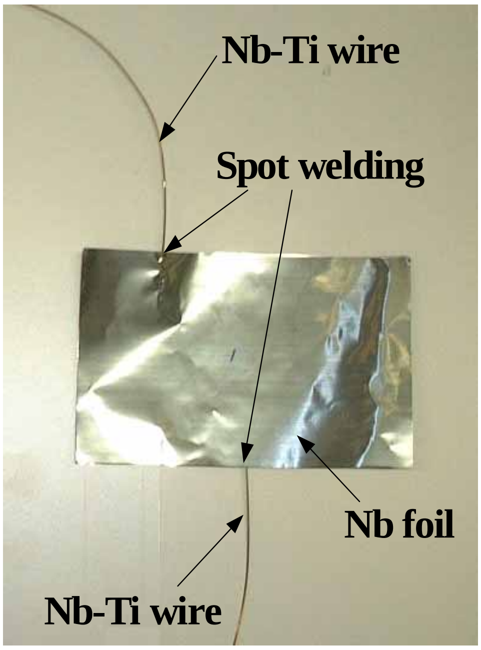

Fig. 4.8 Photograph of Nb foil (120 mm × 60 mm × 20 μm) connected to the terminals of the Nb-Ti superconducting load magnet (see section 4.3).

The superconducting Nb foil, which size is 120 mm in length, 60 mm in width, and 20 μm in thickness, is installed in the air gap of the LTMFP as marked in Fig. 4.2. Both terminals of the superconducting Nb-Ti load magnets (see section 4.3) are connected to this foil by spot welding, for the configuration of the superconducting closed loop as shown in Fig. 4.8. Further, in order to fix the Nb foil in the air gap, the foil is sandwiched in between a couple of translucent aluminum nitride ceramic thin plates (0.5 mm in thickness) which possess high thermal conductivity in liquid helium. The connection length and resistance value of the welding area between the Nb foil and the Nb-Ti wire are 20 mm and 1.2 nΩ, respectively.

4.2.5 Assembly of LTMFP

All components, which were explained in subsection 4.2.1-4.2.4, are assembled as shown in Fig. 4.9. The windings of the assembled LTMFP are covered with epoxy resin in order to prevent the wire movement.

After the assembly is completed, the inductances of the DC bias coils as well as the 3-phase armature coils are measured for different frequencies at room temperature.

Fig. 4.10 (a) shows measured results for the DC bias coils, and both of left- and right-hand side coils keep the same values of inductance. This balancing is important for the realization of the uniform homo-polar traveling field. The measured results for 3-phase coils are also shown in Fig. 4.10 (b). As shown, the inductance values are below 3 mH under the frequency range from 40 to 100 Hz, balancing each other.

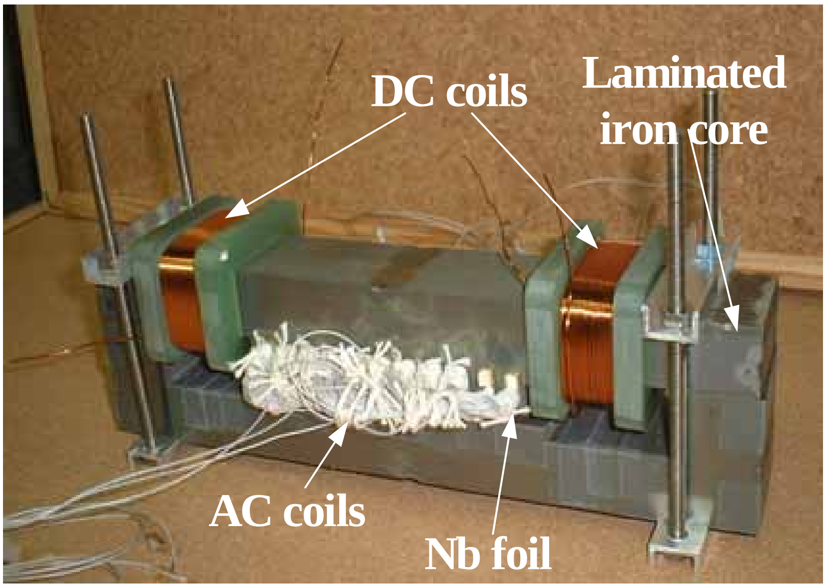

Fig. 4.9 Photograph of the assembled LTMFP.

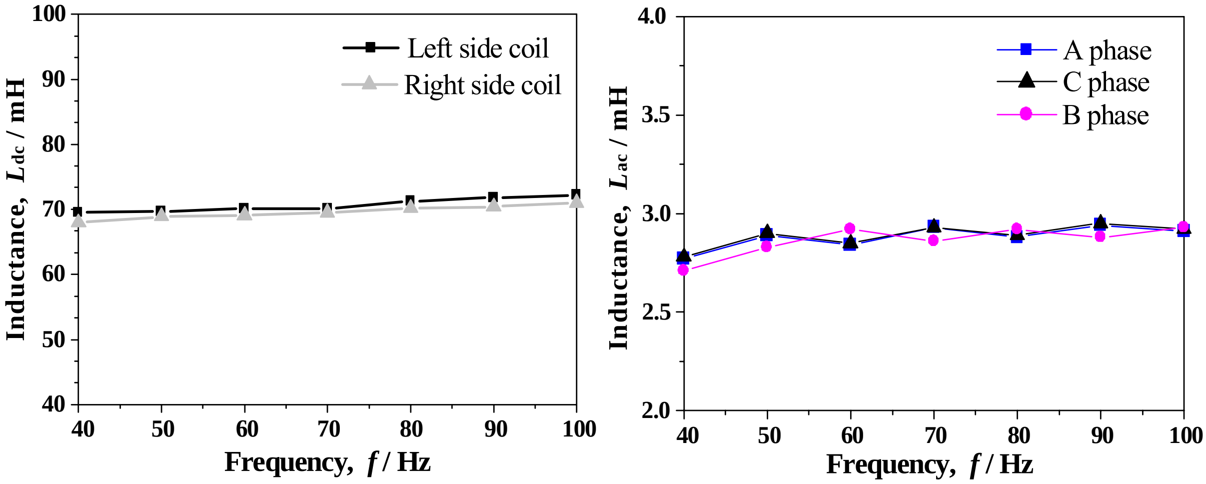

(a) DC bias coils

(b) 3-phase armature coils

Fig. 4.10 Measured results of the inductance value at room temperature.

4.3 Load Magnets

In this section, two types of load magnets are fabricated, i.e., a small-scale single solenoid magnet (1.3 mH) and a toroidal magnet (543 mH). In order to check the basic operating performance of the LTMFP, the small-scale magnet is utilized. The toroidal load magnet, on the other hand, is introduced for the practical current compensation experiment in order to reduce the leakage magnetic field.

4.3.1 Small-scale load magnet

The small-scale load magnet is wound using an Nb-Ti DC superconducting wire, which is 0.9 mm in diameter. The frame bobbin is made of GFRP (glass fiber reinforced plastic); its dimensions are shown in Fig. 4.11 (a). The photograph of the fabricated magnet is also shown in Fig. 4.11 (b).

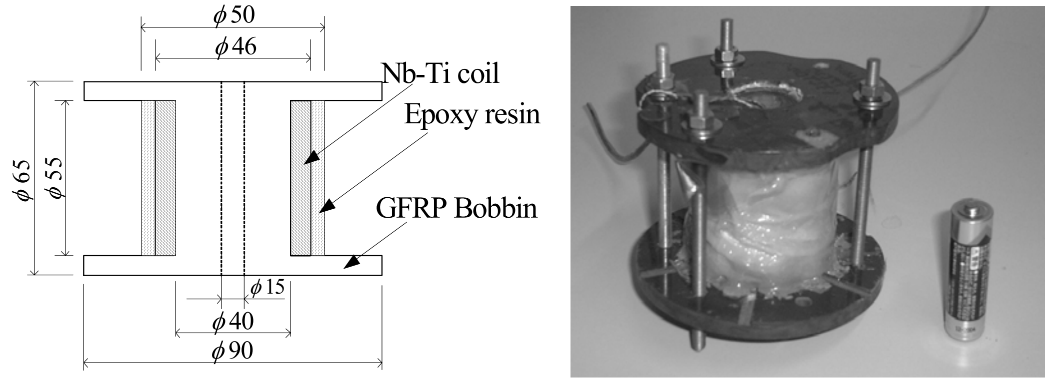

(a) Schematic diagram (b) fabricated photograph

Fig. 4.11 Structure and photograph of the small-scale load magnet (1.3 mH).

Table 4.3 Specifications of the small-scale load magnet.

Cupper ratio	Nb-Ti /Cu (1/3.2)
Wire diameter	0.9 mm
Turns	279
Length / coil	32 m
Inner diameter of frame	40 mm
Height of the frame	56 mm

The wound magnet is covered with epoxy resin in order to reduce wire movement. The inductance and total wire length are 1.3 mH and 32 m, respectively. The specifications of the fabricated magnet are also shown in Table 4.3.

4.3.2 Toroidal load magnet

The toroidal magnet consists of six solenoid coils. Design diagram of the solenoid coil for the toroidal load magnet is shown in Fig. 4.12. The bobbin is made of GFRP and the cooling channels (2 mm in diameter) are made for keeping the temperature of superconducting coil at 4.2 K (see Fig. 4.12 (a)). The superconducting Nb-Ti wire is utilized for the solenoid coil, and the laminated iron cores are introduced in order to form the magnetic circuit (see Fig. 4.12 (b)). The dimensions of the inserted iron core are 60 mm in length, 84 mm in width, and 24 mm in thickness, respectively.

Fig. 4.13 shows the fabricated toroidal magnet. For prevention of the saturation of the iron cores, the interval at 1 mm is kept in between each of the iron cores as shown in Fig. 4.13 (a). As the toroidal load magnet keeps the round shape, the leakage flux can be reduced. Fig. 4.13 (b) shows the photograph of one coil in the toroidal magnet. Table 4.4 also provides parameters of the toroidal load magnet. As shown, the inductance values of the coils show 45.4-46.0 mH.

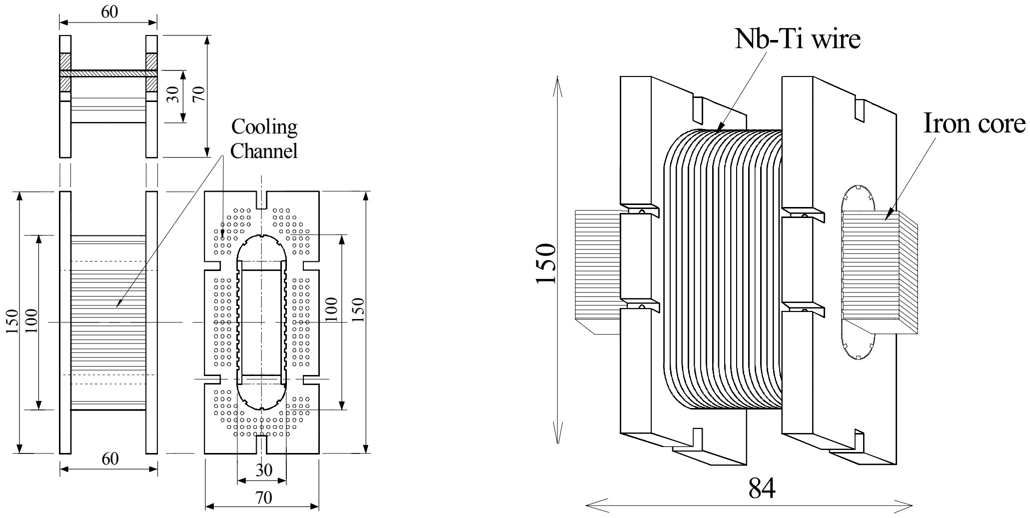

(a) GFRP bobbin (b) assembled solenoid coil

Fig. 4.12 Design diagram of the solenoid coil for the toroidal load magnet.

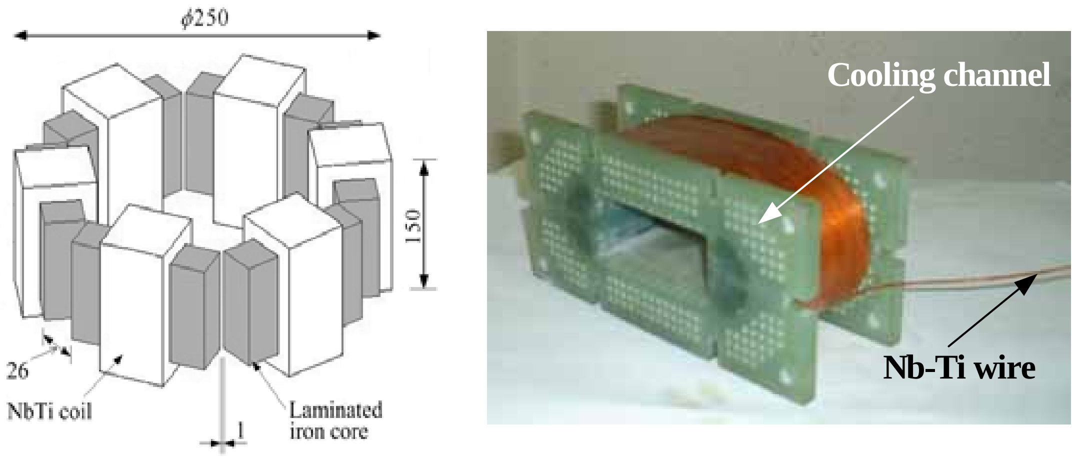

(a) Structure of the assembled toroidal magnet

(b) photograph of the fabricated solenoid coil

Fig. 4.13 Structure of the toroidal load magnet.

Table 4.4 Parameters of the toroidal load magnet.

Wire diameter	0.9 mm
Turns / coil	540
Length / coil	180 m
Layers/ coil	12
Turns / layer	44
Laminated iron core	60 mm × 84 mm × 24 mm
Inductance of the coils	
no.1	46.0 mH
no.2	45.8 mH
no.3	45.7 mH
no.4	45.9 mH
no.5	45.4 mH
no.6	45.8 mH
Total inductance in series	543.0 mH

4.4 Thermal-Type PCS

In our LTMFP system, a thermal-type PCS is installed for the realization of the persistent current mode. This kind of PCS is operated by a heater with a generally slow switching time. Epoxy resin is pasted for every layer of windings for fixation of the wires. In addition, the superconducting wire is uniformly wound on the GFRP cylindrical bobbin by the bifilar manner in order to reduce field inhomogeneity [103]-[105].

The fabricated thermal-type PCS in Fig. 4.14 (a) consists of three components as follows:

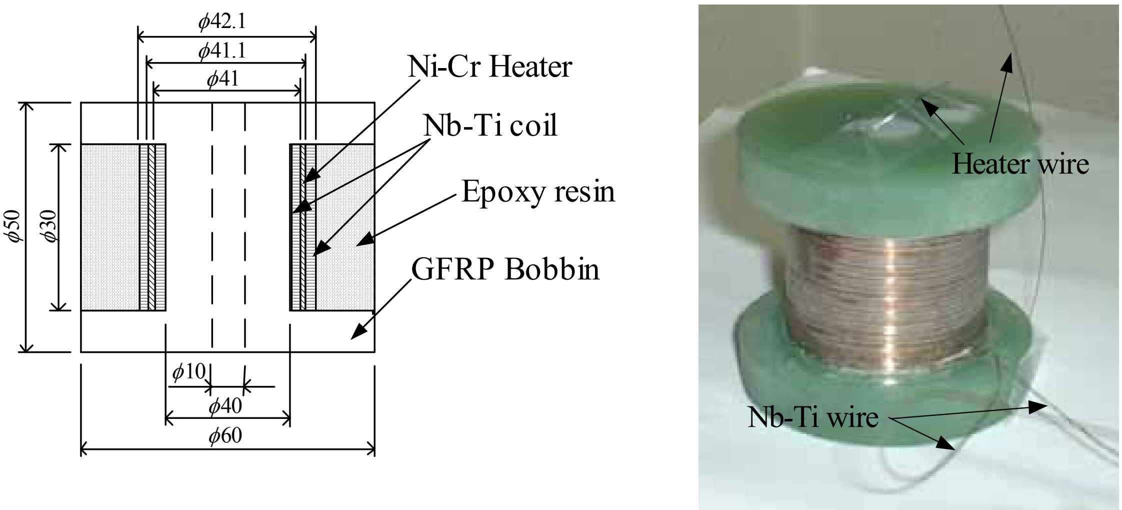

(a) structure of the PCS (b) photograph of the fabricated PCS without epoxy resin

Fig. 4.14 Structure and photograph of the thermal-type PCS.

Table 4.5 Specifications of the fabricated thermal-type PCS.

(Ni-Cr wire)	
thickness	0.05 mm
width	1 mm
total length	2.5 m
resistance at room temperature	128.4 Ω/m
Superconducting Nb-Ti wire	
diameter	0.5 mm
total length	18.2 m
total inductance	21 μH
Thickness of epoxy resin	8.8 mm

The first component is the superconducting coil, which is the Nb-Ti wire with a matrix of Cu-Ni. The second is the heating wire, which consists of the Ni-Cr that has resistance of 128.4 Ω/m at room temperature. This wire is installed in between two kinds of superconducting Nb-Ti windings, allowing a transition to the normal-conducting state by the heating current. The third one is the thermal insulation component (epoxy resin), which encapsulates the Nb-Ti windings [106], [107].

Fig. 4.14 (b) shows the photograph of the fabricated PCS, before pasting the epoxy resin. It should be noted that, since the Nb-Ti wire is wound by the bifilar method [108], [109], the self-inductance of the PCS shows a relatively small value (L: 21 μH). Table 4.5 also provides the specifications of the fabricated thermal-type PCS.

4.5 Summary

In this chapter, the components of the current pumping system, i.e., LTMFP, the load magnet, and the PCS, have been fabricated. The dimension of the fabricated LTMFP was consistent with that of the FEM analysis model (chapter 3). The fabrications of the LTMFP system have been concluded as follows:

First, the LTMFP has been fabricated with the use of superconducting DC and 3-phase AC windings.

Second, two load magnets have been fabricated. A small-scale load magnet of 1.3 mH or a toroidal load magnet of 543 mH is connected with the LTMFP to keep closed the superconducting loop.

Third, a thermal-type PCS was fabricated to supply operating current into the load coil. Since the superconducting Nb-Ti wire has been wound by the bifilar method, the PCS attained a small inductance effectively (L: 21 μH).

Chapter 5 Current Pumping Characteristics of the LTMFP

5.1 Introduction

In this chapter, the fundamental characteristics of the fabricated LTMFP are tested and discussed: We concentrate on the dependent of the driving frequency on the pumping performance. The optimal frequency for the operation of the LTMFP is determined from the experiment. The operating condition, which is obtained from simulation results (chapter 3), is adopted and the enhancement rate of the normal spot size is evaluated by modified equation (2.30). Then, the validity of the modified analytical equation is confirmed. In addition, two types of the superconducting load magnet, i.e., a small scale solenoid magnet (1.3 mH) and a comparatively large scale toroidal magnet (543 mH) are considered in order to investigate the dependent of the inductance value upon the performance, and confirm the calculated enhancement rate of the normal spot size.

5.2 Experimental Setup

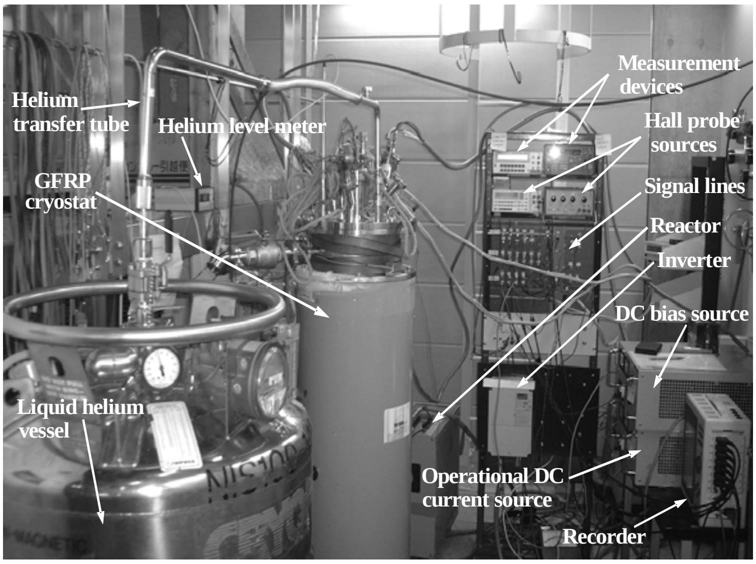

Fig. 5.1 Photograph of the experimental setup.

Fig. 5.1 shows the photograph of the experimental setup. Both the LTMFP and the superconducting load magnet are installed in the GFRP cryostat. In order to carry out the experiment, liquid helium is transferred into the cryostat from the vessel through the helium transfer tube. A PWM inverter is utilized for the operation of the LTMFP.

All measured signals are amplified and recorded into a transient data recorder (HIOKI 8840). In the following subsections, the detailed explanations of the experimental systems will be presented.

5.2.1 Cryogenic configuration

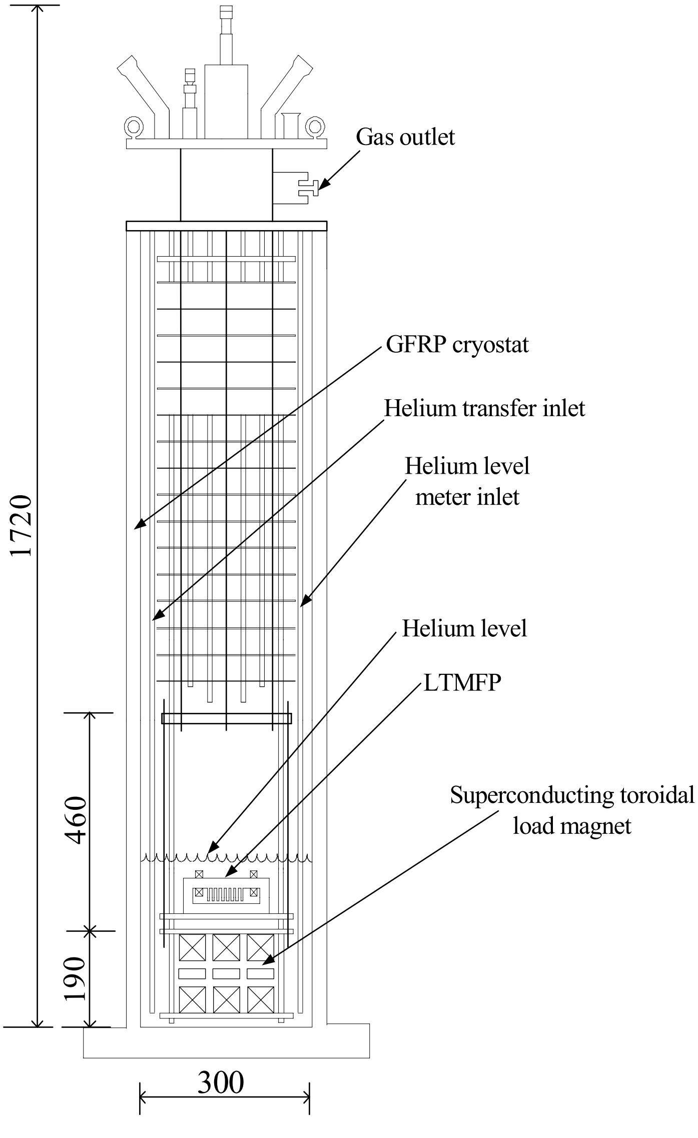

Fig. 5.2 Inner structure of the GFRP cryostat.

Fig. 5.2 illustrates the inner structure of the GFRP cryostat. The LTMFP system as well as the superconducting load magnet is installed at the bottom of the cryostat in order to reduce the liquid helium consumption. The inner diameter of the cryostat is 300 mm and the total height is 1720 mm. The evaporated helium gas in the cryostat flows out through the helium gas outlet. The liquid helium level is monitored via the helium level meter.

5.2.2 Flux pumping systems

Small-scale load magnet

In order to examine the operating conditions of the LTMFP, a small-scale load magnet with the self-inductance at 1.3 mH is connected to the LTMFP. Fig. 5.3 (a) shows the connection diagram of the current pumping system. In this test system, two cryogenic hall sensors are installed, respectively, in the load magnet (axial type) and at the central point in the air gap (transverse type) of the LTMFP. These sensors are used for the measurement of the amplitude of pumped current and the homo-polar traveling magnetic field, respectively. As can be seen in the figure (a), a persistent current loop is realized as Loop 1, i.e., superconducting Nb foil and Nb-Ti coil. They keep a closed loop. The current waveforms of the 3-phase inverter are measured by using shunt resistors, at 50 mΩ. Fig. 5.3 (b) shows the photograph of the assembly of the flux pump system that includes the small-scale load magnet.

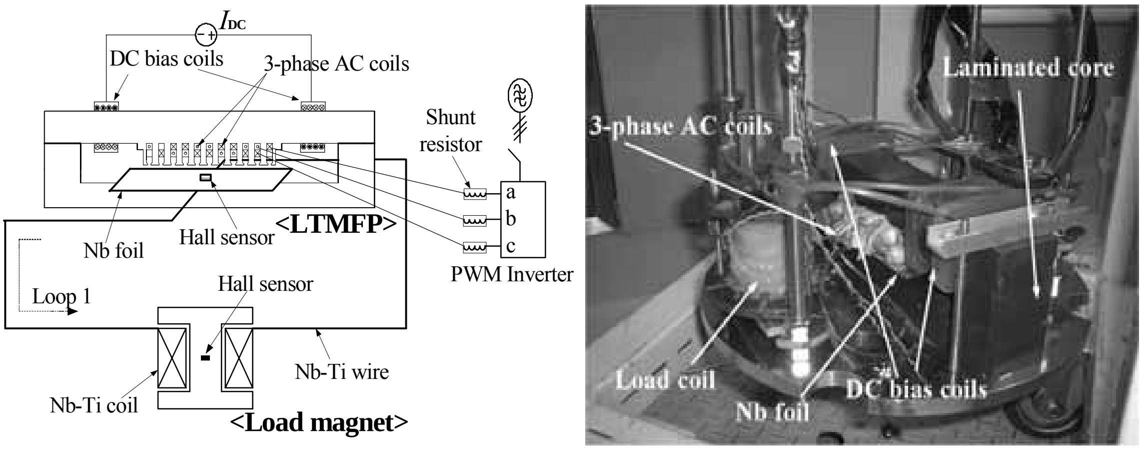

(a) connection diagram (b) assembly photograph

Fig. 5.3 Current pumping system with small-scale load magnet (1.3 mH).

Toroidal load magnet

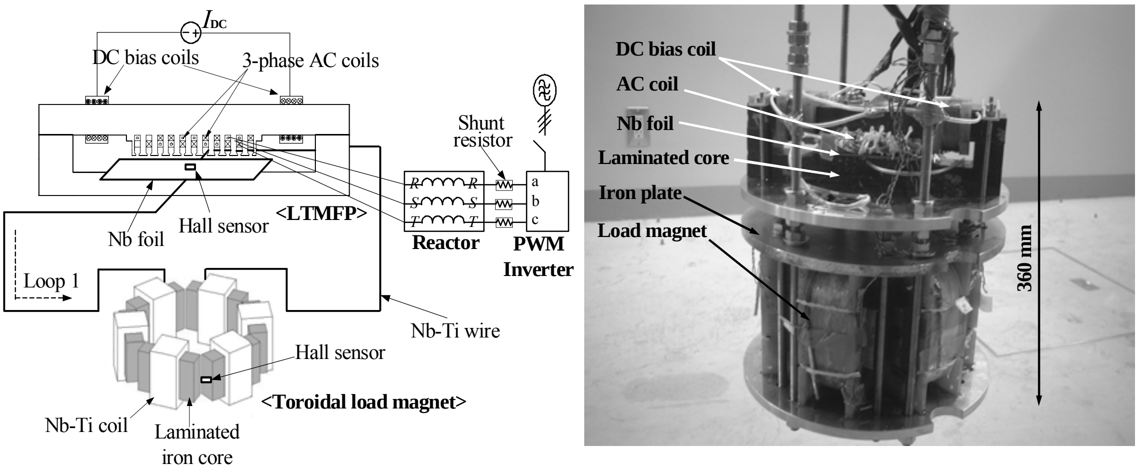

(a) connection diagram (b) assembly photograph

Fig. 5.4 Current pumping system with toroidal load magnet (the number of the element coils is 6).

Fig. 5.4 (a) provides the connection diagram of current pumping system with the toroidal load magnet (the number of the element coils is 6). The basic configuration is the same with the case of the small-scale load magnet. In order to reduce the distortion of the output current waveform, a 3-phase reactor is connected at the output of the 3-phase inverter. Two cryogenic Hall sensors (transverse type) are also installed. Fig. 5.4 (b) shows the photograph of the assembled current pumping system. As displayed in figure (b), an iron plate is installed in between the LTMFP and the toroidal load magnet in order to isolate the LTMFP from the flux leakage of the load magnet.

5.3 Experimental Sequences

5.3.1 Cooling procedure

In order to perform the experiment, the current pumping system is firstly cooled down to 4.2 K. The cooling procedure is as follows:

(1) The cryostat is filled with liquid nitrogen, and then the flux pump is pre-cooled close to 77 K.

(2) The liquid nitrogen in the cryostat is removed by pressurization with dry nitrogen gas. Then the cryostat is purged with helium gas.
(3) The liquid helium is transferred into the cryostat and cooled down to 4.2 K.

5.3.2 Test method

The pumping-up and down performances are tested with and without a load current. We select 10 A as a load current: This value shall be introduced in chapter 6. The following procedures are carried out.

(1) The DC bias current and AC current are applied, respectively to the DC bias coil and the 3-phase windings. Then pumping-up operation commences. The operation is performed until the pumped current reaches 10 A.
(2) After the pumped current reaches 10 A, the DC bias current and AC current are turned off. At this time, Loop 1 (see Fig. 5.4 (a)) is in a persistent current mode.
(3) 5 minutes later, the DC bias source and the 3-phase inverter are turned on at the same time. Afterwards, the pumping-up operation is started.
(4) 15 minutes later, the pumping-up operation is finished. The direction of the traveling magnetic field is reversed by means of the 3-phase inverter in order to facilitate the pumping-down operation. This operation is executed until the load current becomes zero.
(5) The driving frequency of the 3-phase inverter is changed.
(6) The cycles from step (1) to step (5) are repeated.

5.4 Test Results with the Small-Scale Load Magnet

In this section, the test for frequency dependency of pumping actions is carried out with the small-scale load magnet. As the value of the inductance of this magnet is low, the saturation behavior of the current pumping characteristic will be observable (see Fig. 2.15).

Further, experimental results are also explained based on the modified current pumping equation (2.30). The enhancement rate of the normal spot area *k* is estimated from the test results, and finally the validity of the analytical discussion (chapter 2) is confirmed.

5.4.1 Air-gap magnetic flux density

Fig. 5.5 shows the temporal variation of the air gap magnetic flux density, which is measured by the cryogenic hall sensor. As can be seen, a near homo-polar magnetic field can be realized. The positive and negative peak values are 180 and -10 mT for the DC bias current at 10 A and the AC current at 5.5 A_{peak}, 6 Hz (figure (a)), and 200 and -20 mT for DC bias current at 10 A and the AC current at 6 A_{peak}, 7 Hz (figure (b)), respectively. The measured results agree with the obtained ones by the 3-D FEM in chapter 3 (see Fig. 3.7). In order words, the test results with the use of the fabricated system can be discussed based on the simulation (chapter 3).

The normal spot area in the superconducting Nb foil is realized by the penetration of the magnetic flux density. Then, the magnetic flux density that is larger than $\mu_0 H_{c1}$ (horizontal line) is roughly considered to form the normal spots. The lower critical magnetic field $\mu_0 H_{c1}$ of the superconducting Nb foil is roughly 100 mT at 4.2 K [110]. The time durations of w_1, w_2, w_3, and w_4 are 66.1, 66.4, 65.3, and 67.4 ms, respectively. The average duration (w_a(6 Hz)) is 66.3 ms (see Fig. 5.5 (a)).

In the case of Fig. 5.5 (b), the time durations of w_1, w_2, w_3, w_4, and w_5 are 58.4, 61.9, 61.2, 61.2, and 61.9 ms, respectively. The average value (w_a (7 Hz)) is 60.9 ms. In addition, the periods of four poles of the traveling magnetic fields, which includes the

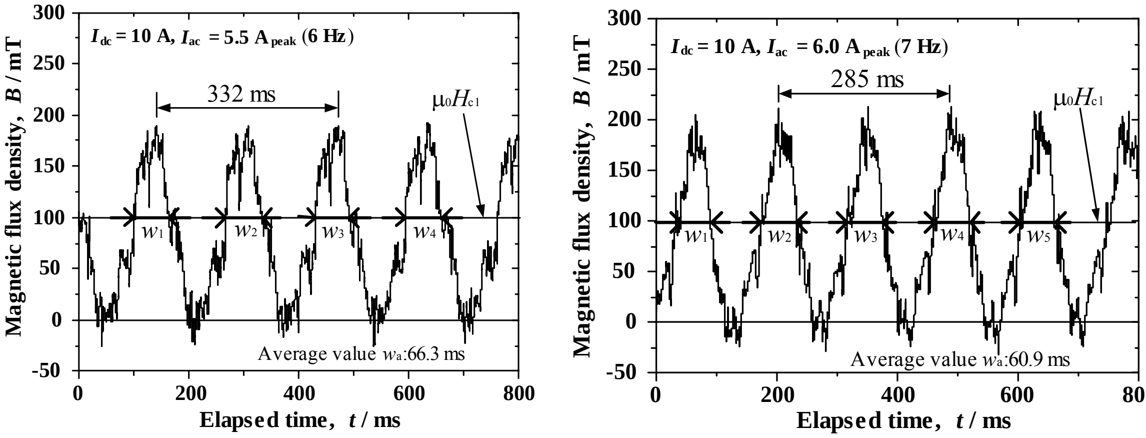

(a) DC bias current at 10 A and AC current at 5.5 A_{peak} (6 Hz)

(b) DC bias current at 10 A and AC current at 6 A_{peak} (7 Hz)

Fig. 5.5 Temporal variation of the magnetic flux density at the central part in the air gap. The measured temperature is 4.2 K.

superconducting properties of the Nb foil, are 332 and 285 ms, respectively (see Figs. 5.5 (a) and (b)). Referring to the FEM analysis for traveling waveform (see Fig. 3.3 (a)), the pole pitch of armature coil is 30 mm. Then, the length of full pitch (four poles) is 120 mm. From the ratio of these values and realized normal spot, the calculated width of normal spot (w_0) is expressed as follows:

In the case of Fig. 5.5 (a), $$w_0(6\text{Hz}) = \frac{120\ \text{mm}}{332\ \text{ms}} \times 66.3\ \text{ms} = 23.9\,\text{mm} \tag{5.1}$$

In the case of Fig. 5.5 (b), $$w_0(7\text{Hz}) = \frac{120\ \text{mm}}{285\ \text{ms}} \times 60.9\ \text{ms} = 25.6\,\text{mm} \tag{5.2}$$

As the teeth width of the LTMFP is 40 mm, the area of the normal spot S_0 on the superconducting Nb foil is expected as:

In the case of Fig. 5.5 (a), $S_0(6\ \text{Hz}) = 23.9\ \text{mm} \times 40\ \text{mm} = 956\ \text{mm}^2$ (5.3)

In the case of Fig. 5.5 (b), $S_0\ (7\ \text{Hz}) = 25.6\ \text{mm} \times 40\ \text{mm} = 1024\ \text{mm}^2$ (5.4)

The calculated size of the normal spot is referred in the next subsection in order to calculate the enhancement rate of the normal spot k.

5.4.2 Calculation sequences of current pumping

The measured results of the pumped current are estimated based on the modified analytical equation (2.30). Fig. 5.6 illustrates the flow chart of the current pumping. The detailed description is as follows:

Step 1

Referred to the experimental result of the temporal variation of the magnetic flux density (see Fig. 5.5), the initial width of the normal spot w_0 is estimated. Since the length of normal spot h is the same as the width of the teeth in the LTMFP (40 mm), the area of normal spot $S_0 = w_0 \times h$ can be estimated. From the estimated value S_0, the self-inductance l_0 and the resistance of the normal spot R_0 of the normal spot in the Nb foil are also estimated with the use of equation (2.26). Here the values w_0, S_0, R_0, and l_0 correspond to the condition that the enhancement rate of the normal spot size is zero, i.e., $k = 0$.

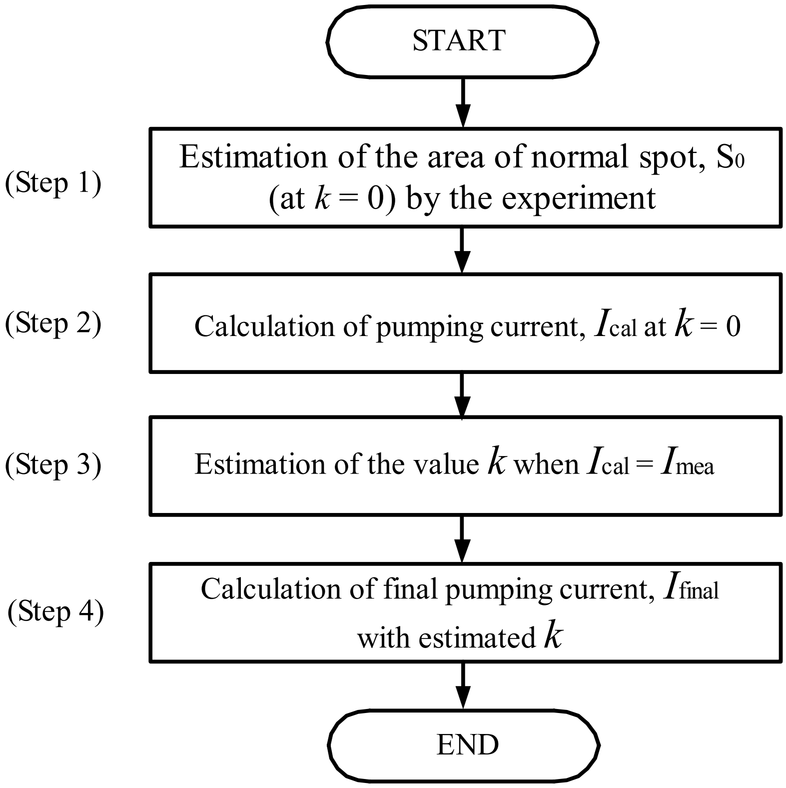

Fig. 5.6 Flow chart of calculation sequences for current pumping.

The normal spot size S_0 is obtained to be 956 mm^2 (equation (5.3)). In addition, the magnetic permeability of vacuum $\mu_0 = 4\pi\times10^{-7}$ H/m, resistivity of the normal spot $\rho = 1\times10^{-8}$ Ωm, thickness of the Nb foil $z = 20$ μm, and the gap length between the yoke and the Nb foil $d = 1.0$ mm (see configuration: Fig. 2.12) are already known.

Therefore, referring to the obtained parameters, the calculated values of the resistance and self-inductance of the Nb foil, R_0 and l_0 for two normal spots can be estimated with the following equations:

$R_0 = \rho h / zw_0 = (1\times10^{-8}\times40\times10^{-3}) / (20\times10^{-6}\times2\times23.9\times10^{-3}) = 0.418$ mΩ

$l_0 = \mu_0 S_0 / d = (4\pi\times10^{-7}) \times (23.9\times2\times40\times10^{-6}) / (1.0\times10^{-3}) = 2.4$ μH

Step 2

From the obtained parameters at step 1, the pumped current I_{cal} (at $k = 0$) is estimated using the modified analytical equation (2.30)

In this case, $w_n = w_0$, $R_n = R_0$, and $l_n = l_0$. From these parameters, the value of the pumped current $I_{cal}(t)$ (at $k = 0$) is calculated.

Step 3

In order to find the appropriate value of k, the calculated pumping value I_{cal} (step 2) is compared with the measured pumping current I_{mea}. From the comparison, the value k is estimated.

Step 4

Based on the estimated value k at step 3, the parameter values at the driving frequency f such as $w_{\mathrm{n}}(f)$ and $R_{\mathrm{n}}(f)$ are also estimated. Consequently, using the modified equation (2.30) and the estimated value k, the final value of pumped current I_{final} at the driving frequency f is calculated.

5.4.3 Experiment and calculation results for current pumping

In this subsection, in order to observe the current pumping characteristics of the LTMFP, the experiments are carried out after the LTMFP and the small-scale load magnet (see Fig. 5.3) are immersed in liquid helium (4.2 K). Through the experiment, the relation between the value of the pumped current and the amplitude of the magnetic flux density is investigated. In addition, the pumping action according to the driving frequency is observed. Moreover, using the calculation sequences described in subsection 5.4.2, the enhancement rate of the normal spot size k is estimated.

Further, since appropriate values of the DC bias current and the AC current have already been obtained by the 3-D FEM simulation in chapter 3, these values are confirmed by the experimental investigations.

Fig. 5.7 shows the measured and calculated results of the pumped current with DC bias current at 10 A and AC current at 5.5 $\mathrm{A_{peak}}$ for different frequencies, i.e., 6, 8, 20 Hz. The experiments are performed for 400 s. The amplitude of the traveling magnetic field at the air gap is shown in Fig. 5.5 (a). It can be seen that the pumped currents saturate around t= 100 s because of the smaller inductance value of the load magnet. The saturation value of the pumped currents is in proportion to the driving frequency. This operating characteristic has been already predicted in the subsection 2.3.4 (see Fig. 2.17). The measured results of the saturated currents at 6, 8, and 20 Hz are 19.8, 22.3, and 28.4 A, respectively.

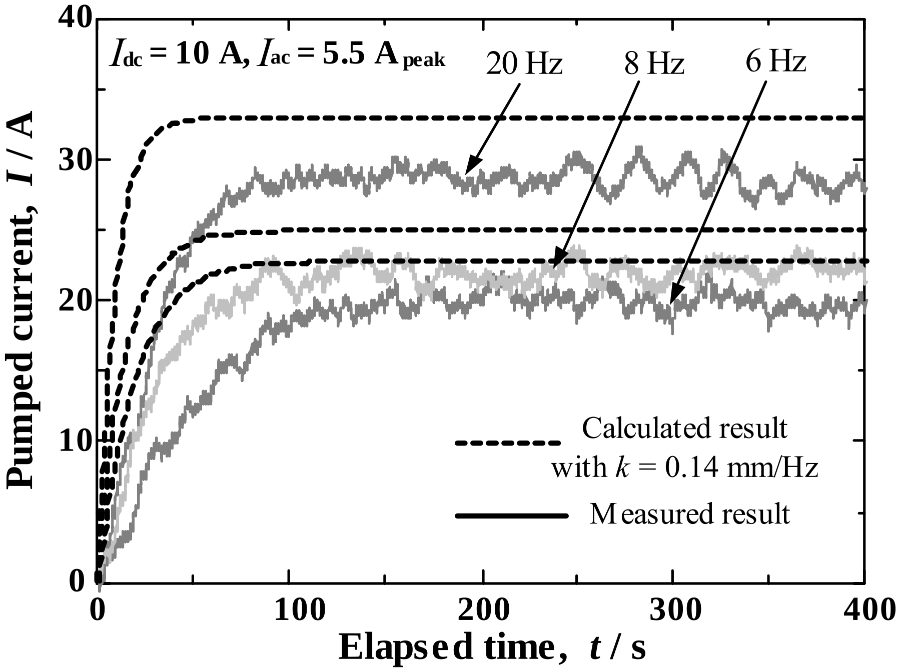

Fig. 5.7 Measured and calculated results of the pumped current with DC bias current at 10 A and AC current at 5.5 A_{peak}. The measured temperature is 4.2 K.

The reason for the noise of the pumped current is that of the air-gap magnetic flux density, i.e., from the inverter (see Fig. 5.5 (a)).

Furthermore, from the calculation sequence in subsection 5.4.2, the enhancement rate of the normal spot is estimated to be k = 0.14 mm/Hz. The calculated saturation currents with k = 0.14 mm/Hz at 6, 8, and 20 Hz become 22.5, 25.1, and 33.5 A, respectively. As can be seen by comparison between solid curves and broken curves in Fig. 5.7, these calculated values agree well with the measured ones.

Moreover, in order to verify the estimated value of k for different operational condition, the experiment is also performed under the different amplitude of the magnetic flux density.

Fig. 5.8 shows measured and calculated results of the pumped current with the DC bias current at 10 A and AC current at 6 A_{peak} for 7, 9, and 15 Hz. The amplitude of the traveling magnetic field at the air gap is shown in Fig. 5.5 (b). Under these driving frequencies, the measured results of the pumped saturation current are 22.7, 25.3, and 29.8 A, respectively.

From the calculation sequence of Fig. 5.6, the corresponding calculated values of the pumped current at 7, 9, and 15 Hz are 26.9, 28.8, and 35.9 A, respectively. As can be

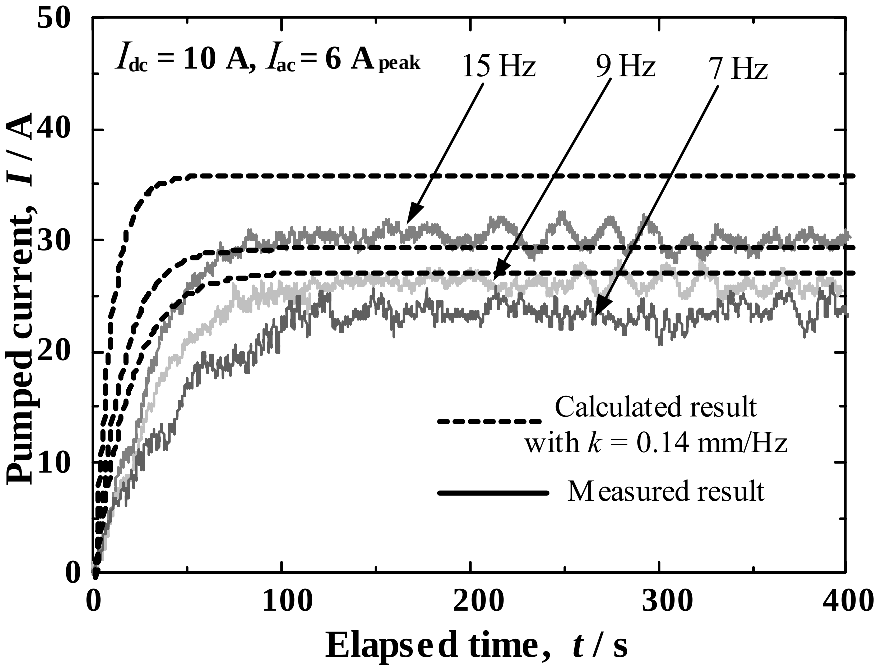

Fig. 5.8 Measured and calculated results of the pumped current with DC bias current at 10 A and AC current at 6 A_{peak}. The measured temperature is 4.2 K.

Table 5.1 Results of the pumped current with a small-scale load magnet (1.3 mH).

L (mH)	**I_{DC} (A)**	**I_{AC} (A_{peak})**	**f (Hz)**	Measured and calculated results of pumped current during 400 seconds (A) (measurement / theory)
1.3	10	5.5	6	19.8 / 22.5
			8	22.3 / 25.1
			20	28.4 / 33.5
		6	7	22.7 / 26.9
			9	25.3 / 28.8
			15	29.8 / 35.9

seen, even under the different amplitude of the magnetic field, the measured pumped currents agree well with the calculated values with the use of k = 0.14 mm/Hz (see Fig. 5.8).

Based on the measured results of the pumped current in Figs. 5.7 and 5.8, it has been checked that the saturated value of the pumped current is also roughly proportioned to the amplitude of the magnetic flux density. Thus, it has been confirmed that the pumped current depends not only on the amplitude of the magnetic flux density, but also on the driving frequency as shown in Table 5.1.

Based on this study, it has been concluded that pumping characteristics of the LTMFP can be effectively explained by means of the phenomenon of the enhancement of the normal spot in the moving flux.

5.5 Test Results with the Toroidal Load Magnet

In this section, in order to examine the operating relation between the inductance of the load magnet and the current pumping characteristics (see Fig. 2.15), the LTMFP is operated with the toroidal load magnet at 543 mH. In addition, in order to investigate the pumping action in detail, the LTMFP system is executed under various frequencies.

Further, for the verification of the already calculated enhancement rate of the normal spot k = 0.14 mm/Hz, calculated currents are compared with measured ones below 20 Hz. Moreover, the enhancement rate over 20 Hz is also estimated using the calculation sequence in subsection 5.4.2.

As the experimental condition of this section is the same with that in section 5.4, the operating characteristics of the toroidal magnet are compared with those of the small-scale load magnet.

5.5.1 Air-gap magnetic flux density

Fig. 5.9 shows the measured results of the current waveform of the 3-phase inverter at 6 A_{peak} (7 Hz) without and with a reactor, respectively. These waveforms are measured by use of the shunt resistors (50 mΩ) at room temperature. As can be seen in the figures, utilization of the reactor surely reduces the distortion of the waveforms.

Fig. 5.10 shows the measured results of temporal variation of magnetic flux density at the central air gap with DC bias current at 10 A and AC current at 5.5 A_{peak} (7 Hz), and with DC bias current at 10 A and AC current at 6 A_{peak} (7 Hz), respectively. The corresponding positive and negative peak values are 180 and -10 mT, and 200 and

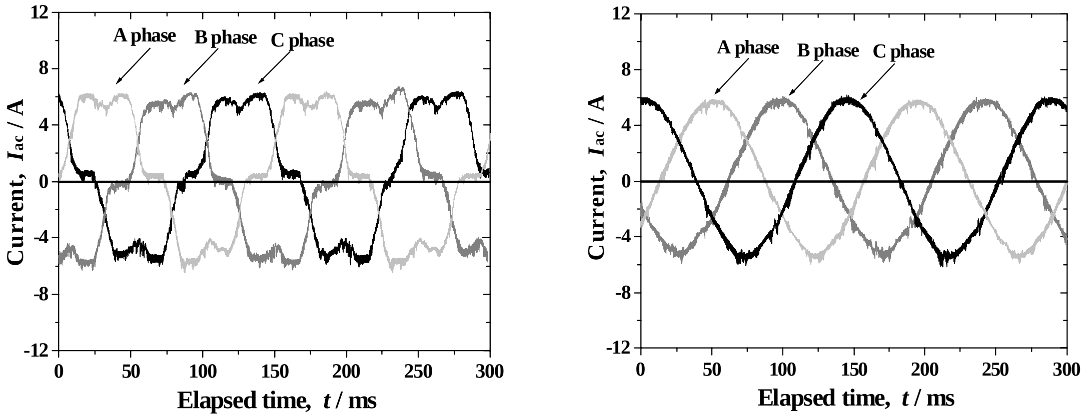

(a) without reactor (b) with reactor

Fig. 5.9 Current waveforms of the 3-phase inverter at 6 A_{peak} (7 Hz) at room temperature.

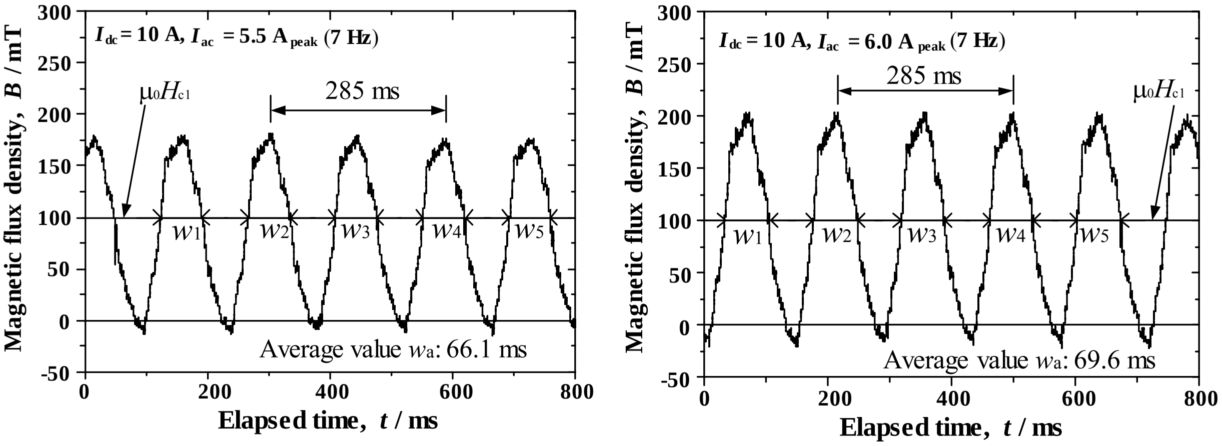

(a) DC bias current at 10 A and AC current at 5.5 A_{peak} (7 Hz) (b) DC bias current at 10 A and AC current at 6 A_{peak} (7 Hz)

Fig. 5.10 Temporal variations of the magnetic flux density at the central part in the air gap with 3-phase reactor. The driving frequency is 7 Hz and the measured temperature is 4.2 K.

-20 mT, respectively. As can be seen with figures, the current waveform with reactor can produce comparatively clear traveling magnetic field with the air gap. This can also be understood by comparing Fig. 5.10 with Fig. 5.5.

In Fig. 5.10, we can also estimate the width of the normal spots with the criterion of $B=\mu_0 H_{c1}$ (=100 mT). In the case of Fig. 5.10 (a), the time durations from w_1 to w_5 are 65.3, 67.3, 66.0, 65.3, and 66.7 ms, respectively. In the case of Fig. 5.10 (b), the time durations from w_1 to w_5 are 68.8, 71.4, 70.2, 68.2, and 69.5 ms, respectively. These average values are 66.1 and 69.6 ms, respectively. Based on the calculation sequence of subsection 5.4.2, the initial width of normal spot area w_0 is estimated as follows: (the distance of full pitch (4 poles) is 120 mm.)

In the case of Fig. 5.10 (a), $$w_0 = \frac{120\ \text{mm}}{285\ \text{ms}} \times 66.1\ \text{ms} = 27.8\,\text{mm} \tag{5.6}$$

In the case of Fig. 5.10 (b), $$w_0 = \frac{120\ \text{mm}}{285\ \text{ms}} \times 69.6\ \text{ms} = 29.3\,\text{mm} \tag{5.7}$$

In addition, the width of the teeth in the LTMFP is 40 mm. Thus, the estimated values S_0 on the superconducting Nb foil are expected as follows:

In the case of Fig. 5.10 (a), $S_0 = 27.8\text{ mm} \times 40\text{ mm} = 1112\text{ mm}^2$ (5.8)

In the case of Fig. 5.10 (b), $S_0 = 29.3\text{ mm} \times 40\text{ mm} = 1172\text{ mm}^2$ (5.9)

Compared with the estimated values w_0 in Fig. 5.5, these values are slightly higher due to the reduction of noise. Other parameters, i.e., l_0 and R_0, are also estimated by the calculation sequence of subsection 5.4.2.

5.5.2 Experiment and calculation results for current pumping characteristics

The experiment is carried out with a toroidal load magnet (543 mH) after both the LTMFP and the toroidal load magnet are immersed in liquid helium (4.2 K).

Fig. 5.11 shows the measured and calculated results of the pumped current with DC bias current at 10 A and AC current at 5.5 A_{peak}. The operating conditions are from 7 to 20 Hz for the duration of 18 minutes. Under these driving conditions, the measured values of the pumped current at 7, 8, 9, 10, 15, and 20 Hz reach 2.8, 3.2, 3.8, 4.4, 6.1, and 8.9 A, respectively. Compared with pumping results in the small-scale load magnet (see Figs. 5.7 and 5.8), the noise is drastically reduced due to the clear waveform of the magnetic flux density in the air gap.

Since the inductance of the toroidal load magnet is larger than that of the small-scale load magnet, the LTMFP generates the stabilized current pumping without saturation. Moreover, it has been observed that the pumped current also shows the frequency dependency.

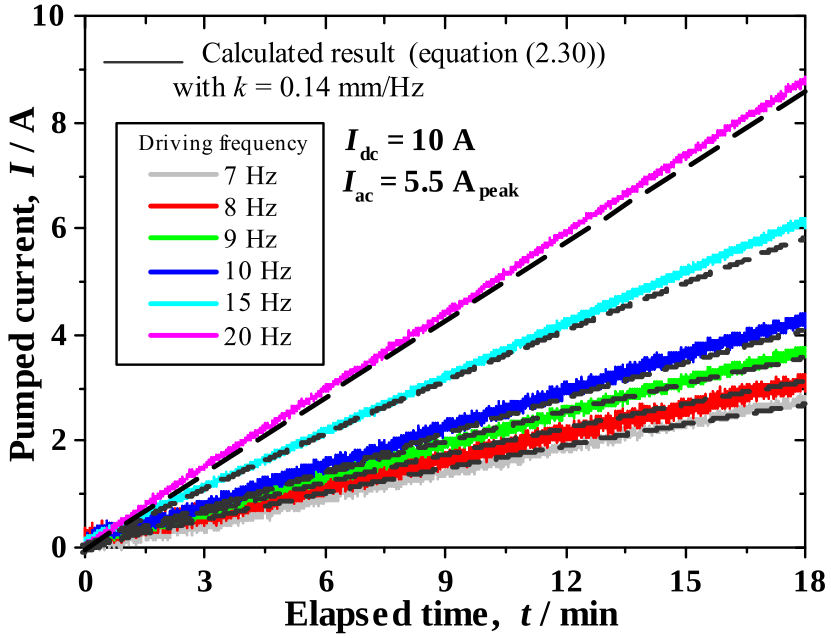

Fig. 5.11 Measured and calculated results of the pumped current with DC bias current at 10 A and AC current at 5.5 A_{peak}. The measured temperature is 4.2 K.

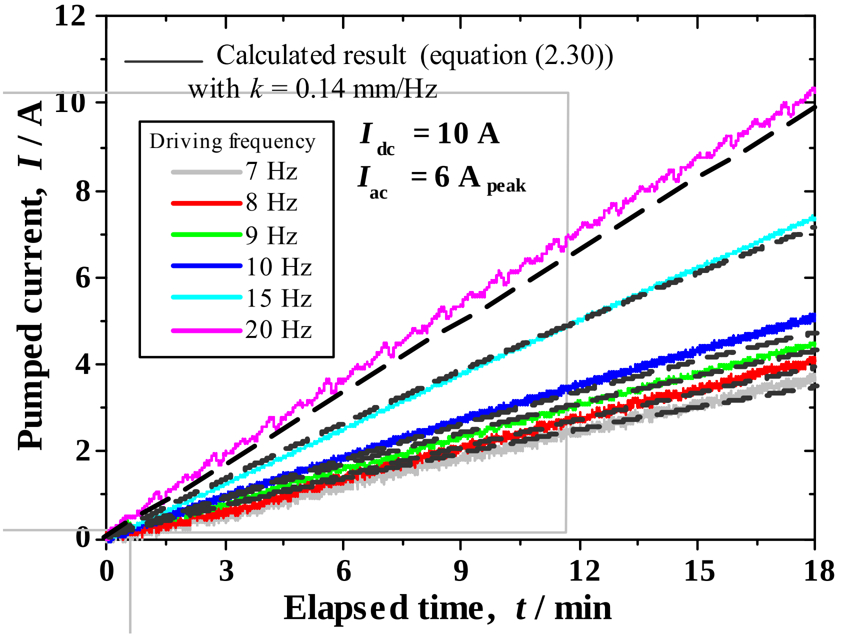

Fig. 5.12 Measured and calculated results of the pumped current with DC bias current at 10 A and AC current at 6 A_{peak}. The measured temperature is 4.2 K.

Based on the calculation sequence of Fig. 5.6 and k = 0.14 mm/Hz, the theoretical curves are shown as broken curves in Fig. 5.11. As can be clearly seen, the agreement between the calculated results and the measured results is excellent. For example, the calculated results of the pumped current at 7, 8, 9, 10, 15, and 20 Hz become 2.7, 3.1, 3.6, 4.2, 5.9, and 8.7 A, respectively when t=18 min.

Fig. 5.12 also shows the measured and calculated results of the pumped current with DC bias current at 10 A and AC current at 6 A_{peak} in the duration of 18 minutes. Under these driving conditions, the measured results at 7, 8, 9, 10, 15, and 20 Hz become 3.6, 4.1, 4.4, 5.0, 7.3, and 10.2 A, respectively. From calculation sequences of Fig. 5.6, on the other hand, the calculated results at 7, 8, 9, 10, 15, and 20 Hz are 3.4, 3.9, 4.3, 4.7, 7.0, and 9.9 A, respectively. That is, the calculated results of the pumped current with k = 0.14 mm/Hz nearly coincided with the measured ones (see Fig. 5.12). This means that the validity of the obtained enhancing rate of the normal spot (k = 0.14 mm/Hz) is

Table 5.2 Measured and calculated values of the pumped current with toroidal load magnet of 543 mH under the duration of 18 minutes.

L **(mH)**	**I_{DC}** **(A)**	**I_{AC}** **(A_{peak})**	**f** **(Hz)**	Measured and calculated currents (A) after 18 minutes (measurement / theory)
543	10	5.5	7	2.8 / 2.7
			8	3.2 / 3.1
			9	3.8 / 3.6
			10	4.4 / 4.2
			15	6.1 / 5.9
			20	8.9 / 8.7
		6	7	3.6 / 3.4
			8	4.1 / 3.9
			9	4.4 / 4.3
			10	5.0 / 4.7
			15	7.3 / 7.0
			20	10.2 / 9.9

confirmed. In addition, from the experimental results of Figs. 5.11 and 5.12, it can be seen that the pumped currents depend on the amplitude of the magnetic flux density.

The total results for pumping currents with toroidal load magnet of 543 mH under the duration of 18 minutes are shown in Table 5.2. Namely, the performance of the LTMFP is dominated by the driving frequency, the amplitude of air gap magnetic field, and the inductance of the load magnet. With respect to the driving frequency, more detailed discussion is done in the following.

In order to optimize driving frequency of the LTMFP, the pumping current rate C_{pr} is estimated based upon the analytical expression (equation (2.30)) and the experiment. The driving frequency is varied from 7 to 60 Hz by means of PWM inverter. The solid circles in Fig. 5.13 show the measured results of the pumping current rate for different driving frequencies. The operating currents are DC bias current at 10 A and AC current at 6 A_{peak}. The pumping current rate is estimated for the time duration of 100 s. Table 5.3 lists the estimated values. The solid and dotted curves are the theoretical expression (equation (2.30)) for the driving frequency, respectively, under and over 20 Hz. And the corresponding enhancement rates k are 0.14 and 0.63 mm/Hz. The conventional curve with k=0 is also plotted for comparison. As can be clearly seen, the theoretical curves with finite k agree well with the measured results.

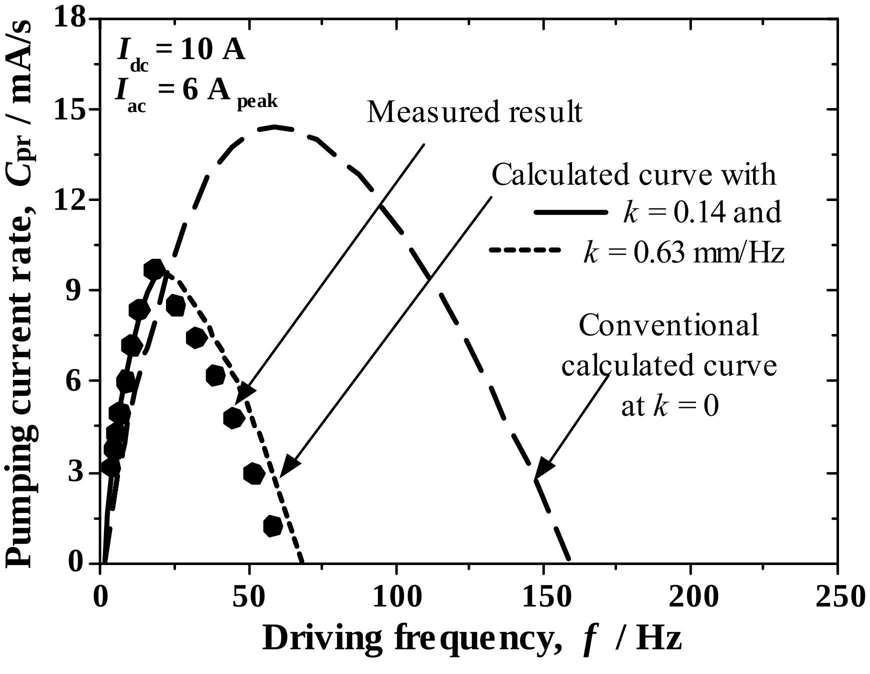

Fig. 5.13 Measured current pumping rate C_{pr}, calculated ones with k = 0.14 and 0.63 mm/Hz, and calculated one with k = 0, respectively.

Table 5.3 Pumped current rates with DC bias current at 10 A and AC current at 6 A_{peak} under a toroidal load magnet of 543 mH.

L (mH)	I_{dc} (A)	I_{ac} (A_{peak})	f (Hz)	C_{pr} (mA/s)
543	10	6	7	3.4
			8	3.9
			9	4.2
			10	4.7
			12.5	5.8
			15	6.9
			17.5	8.3
			20	9.5
			25	8.4
			30	7.5
			35	6.2
			40	4.7
			50	2.8
			60	1.2

As shown in Fig. 5.13, the measured value of the pumped current rate reaches the maximum value at 20 Hz. And then, such rate decreases over 20 Hz. This means that the optimal driving frequency is around 20 Hz. The main reason for this pumping behavior is due to the magnetic diffusion in the superconducting Nb foil. That is, as is already discussed in subsection 3.3.2, the characteristic time of the magnetic diffusion in the superconducting Nb foil is around 20 Hz. This means that the enhancement rate of the normal spot is enlarged over 20 Hz. And then the corresponding C_{pr} is decreased.

Further, it is expected that the pumping rate reaches zero at around 70.5 Hz. When the driving frequency is over 70.5 Hz, the pumping action cannot produce pumping current any more. This frequency is called the “upper limit driving frequency”. The characteristic time of the magnetic diffusion t_{md} corresponding to the maximum frequency at 20 Hz is 50 ms (=1/20 Hz). This result agrees with the calculated value

($46\ \text{ms} = \dfrac{1}{21.7\ \text{Hz}}$) (see equation (3.22)). In addition, the tendency of magnetic diffusion according to the driving frequency coincides comparatively with the results of the 3-D FEM simulation (see Fig. 3.11). On the other hand, the theoretical equation with k = 0, which doesn’t take into account the phenomenon of magnetic diffusion, cannot explain the operating characteristics of the pumping performance over 20 Hz.

Consequently, it has been verified that pumping characteristics of LTMFP are effectively explained by the phenomenon of enhancement of the normal spot area.

5.6 Performance Test of LTMFP with the Use of Toroidal Load Magnet

In this section, in order to apply the LTMFP to the current compensator in chapter 6, the basic tests for charging-up and down performances are executed. The tests are carried out at 10, 15, and 20 Hz. The experimental setup and the operation conditions of DC bias current and AC current are the same as in subsection 5.5.2. As an evaluation test for current compensator, the pumping-up and down actions are executed in a persistent current mode at 10 A.

5.6.1 Pumping-up and down performances

The experiment is carried out after the LTMFP and the toroidal load magnet are immersed in liquid helium (4.2 K). Experimental sequences are executed as outlined in subsection 5.3.2.

Fig. 5.14 shows the measured results of the pumping-up and down operations with an operating load current at 10 A. The current conditions are DC bias current at 10 A and AC current at 6 A_{peak}. As is already mentioned, the pumping-up and down rates are proportional to the driving frequency. The measured rates of the current pumping-up and down performance are shown in Table 5.4. Compared to the pumping-down rate, it has been observed that the pumping-up rate is smaller. The reason is as follows.

The connected circuit for this test is mainly composed of resistor and inductor elements. The resistor and inductor elements mean the contact resistance and the inductance of the toroidal load magnet, respectively. Here, the contact resistance is small and can be ignored. In general, the inductor is capable of storing magnetic energy. The energy will be stored and released in the inductor if the circuit is connected with the positive and negative charging devices. Particularly, the charging duration depends on the initial current conditions.

In the case of the pumping-up operation with the initial operating current, the pumping-up rate is slower due to the already stored finite energy by the initial current. If the initial operating current is larger, more time is required to charge up the pumping current. On the other hand, in the case of the pumping-down action, the decay time is fast due to reverse pumping current. From these reasons, the slopes of pumping current show different rates according to the pumping-up and down actions as shown in Fig. 5.14.

Consequently, through the experimental performance of pumping-up and down actions in the operating current (persistent current mode), the control of pumping current according to driving frequency is demonstrated.

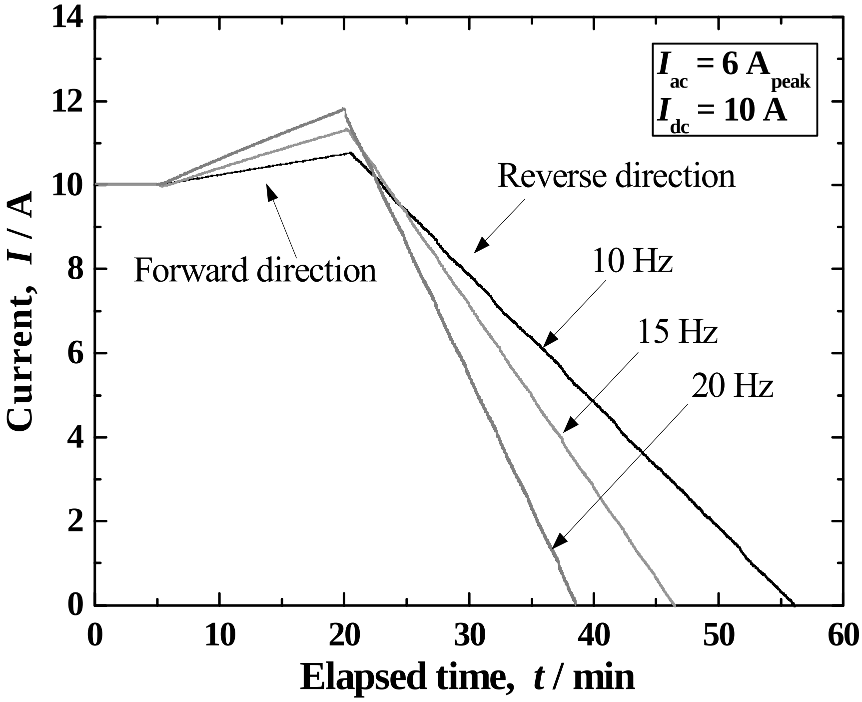

Fig. 5.14 Pumping-up and down operations with the operating load current at 10 A. The current conditions are DC bias current at 10 A and AC current at 6 A_{peak} (driving frequency: 10, 15, and 20 Hz). The measured temperature is 4.2 K.

Table 5.4 Pumped current rates of the pumping-up and down performances with the operating load current at 10 A.

L (mH)	I_{DC} (A)	I_{AC} (A_{peak})	I_{op} (A_{dc})	f (Hz)	I_{rate} (mA/s) (up / down)
543	10	6	10	10	0.83 / -5.1
				15	1.47 / -6.9
				20	1.98 / -10.8

5.7 Summary

In this chapter the fundamental characteristics of the LTMFP were investigated. The experimental results of the current pumping characteristics were explained based on the theoretical equation presented in chapter 2. The conclusions are summarized as follows:

(1) Already obtained values of DC bias current and AC current based on 3-D FEM simulation for the operation of the LTMFP in chapter 3 have been confirmed by experiments.

(2) From the investigation of the current pumping with the small-scale load magnet (1.3 mH), it has been observed that the pumped current depends not only on the amplitude of the magnetic flux density, but also on the driving frequency. These operating characteristics for the current pumping could be confirmed by the modified equation (2.30). The enhancing rate of the normal spot, $k = 0.14$ mm/Hz was estimated based on the experiment.

(3) From various experiment results with the toroidal load magnet (543 mH), the performance of the LTMFP with large inductance load was investigated for different amplitude of the magnetic field and the driving frequency. In addition, the obtained value $k = 0.14$ mm/Hz has also been verified from the pumping observations according to the driving frequency.

(4) From the pumping operations in a wide range of the driving frequency, it was found that the pumping current rate is maximized at around 20 Hz. The corresponding characteristic time of magnetic diffusion t_{md} is estimated as 50

ms ($=\frac{1}{20\ \text{Hz}}$). This measured value agrees with the numerically simulated result in Fig. 3.11. The main reason for the decrement of the pumping current rate over 20 Hz is the enhancement of the penetrated area due to the effect of the magnetic diffusion.

(5) When the driving frequency was over 20 Hz, the enhancement rate of the normal spot k was enlarged to be 0.63 mm/Hz. This calculated rate was close to the simulated ones carried out through FEM analysis (see Fig. 3.11). As a result, pumping actions for frequency dependency in LTMFP could be explained by the phenomenon of the enhancement of the normal spot in the moving flux in chapter 2.

(6) As a basic demonstration for the current compensator, it has been observed that the charging-up and down actions of the LTMFP have stably been carried out under the operating load current at 10 A. From these observations, it has been deduced that the fabricated LTMFP can be applied to the current compensator for superconducting magnet systems in a persistent current mode.

Finally, from various experimental characteristics and the analytical equations, basic observations for pumping actions in the proposed LTMFP have been performed. In particular, the explanation of the pumping tendency according to the enhancement of normal spot area has been firstly introduced in the study.

Furthermore, based on these observations for pumping-up and down actions in the persistent current mode, the possibility of the LTMFP has been demonstrated as an energy-saving current supply in the persistent current loop.

Chapter 6 Performance of Current Compensator by Use of the LTMFP

6.1 Introduction

For the applications of superconducting magnet systems, e.g., Maglev train and NMR, in order to obtain a high magnetic field with stabilized property, the technology of maintenance of the persistent current mode has currently been recognized to be one of the most important problems.

As a solution to persistent current decay, this chapter is devoted to achieve a current compensator for the superconducting magnet. The new type of current compensator is composed of the LTMFP and a typical feedback control circuit.

The superconducting toroidal magnet is subjected as a practical load. The current compensation performance is experimentally investigated and discussed in this chapter.

6.2 Basic Principle of the Current Compensator

Fig. 6.1 shows the schematic illustration of the current compensation by the use of the LTMFP. Since the superconducting load magnet has some joints, small contact

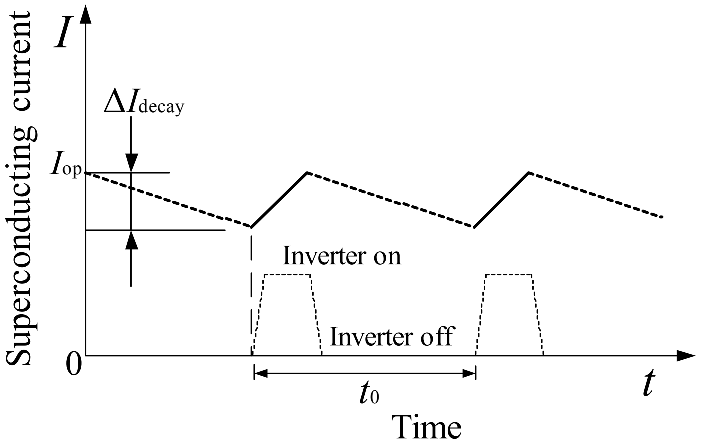

Fig. 6.1 Schematic illustration of current compensation by the inverter operation.

resistances exist. These resistances cause the persistent current decay $\Delta I_{\mathrm{decay}}$ in the closed superconducting current loop. Then, the LTMFP is excited by means of the inverter. In this figure, the current is recovered to be I_{op}, i.e., initial operating current. As can be easily understood, the time interval for compensation t_0 has to be decreased if we want to decrease $\Delta I_{\mathrm{decay}}$.

6.3 Experimental Setup

Fig. 6.2 shows the photograph of the experimental system. The feedback control circuit is installed at room temperature.

Fig. 6.3 shows the connection diagram of the current compensator system. In this experiment, the toroidal magnet that is made of Nb-Ti wire is utilized as a load magnet. In order to realize the persistent current mode of the superconducting magnet, a thermal type (heater driven) PCS is installed in parallel with the DC current source I_{DC1}.

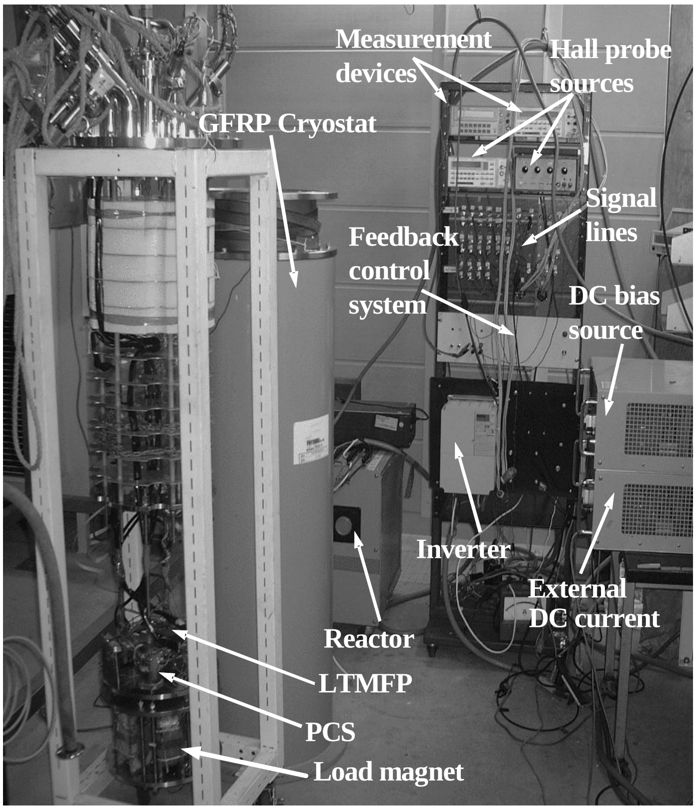

Fig. 6.2 Photograph of the assembled experimental system with LTMFP.

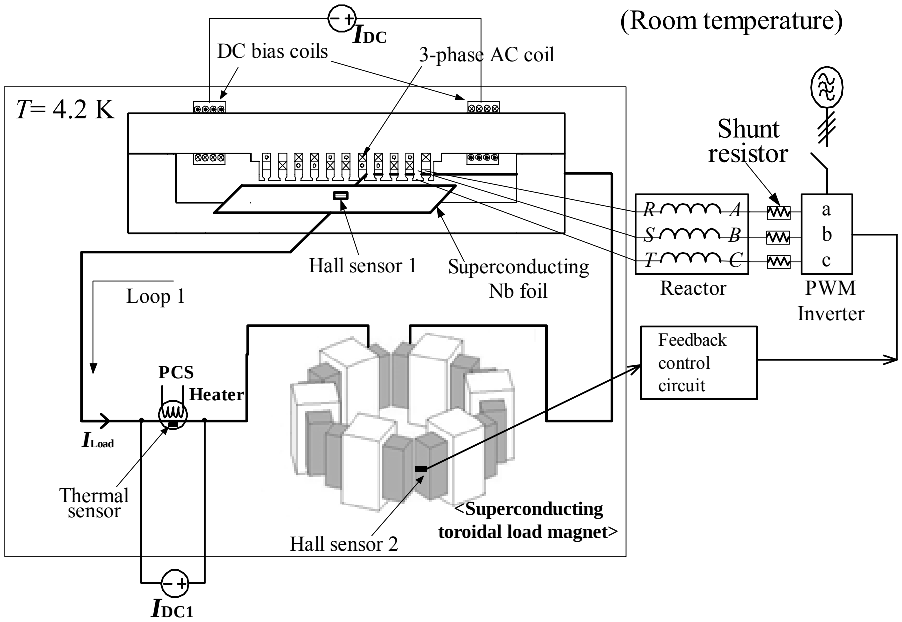

Fig. 6.3 Connection diagram of the current compensator system.

The superconducting Nb foil, a PCS, and a superconducting load magnet are connected by means of the superconducting Nb-Ti wire. This means that the superconducting loop can be formed except for the contact parts. The air-gap magnetic flux density of the LTMFP is measured by Hall sensor 1. Hall sensor 2 is also installed in between the element coils of the load magnet for the measurement of the load current. The output current of the inverter is measured using shunt resistors (50 mΩ). The experiments are carried out after the LTMFP and the toroidal load magnet are immersed in liquid helium (4.2 K).

6.4 Persistent Current Operation Method for Superconducting Load Magnet by Use of LTMFP

In this section, the explanations for the control sequence of the current compensator and the feedback control circuit are described.

Fig. 6.4 provides the flow chart of the operation of superconducting load magnet. The control sequences are as follows:

(Step 6.2.1) the external DC current (I_{DC1}, see Fig. 6.3) supplies the operating current

I_{op} to the superconducting load magnet during PCS is turned off.

(Step 6.2.2) PCS is turned on and I_{DC1} is turned off; the superconducting load magnet keeps the superconducting persistent mode. Then, the persistent current decay is caused.

(Step 6.2.3) the current compensation is carried out in order to compensate the persistent current decay by the use of the feedback control circuit. Operating sequence of the feedback control circuit is explained in Fig. 6.5 in more detail.

(Step 6.2.4) when the compensating current reaches the target value, the compensator is paused. Through these procedures, the superconducting load magnet is excited.

Fig. 6.5 provides the flow chart of the current compensation operation with feedback control circuit. The control procedures are as follows:

(Step 6.3.1) the DC bias source supplies current to DC bias coil of the LTMFP.

(Step 6.3.2) the inverter supplies to AC coil of the LTMFP. Then, the LTMFP generates pumping current I_{load}.

(Step 6.3.3) the feedback control circuit of the current compensator detects I_{load}.

(Step 6.3.4) until the I_{load} reaches operating current I_{op}, the LTMFP generates I_{load}.

(Step 6.3.5) if I_{load} reaches I_{op}, the current compensator turns off the inverter. The closed superconducting magnet keeps persistent current mode. Then the persistent current decay I_{decay} is caused.

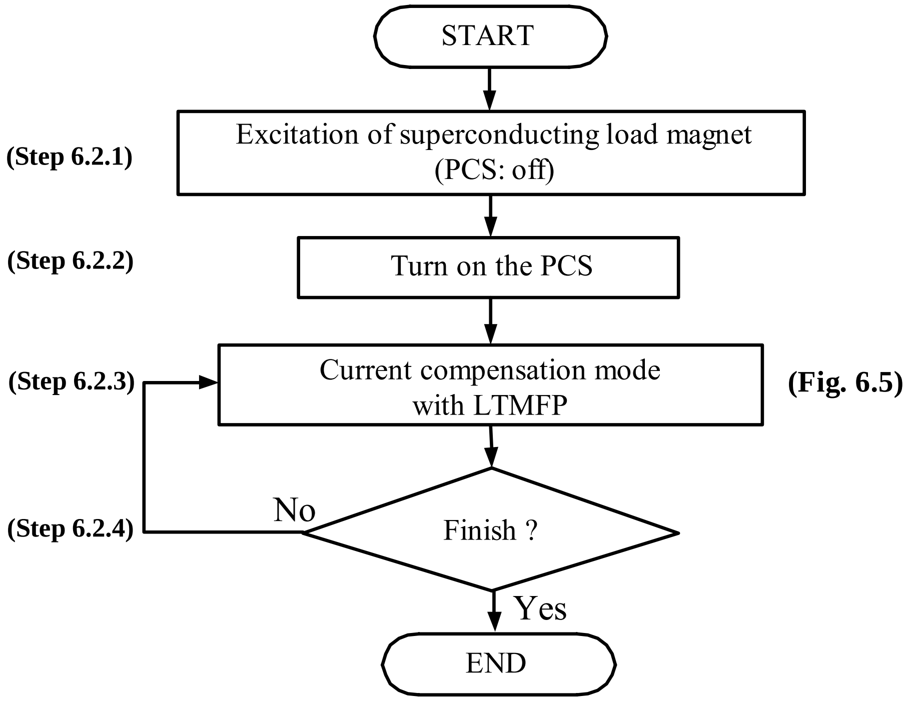

Fig. 6.4 Flow chart of the persistent current operation of superconducting load magnet.

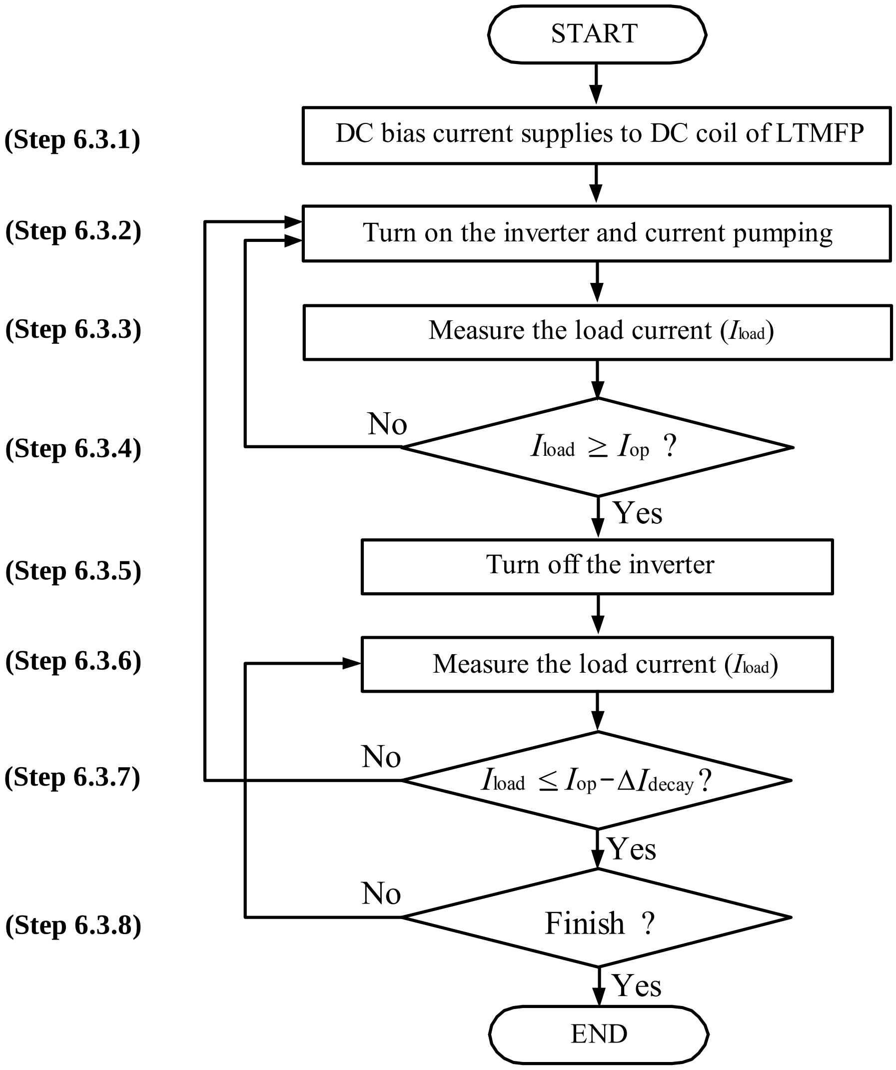

Fig. 6.5 Flow chart of operation of the current compensation.

(Step 6.3.6) the current compensator detects I_{load} by use of the feedback control circuit.

(Step 6.3.7) if I_{load} is smaller than I_{op} - ΔI_{decay} (the criterion of ΔI_{decay}, 1 mA is set in this current compensator), the inverter is turned off. However, if I_{load} exceeds I_{op} - ΔI_{decay} (that means ΔI_{decay} is larger than 1 mA), the feedback control circuit turns on the inverter of the LTMFP.

(Step 6.3.8) the procedures of (step 6.3.6) and (step 6.3.7) are repeated.

Through these procedures, the feedback control circuit compensates the decayed current ΔI_{decay}.

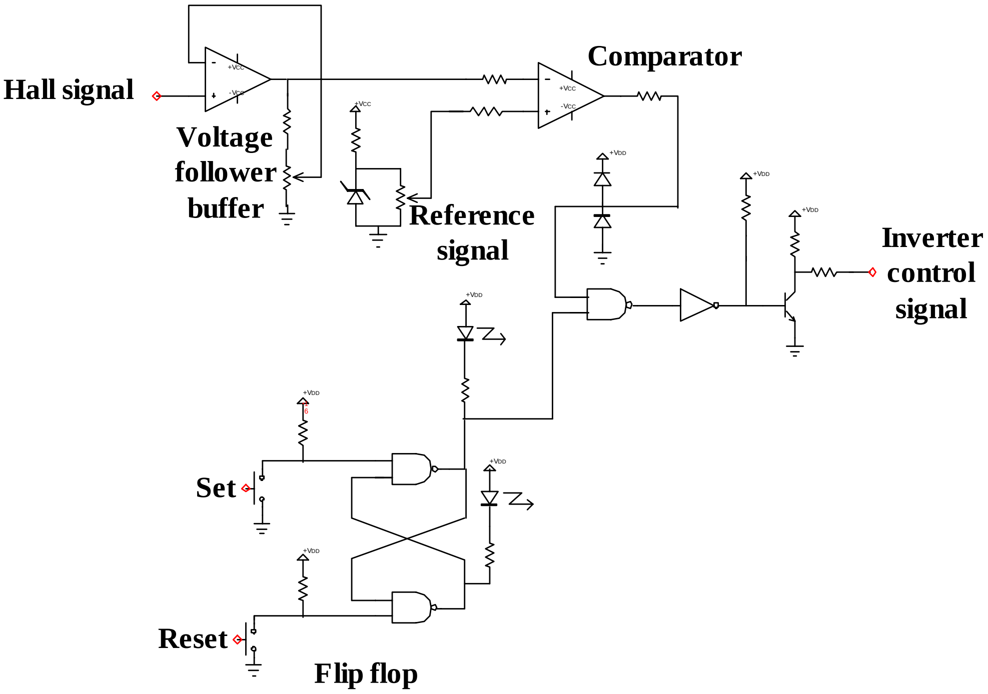

Fig. 6.6 Circuit diagram of the feedback control circuit.

Fig. 6.6 shows the circuit diagram of the feedback control circuit. A non-inverting amplifier circuit amplifies the Hall signal, which corresponds to the load current of the superconducting magnet. This device is called the voltage follower. The amplified voltage is used to adjust the analog level for the reference voltage that is arranged by the variable resistor. In the feedback control circuit, the target value of the compensation current is determined by the reference signal. A compensation operation is carried out when the decremented value of the current $\Delta I_{\mathrm{decay}}$ exceeds 1 mA. Resistors and diodes clamp the output signal of the comparator. In addition, the RS flip-flop can generate an “open” or “close” signal. This is the basic function of the feedback control circuit.

6.5 Operating Characteristics of the PCS

In this section, the operating characteristics of the thermal type PCS are examined. Since the thermal process dominates the switching mechanism for this type of PCS, the response time of the LTMFP is determined by that of the PCS.

Fig. 6.7 shows the structure of thermal type PCS and the position of the thermometer.

After the outer Nb-Ti coil is wound, the thermometer is attached to the surface of the PCS by using cryogenic silicone grease. Epoxy resin is then used to cover the Nb-Ti coil and thermometer.

Fig. 6.8 shows the measured result of the temperature trace at the surface of the PCS by heating power at 3.21 W (100 mA). This measurement is performed under the operating current at 10 A as a practical situation. The heater is turned on for 20 s (from 3 to 23 s).

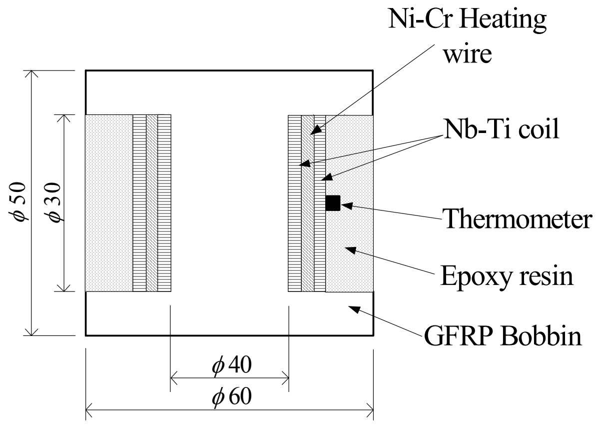

Fig. 6.7 Structure of the thermal type PCS and position of thermometer.

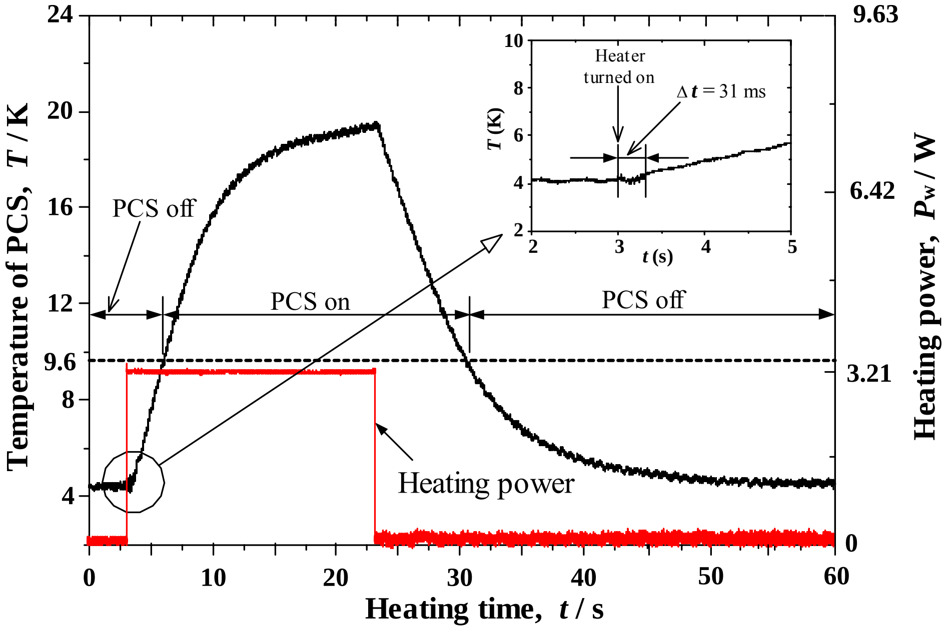

Fig. 6.8 Measured results of the temperature trace of the PCS with heating power at 3.21 W and heating time of 20 seconds. The initial temperature is 4.2 K and the operating current is 10 A.

As can be seen in the inset, the temperature of the PCS begins to increase 31 ms after the heat is turned on. The maximum value of the temperature reaches 19.6 K at this heating condition, and the unstable behavior such as quench is not observed. Since the typical value of the critical temperature of the Nb-Ti superconducting wire is 9.6 K, it can be reasonably considered that the PCS becomes off-state (normal-conducting state) when the temperature of the coil, T, exceeds 9.6 K. By using this consideration, the PCS is in an off-state for the duration of 25 s (from 6 to 31 s). That is, the fabricated PCS is successfully functioned.

6.6 Persistent Current Decay in the Superconducting Toroidal Magnet

Fig. 6.9 shows the typical measured result of the current decay of the superconducting toroidal magnet in the persistent current mode. That is, the magnet is firstly excited by using a DC current source (see I_{DC1}, Fig. 6.3) with an off-state of the PCS. After the load current reaches 10.367 A, the current decay is measured for 90 minutes by turning on the PCS (persistent current mode). As can be seen, the current is slightly decayed mainly due to the contact resistance of the superconducting coil. The current is decreased to be 10.355 A at t = 90 minutes, and the corresponding decayed current $\triangle I_{\mathrm{decay}}$ is 12 mA.

The total contact resistance in the 6-toroidal load magnet can be calculated by the use of RL circuits. The equation of I for RL circuit is expressed as

$$i = i_0 \mathrm{e}^{-\frac{R}{L}t} \tag{6.1}$$

where R, L, and t denote the total contact resistance, the inductance of load magnet, and time (in seconds), respectively. The symbols of i and i_0 represent decayed current and initial current, respectively. From two arbitrary points such as (0 s, 10.367 A) and (1500 s, 10.364 A) in the measured results in Fig. 6.9, the values R and i_0 are calculated as 0.115 μΩ and 10.367 A, respectively. Then, the equation (6.1) is expressed as,

$$i = 10.367\mathrm{e}^{-\frac{0.115\times10^{-6}\,\Omega}{0.543\ \mathrm{H}}t} \tag{6.2}$$

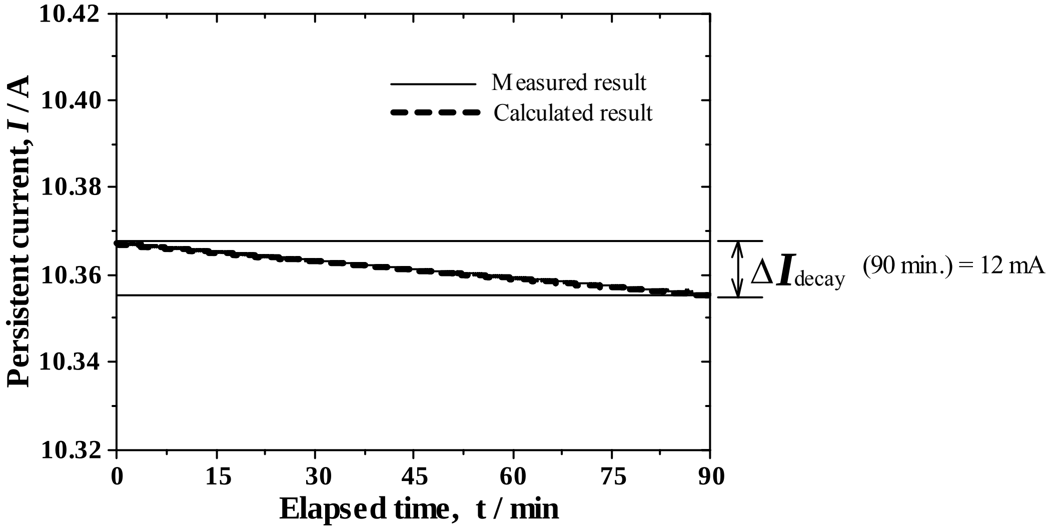

Fig. 6.9 Measured result of superconducting load current decay with the toroidal load magnet during 90 minutes. The measured temperature is 4.2 K.

The calculated persistent current decay using the equation (6.2) is plotted as a dotted line in Fig. 6.9. The calculated time constant τ ($=\frac{L}{R}$) is 4.72×10^6 s.

6.7 Current Compensation Performance

In this section, the above-mentioned current decay (section 6.6) is compensated by means of the developed LTMFP. The validity of our proposal is experimentally confirmed here. In this experiment, we select 10 A as an operating load current. For the operation of the LTMFP, the DC bias current and the peak value of the AC current are set to be, respectively, 6.1 A and 4.2 A_{peak}. We test for two driving frequencies at 15 Hz and 20 Hz.

As is already mentioned in subsection 1.3.1, the persistent current decay for recently developed HTS magnet (2.4 H) in the Maglev train reached below 10 %/day (= 0.42 %/hr). In order to achieve the operation of the Maglev train continuously, the persistent current decay needs to be compensated. As a practical evaluation, the fabricated current compensator is set to achieve pumping current 1 mA per one action in the operating current 10 A (the corresponding control rate is 0.01 %).

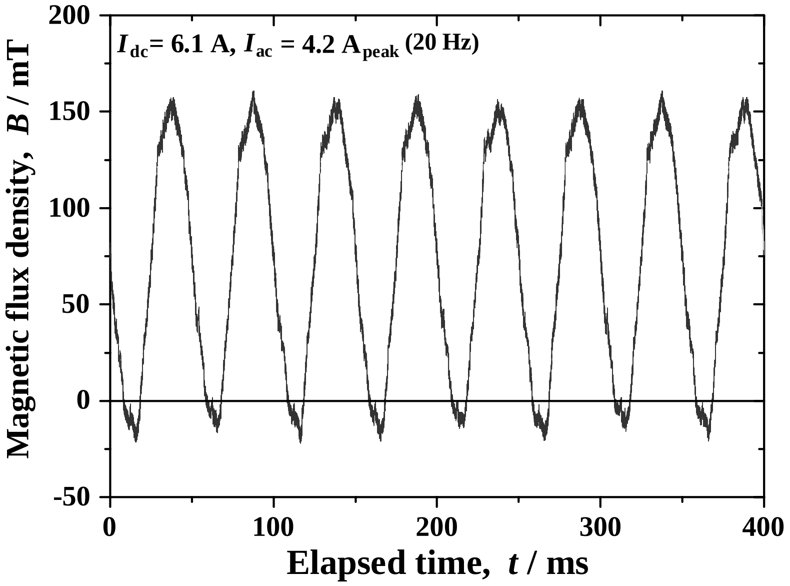

Fig. 6.10 Temporal variation of the magnetic flux density at the central part in the air gap of the LTMFP with DC bias current at 6.1 A and AC current at 4.2 A_{peak}. The measured temperature is 4.2 K. A similar waveform is also observed for 15 Hz.

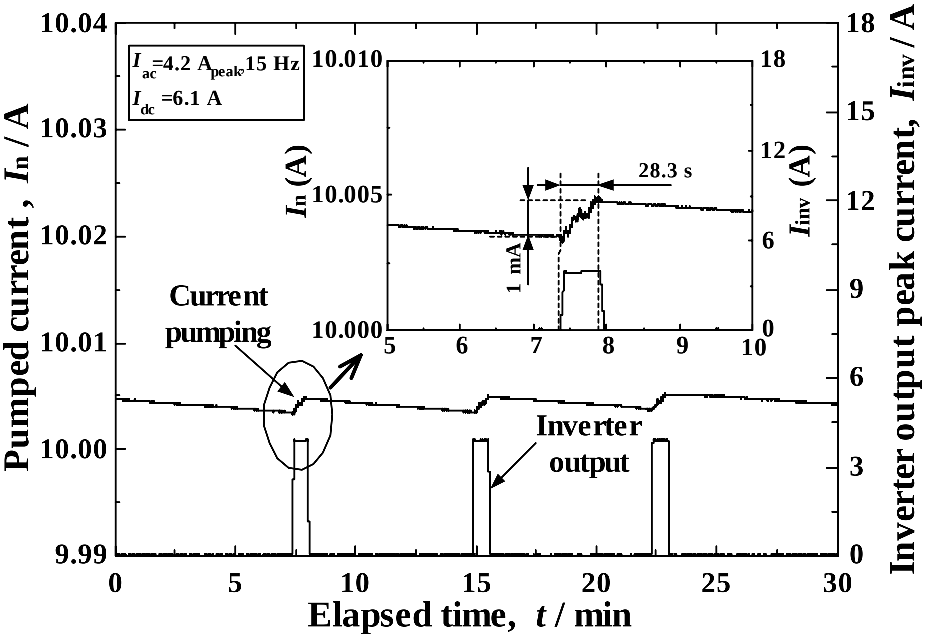

Fig. 6.11 Current compensation of superconducting toroidal magnet by means of LTMFP with the condition of DC bias current at 6.1 A and AC current at 4.2 A_{peak} (15 Hz).

Fig. 6.10 shows the temporal variations of the magnetic flux density at the central air gap of the LTMFP at 20 Hz. A similar waveform is also observed for the frequency at 15

Hz. Under this condition, the range of the magnetic flux density is between 155 and -20 mT; the traveling magnetic flux density is realized.

Fig. 6.11 shows the compensation performance of the LTMFP by means of the feedback control circuit under the operating load current I_{op} at 10 A. The driving frequency of the LTMFP in this figure is 15 Hz. As can be seen in the figure, the performance of current compensation can be successfully realized. Namely, we observe the load current for 30 minutes and current is maintained to be 10.004 A (+1 mA and -0 mA). During the measurement, the LTMFP is excited three times. The corresponding energy consumption of the LTMFP is about 72 μW/hr (= 12 μW×6).

The inset also shows the enlarged curve of the pumping up operation. As can be seen in the figure, the load current increases almost linearly. The pumped current reaches 1 mA by operating LTMFP for 28.3 s.

In order to confirm the performance of the current compensator in the different driving frequencies, the experiment LTMFP is also performed at 20 Hz. As shown in Fig. 5.13, the pumping current rate is maximized at this driving frequency. Fig. 6.12 shows the periodically measured results of the compensating current at 1 mA with DC bias current at 6.1 A and AC current at 4.2 A_{peak} (20 Hz).

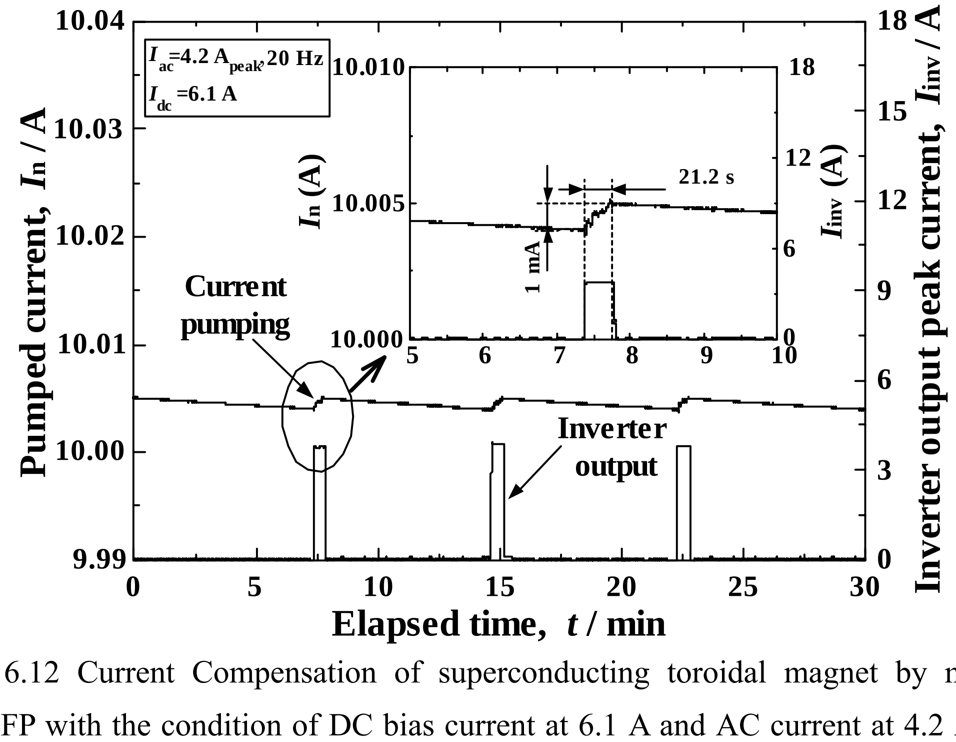

Fig. 6.12 Current Compensation of superconducting toroidal magnet by means of LTMFP with the condition of DC bias current at 6.1 A and AC current at 4.2 A_{peak} (20 Hz).

Table 6.1 Measured results of pumped current of the current compensator.

L (H)	I_{DC} (A)	I_{AC} (A_{peak})	I_{op} (A)	f (Hz)	Pumping current rate (μA/s)
543	6.1	4.2	10	15	35
				20	47

As can be seen in the figure, the performance of current compensation can be successfully realized for the duration of 30 minutes. The pumped current reaches 1 mA by operating LTMFP for 21.2 s. The rate of pumping current by the current compensator is summarized in Table 6.1. The rate at 20 Hz is surely higher than that at 15 Hz.

6.8 Summary

In this chapter, the operation of the proposed current compensator has successfully been executed. The current compensation is developed with the use of the LTMFP and the feedback control circuit. From the results, the current compensator using the LTMFP presented one solution for the problem of the current decay in the superconducting magnets without PCS operations. The obtained results are summarized as follows:

(1) The current decay in the closed persistent current loop occurs for the operating load current at 10 A, due to the connection resistance (0.115 μΩ). The persistent current decay of the toroidal magnet reached 12 mA under the duration of 90 minutes operation. Due to such persistent current decay, the toroidal load magnet can be served as a small scale HTS magnet that has the persistent current decay.

(2) The compensating performance using the current compensator has been realized in the persistent current mode (operating current at 10 A). The pumping current, 1 mA per one action, has successfully been generated in the different driving frequencies (15 and 20 Hz). This means that the corresponding control rate of the load current is 0.01 % ($= \frac{1\ \text{mA}}{10\ \text{A}} \times 100$).

Consequently, the technology using the LTMFP and the feedback control circuit unit has been evaluated as a superconducting current compensator for the superconducting magnet systems. This approach with the use of the LTMFP is the first proposal for the new type of the current compensator.

Chapter 7 Conclusions

This thesis has proposed the Linear Type Magnetic Flux Pump (LTMFP) that is based on the principle of the linear induction motor. Compared with early-developed flux pumps, the LTMFP has some merits; the LTMFP generates pumping current without mechanically rotating systems, as well as, having a simplified control sequence.

For theoretical analysis, the modified pumping equation (2.30) was derived in order to explain the operating characteristics of the LTMFP. The modified equation is based on the phenomenon of the enhancement of the normal spot in the penetrated moving flux. The 3-D FEM simulation numerically confirmed this phenomenon.

The performance of the fabricated LTMFP was experimentally investigated under various conditions. The measured pumping actions of the LTMFP can be explained by the modified equation (2.30). The operating characteristics of the LTMFP were then effectively explained by the phenomenon of the enhancement of the normal spot. This analytical approach of enhancement of normal spot is the first proposal in this study.

In order to achieve the current compensator for the superconducting magnet systems, we introduced and implemented a new type of current compensator, which consists of the LTMFP and a feedback control circuit. Compared with the already developed superconducting current supplies, the introduced current compensator easily controls a compensating current with the LTMFP. Through practical tests, the current compensator was able to generate the compensating current at as little as 1 mA scale in the operating current of 10 A (the corresponding control rate is 0.01 % ($= \frac{1\ \text{mA}}{10\ \text{A}} \times 100$)). Thus, the possibility of the new type of current compensator was confirmed.

From this study, the guideline for the technology of the new type of current compensator has been established. The conclusions for every chapter are summarized as follows:

In chapter 1, the background of the superconductivity and the fundamental aspects of a superconductor have been explained in order to understand the superconductivity field. In addition, the current status of development of superconducting magnets as well as the required technologies for application development was introduced. In the application of superconducting magnet systems, the necessity of the current compensator using a superconducting flux pump and the purpose of this study were explained. Further, outline of this thesis was summarized.

In chapter 2, the operating principle and theoretical analysis of the LTMFP were explained in detail. The operating mechanisms of the already developed flux pumps and their problems were described. In order to solve these problems, we proposed a new type of flux pump called linear type magnetic flux pump (LTMFP). The operating mechanism of the proposed LTMFP and operating merits were explained. In addition, the explanation of the operating characteristics of the LTMFP and theoretical equation, which is based on the phenomenon of enhancing the normal spot, was introduced. The enhancement of the normal spot is considered to be due to the magnetic diffusion in a superconductor. Based on the theoretical equation, the operating characteristics of the LTMFP were discussed.

In chapter 3, the magnetic behavior of the superconducting Nb foil was analyzed using a 3-D FEM simulation. The operating conditions of the DC bias current and the AC current were obtained by 3-D FEM analysis. In addition, in order to confirm the introduced phenomenon of the enhancement of the normal spot in chapter 2, the phenomenon of magnetic diffusion in superconductor was simulated. Through the simulated results, the enhancing rate of the normal spot according to the driving frequency was obtained. The validity of the simulation code was verified by comparing to the characteristic time of the magnetic diffusion that is suggested by the analytical equation.

In chapter 4, the fabrication of the LTMFP system was described. Referring to the simulation model in chapter 3, all components of the LTMFP, which consist of a couple of DC bias coils, AC armature coils, a laminated silicon steel core, and a superconducting Nb foil, were fabricated. In addition, in order to estimate the operating characteristics of LTMFP, two types of load magnets and a thermal-type PCS were fabricated. In addition, in order to estimate the operating characteristics of LTMFP, two types of load magnets and a thermal-type PCS were fabricated.

In chapter 5, the experimental performances of the fabricated LTMFP were investigated. The validity of the obtained values of the DC bias current and the AC current by 3-D FEM in chapter 3 was confirmed based on the performance evaluations. In addition, the experimental investigation was carried out with a small-scale load magnet of 1.3 mH in order to observe the pumping current of the LTMFP. In order to estimate the enhancing rate of the normal spot k, the calculation sequence of the pumping current was introduced. Based on the calculation sequence of the pumping current, the calculated values k = 0.14 mm/Hz below 20 Hz and k = 0.63 mm/Hz over 20 Hz were estimated, respectively. The validity of the obtained k values was also verified by comparing with the experimental results for the toroidal load magnet (543 mH). That is, the measured results were explained by the modified equation in chapter 2. Further, the characteristic frequency, (20 Hz) at which the pumping current rate shows the peak value, agreed comparatively with the simulated results in chapter 3. Thus, the pumping current characteristics in the LTMFP could be explained by the phenomenon of the enhancement of the normal spot in the penetrated moving flux discussed in chapter 2. From the various experimental performances, the pumped currents according to the different driving frequencies, the different amplitudes of the applied magnetic fields, and the different load magnets were investigated, respectively. As a fundamental test for the current compensator, the pumping-up and down operations of the LTMFP system were performed under the operating load current at 10 A. From this basic observation, it was deduced that the LTMFP can be applied to the current compensator in the persistent current mode.

In chapter 6, the assembly and the experimental performance of the current compensator were carried out. As one of the new solutions for the persistent current decay in a superconducting magnet, a current compensator that is composed of a LTMFP and a feedback control circuit was introduced. As a practical test, the compensating performance using the LTMFP has been executed in the persistent current mode (operating current at 10 A). The pumping current, 1 mA scale per one action, has successfully been generated at 15 and 20 Hz (the corresponding control rate of the load current is 0.01 % ($= \frac{10^{-3}\,\mathrm{A}}{10\ \mathrm{A}} \times 100$)). In conclusion, from the experimental evaluation, the technology using the LTMFP has been achieved as a superconducting current compensator for persistent current decay in a superconducting magnet. This basic study presented a guideline in regards to the new current compensator with LTMFP.

The subjects on the proposed LTMFP for future study are as follows:

1. Development of the large-scale LTMFP is important in order to compensate the larger current in a practical sized superconducting magnet.
2. The investigation has to be carried out by means of the real HTS load magnet.

Acknowledgement

The author would like to acknowledge his sincere gratitude to Professor Takashi Hikihara, graduate school of engineering, Kyoto University, for his helpful discussions and suggestions. The author would like to thank Professor Tetsuo Kobayashi, graduate school of engineering, Kyoto University, for the important discussions. The author is also grateful to Associate Professor Taketsune Nakamura, graduate school of engineering, Kyoto University, for the continuing guidance, valuable suggestions and supports throughout his work.

The author is deeply indebted to Professor Emeritus of Kyoto University Itsuya Muta, and Professor Tsutomu Hoshino, Meisei University, for their supports throughout this work. The author wishes to appreciate to Professor Tae Kuk Ko, Yonsei University, and Professor Hyun Ki Kim, Suwon University, and Associate Professor Hyung Keun Ahn, Konkuk University, for their hearty considerations and valuable discussions. The author wishes to express to his gratitude to Dr. Myung Whan Sohn, Senior Researcher of KERI, Dr. Young Sik Choi, Technical Manager of CAST, Dr. Hyun Man Jang, Researcher of LG Cable Research Center and all the members of applied superconductivity laboratory for their technical advices and fruitful supports to his work.

The author wishes to express his deepest appreciation to his father, mother, little brother, wife and wife's family for their prayer, encouragement and understanding during his study in Japan.

Finally, the author would like to express his highly adoration to the Almighty God for the God's sincerity and obligation.

This work was supported by the Japanese Government Scholarship of the Ministry of Monbusho (No. 14655107) and the 21st century COE program (No. 14213201) in Japan.

Yoon Do Chung

References

1. A. Rose-Innes and E. Rhderick, "Introduction to superconductivity," *Oxford: Pergamon Press*, pp. 3-15, 1978.
2. Y. Iwasa, "Case studies in superconducting magnets design and operational issues," *Plenum Press*, pp. 7-15, 295-306, 1994.
3. L. Horng, J.C. Wu and T.C. Wu, "Flux pining force Nb thin films with periodic vortex pinning arrays," *Journal of Applied Physics*, vol. 91, no. 10, pp. 8510-8512, May 2002.
4. T. Kiyoshi, A. Sato, H. Wada, S. Hayashi, M. Shimada and Y. Kawate, "Development of 1 GHz superconducting NMR magnet at TML/NRIM," *IEEE Transactions on Applied Superconductivity*, vol. 9, no. 2, pp. 559-562, June 1999.
5. W.D. Markiewicz and R.E. Goddard, "Bronze tin content and grain size in Nb/sub 3/Sn composite superconductors," *IEEE Transactions on Applied Superconductivity*, vol. 12, no. 1, pp. 1063-1066, March 2002.
6. S. Masuyama, H. Yamamoto and Y. Matsubara, "A Nb-Ti split magnet directly cooled by a cryocooler," *IEEE Transactions on Applied Superconductivity*, vol. 3, no. 1, pp. 262-265, March 1993.
7. C.G. Kuper, "An introduction to the theory of superconductivity," *Oxford: Clarendon Press*, pp. 8-21, 1988.
8. D. Shi, "High temperature superconducting materials science and engineering: new concepts & technology," *Elsevier Science Ltd*, *New York*, pp. 3-21, 1995.
9. H. Kitaguchi, "*V-I* characteristics of MgB_2 PIT composite tapes: *n*-value under strain, in high field, or at high temperature," *Physica C*, vol. 401, pp. 246-250, 2004.
10. M. Tinkham, "Introduction to superconductivity," *New York*, *NY: McGraw-Hill Press*, pp. 5-9, 1975.
11. T.P. Orland and K.A. Delin, "Foundations of applied superconductivity," *Addison Wesley Press*, pp. 38-39, 1991.
12. K.A. Ziq, P.C. Canfield, J.E. Ostenson and D.K. Finnemore, "Scaling of flux pinning with the thermodynamic critical field," *Physical Review B*, vol. 60, no. 5, pp. 3604-3607, 1999.
13. M.N. Wilson, "Superconducting magnets," *Oxford University Press*, pp. 4-21, 1983.
14. T. Matsushita, N. Harada, K. Yamafuji and M. Noda, "Hysteresis loss in a type-II superconductor in the regime of reversible fluxoid motion," *Japanese Journal of Applied Physics*, vol. 28, no. 3, pp. 356-360, March 1989.

15. M.P. Omen, “AC loss in superconducting tapes and cables,” *Ph.D. Dissertation of Twente University*, *Nederland*, pp. 15-31, 2000.
16. M.M. Farhoudi, “AC loss in Ag/Bi-2223 tapes in AC field,” *Master Thesis of University of Wollongong*, *Australia*, pp. 18-26, 2002.
17. J.H. Kim, K.T. Kim, S.H. Jang, J.H. Joo, S.Y. Choi, W.S. Nah, H.K. Kang, T.K. Ko, H.S. Ha, S.S. Oh, K.S. Ryu and P. Nash, “Measurement of joint properties of Bi(Pb)-Sr-Ca-Cu-O (2223) tapes by field decay technique,” *IEEE Transactions on Applied Superconductivity*, vol. 13, no. 2, pp. 2992-2995, June 2003.
18. J.R. Groves, P.N. Arendt, S.R. Foltyn, R.F. Depaula, E.J. Peterson, T.G. Holesinger, J.Y. Coulter and R.W. Springer, “Ion-beam assisted deposition of Bi-axially aligned MgO template films for YBCO coated conductors,” *IEEE Transactions on Applied Superconductivity*, vol. 9, no. 2, pp. 1964-1966, June 1999.
19. Y. Iwasa, “HTS magnets; stability; protection; cryogenics; economics; current stability/protection activities at FBML,” *Cryogenics*, vol. 43, pp. 303-316, 2003.
20. J.H. Kim, K.T. Kim, J.H. Joo, S.Y. Choi, W.S. Nah, H.S. Ha and S.S. Oh, “Measurement of joint resistance of Bi-2223/Ag tapes using field decay technique,” *Korea Institute of Applied Superconductivity and Cryogenics*, *Conference 2003*, pp. 294-296, Feb. 2003.
21. M. Igarashi, H. Nakao, M. Terai, T. Kuriyama, S. Hanai, T. Yamashita and M. Yamaji, “Persistent current HTS magnet cooled by cryocooler (1)-project overview,” *IEEE Transactions on Applied Superconductivity*, vol. 15, no. 2, pp. 1469-1472, June 2005.
22. J.E.C. William and E.S. Bobrov, “MRI magnet for imaging,” *Journal De Physique*, vol. 45, no. 1, pp. 691-694, 1984.
23. S. Kusada, M. Igarashi, K. Kuwano, K. Nemoto, S. Hirano, T. Okutomi, M. Terai, T. Kuriyama, K. Tasaki, T. Tosaka, K. Marukawa, S. Hanai, T. Yamashita, Y. Yanase, H. Nakao and M. Yamaji, “Persistent current HTS magnet cooled by cryocooler (2)-magnet configuration and persistent current operation test,” *IEEE Transactions on Applied Superconductivity*, vol. 15, no. 2, pp. 2285-2288, June 2005.
24. K. Tasaki, T. Tosaka, K. Marukawa, T. Kuriyama, S. Hanai, M. Yamaji, K. Kuwano, M. Igarashi, K. Nemoto, S. Hirano, T. Okutomi, H. Nakao and M. Terai, “Persistent current HTS magnet cooled by cryocooler (3)-HTS magnet characteristics,” *IEEE Transactions on Applied Superconductivity*, vol. 15, no. 2, pp. 2289-2292, June 2005.

25. T. Tosaka, T. Marukawa, T. Kuriyama, H. Nakao, M. Yamaji, K. Kuwano, M. Igarashi, K. Nemoto and M. Terai, “Persistent current HTS magnet cooled by cryocooler (4)-persistent current switch characteristics,” *IEEE Transactions on Applied Superconductivity*, vol. 15, no. 2, pp. 2293-2296, June 2005.
26. H. Nagai, “Development and testing of super fluid-cooled 900 MHz NMR magnet,” *Cryogenics*, vol. 41, no. 2, pp. 623-630, 2001.
27. M.P. Omen, M. Leghissa, G. Ries, N. Proelss, H.W. Neumueller, F. Steinmeyer, M. Vester and F. Davies, “HTS flux pump for cryogen-free HTS magnets,” *IEEE Transactions on Applied Superconductivity*, vol. 15, no. 2, pp. 1465-1468, June 2005.
28. T. Kiyoshi, “Persistent mode operation of a 920 MHz high-resolution NMR magnet,” *IEEE Transactions on Applied Superconductivity*, vol. 12, pp. 711-716, 2002.
29. J. Bascunan, “A low and high-temperature superconducting NMR magnet: design and performance results,” *IEEE Transactions on Applied Superconductivity*, vol. 13, no. 2, pp. 1550-1553, June 2003.
30. G. Morrow, “Progress in MRI magnets,” *IEEE Transactions on Applied Superconductivity*, vol. 10, no. 1, pp. 744-751, March 2001.
31. P. Jezzard, “Functional MRI an introduction to methods,” *Oxford University Press*, pp. 12-45, 1998.
32. A.A. Zhukov, J.P. Ströbel, P. Kummeth, M. Kraus, S. Peehs, W. Schindler, I. Khasanow, H.W. Neumüller, G. Saemann-Ischenko, A.A. Yarygin and S.I. Krasnosvobodtzev, “Comparative study of magnetic and transport properties and *E-J* characteristics analysis of epitaxial YBa_2Cu_7- thin films,” *Cryogenics*, vol. 33, pp. 142-146, 1993.
33. T. Wakuda, T. Nakano, M. Iwakuma, K. Funaki, M. Takeo, K. Yamafuji, Y. Yamada and S. Yasuhara, “*E-J* characteristics and a.c. losses in a superconducting Bi (2223) hollow cylinder,” *Cryogenics*, vol. 37, pp. 381-388, July 1997.
34. J. Bae, Y. Oh, S. Lee and T.K. Ko, “The design, manufacture and characteristic experiment of a superconducting excitation coil,” *IEEE Transactions on Applied Superconductivity*, vol. 2, pp. 672-675, July 1997.
35. C. Schmidt, “Temperature dependence of ac-losses in multifilamentary Bi-2223 tapes between 4.2 K and T_c,” *Cryogenics*, vol. 44, pp. 187-195, 2004.
36. A.K. Ghosh, “*V-I* transition and *n*-value of multifilamentary LTS and HTS wires and cables,” *Physica C*, vol. 401, pp. 15-21, 2004.

37. L. Horng and C.H. Tai, "Critical persistent current for a loop formed by a Bi-2223 Ag-sheathed superconducting tape," *IEEE Transactions on Applied Superconductivity*, vol. 11, no. 1, pp. 3006-3009, March 2001.
38. J.H. Kim, K.T. Kim, J.H. Joo, S.Y. Choi, W.S. Nah, H.S. Ha and S.S. Oh, "Measurement of joint resistance of Bi-2223/Ag tapes using field decay technique," *Korea Institute of Applied Superconductivity and Cryogenics, Conference 2003*, pp. 294-296, Feb. 2003.
39. A. Rimikis, R. Kimmich and T. Schneider, "Investigation of *n*-value of composite superconductors," *IEEE Transactions on Applied Superconductivity*, vol. 10, no. 1, pp. 1239-1241, March 2000.
40. P. Lezza, "Transport properties and exponential *n*-value of Fe/MgB_2 tapes with various MgB_2 particle sizes," *Physica C*, vol. 401, pp. 305-309, 2004.
41. A. Street, "Superconducting magnets get bigger and better," *The Industrial Physicist*, pp. 32-38, 2002.
42. J. Benjamin, "A 'permanent' high-temperature superconducting magnet operated in thermal communication with a mass of solid nitrogen," *Cryogenics*, vol. 42, pp. 229-233, 2002.
43. Y. Iwasa, "Microampere flux pump for superconducting NMR magnets Part 1; basic concept and microtesla flux measurement," *Cryogenics*, vol. 41, pp. 385-391, 2001.
44. H.G. Lee, H.M. Kim and Y. Iwasa, "A flux pump for an NMR magnets," *IEEE Transactions on Applied Superconductivity*, vol. 13, no. 2, pp. 1640-1643, June 2003.
45. G.C. Xiong, F.R. Wang, S.Z. Wang, Q.D. Jiang, J.Y. Li, Z.J. Yin, C.Y. Li and D.L. Yin, "Critical current density and flux creep in epitaxial $YBa_2Cu_3O_{7-x}$ thin films," *Cryogenics*, vol. 30, pp. 448-450, May 1990.
46. S.L. Wipf, "A superconducting direct-current generator," *Advanced in Cryogenics Engineering*, vol. 9, pp. 342-348, 1964.
47. T. Buchhold, "Superconductive power supply and its application for electrical flux pumping," *Cryogenics*, vol. 4, pp. 212-215, 1964.
48. O.A. Shevchenko, "Novel supplies for powering a superconducting magnet," *IEEE Transactions on Applied Superconductivity*, vol. 10, no. 1, pp. 1414-1417, March 2000.
49. O.K. Mawardi and T.K. Ko, "Brushless superconducting alternators," *IEEE Transactions on Magnetics*, vol. 13, no. 1, pp. 780-783, 1977.
50. W. Qiuliang, "Study of full-wave superconducting rectifier-type flux-pumps," *IEEE Transactions on Magnetics*, vol. 28, no. 1, pp. 2699-2702, 1996.

51. S.K. Jeong, "Experiment of flux pump for high temperature superconductor insert coils of NMR magnets," *Journal of the Korea Institute of Applied Superconductivity and Cryogenics*, vol. 3, no. 2, pp. 15-20, Nov. 2001.
52. V.V. Vasiliev, V.N. Isaykin, O.D. Kanzyuba, V.G. Kozrezov, V.A. Kulagin, A.A. Markov, V.D. Raev, A.N. Romanv, B.Y. Serebryakov, N.A. Sysoev, A.A. Forostenko, V.Y. Pakhomov and E.B. Klimova, "Experimental-model of a flux pump," *Cryogenics*, vol. 29, pp. 1015-1017, Oct. 1989.
53. Y.S. Yoon, M.C. Ahn, H.M. Kim and T.K. Ko, "Determination of equivalent circuit parameters of the low-T_c superconducting power supply for charging of superconducting magnet," *IEEE Transactions on Applied Superconductivity*, vol. 13, no. 2, pp. 2222-2226, June 2003.
54. W.D. Markiewick, "Current injection for field decay compensation in NMR spectrometer magnet," *IEEE Transactions on Applied Superconductivity*, vol. 12, pp. 1886-1890, Dec. 2002.
55. H.V. Beelen, "A 25000 gauss, 175 amperes Nb-25% Zr wire magnet FED by a flux pump," *Physics letters*, vol. 7, no. 3, pp. 175-176, Nov. 1963.
56. J.V. Suchtelen, J. Volger and D.V. Houwelingen, "The principle and performance of a superconducting dynamo," *Cryogenics*, vol. 5, no. 5, pp. 256-266, Oct. 1965.
57. H.V. Beelen, J.P.T. Arnold, H.A. Sypkens, J.P. Van, B. Houckgeest, R.B. Ouboter, J.J.M. Beenakker and K.W. Taconis, "Flux pumps and superconducting solenoid-s," *Physica*, vol. 31, pp. 413-443, 1965.
58. O.K. Mawardi and T.K. Ko, "Operational characteristics of a flux pump," *IEEE Transactions on Magnetics*, vol. 15, no. 1, pp. 828-831, 1979.
59. O.K. Mawardi, "Armature reaction in a flux pump," *IEEE Transactions on Magnetics*, vol. 23, no. 2, pp. 587-590, March 1987.
60. T. Hoshino, A. Kawasaki, M. Nishikawa, K.M. Salim, I. Muta and T. Nakamura, "Design of 6.6 kV, 100 A saturated DC reactor type superconducting fault current limiter," *IEEE Transactions on Applied Superconductivity*, vol. 13, no. 2, pp. 2012-2015, June 2003.
61. I. Muta, "Preliminary experiments for possibility of brushless superconducting synchronous generator excited by magnetic flux pump," *Proceedings of ICEM '84*, *Laussanne Swiss*, pp. 1118-1121, 1984.

62. H. Tsukiji, T. Hoshino and I. Muta, “Characteristics of exciting superconducting magnet by magnet flux pump,” *Transactions of IEE of Japan*, vol. 116-D, no. 2, pp. 183-190, Feb. 1996.
63. H. Tsukiji, K.D. Choi, M. Tsukiyama, T. Nishiya, T. Hoshino, I. Muta and E. Mukai, “Test of high-voltage output magnetic flux pump for superconducting magnet,” *Proceedings of 16th ICEM / ICMC*, *Kitakyuushu Japan*, pp. 953-956, May 1996.
64. T. Hoshino, M. Eguchi, T. Konishi, I. Muta, T. Nakamura, H. Tsukiji and M. Noguchi, “Turn off trigger energy characteristics of the superconducting power electronics device (S-PED),” *IEEE Transactions on Applied Superconductivity*, vol. 9, no. 2, pp. 1221-1224, June 1999.
65. H.M. Kim, Y.S. Yoon and T.K. Ko, “The characteristics analysis of e.m.f. induced by moving normal spot in a cylindrical superconducting foil,” *Progress in Superconductivity*, vol. 1, no. 2, pp. 99-104, Feb. 2000.
66. M.S. Joo and T.K. Ko, “The determination of equivalent circuit parameters due to continuous switching action in the superconducting flux pump,” *IEEE Transactions on Applied Superconductivity*, vol. 7, no. 2, pp. 668-671, June 1997.
67. H. Tsukiji, K.D. Choi, M. Tsukiyama, T. Nishiya, T. Hoshino, E. Mukai and I. Muta, “Test of disk type magnetic flux pump with the ability of high voltage output,” *IEEE Transactions on Applied Superconductivity*, vol. 7, no. 2, pp. 394-397, June 1997.
68. H.G. Lee, J. Bascunan and Y. Iwasa, “A high-temperature superconducting double-pancake insert for an NMR magnet,” *IEEE Transactions on Applied Superconductivity*, vol. 13, no. 2, pp. 1546-1549, June 2003.
69. Y. Iwasa, “NMR/MRI superconducting magnet technologies: recently activities at MIT francis bitter magnet laboratory,” *Journal of the Korea Institute of Applied Superconductivity and Cryogenics*, vol. 5, no. 1, pp. 1-12, 2003.
70. T.K. Ko and O.K. Mawardi, “Current distribution in a moving spot flux pump,” *IEEE Transactions on Magnetics*, vol. 23, no. 2, pp. 584-586, 1987.
71. H.M. Kim, C.J. Lee, T.K. Ko, Y.S. Yoon, S.J. Lee, T.S. Han and S.S. Oh, “Design, fabrication and test of a discrete-foil-type superconducting power supply,” *Cryogenics*, vol. 41, pp. 189-194, 2001.
72. Y.S. Yoon, S.J. Lee, H.M. Kim and T.K. Ko, “Analysis of the operational characteristics of a heater-trigger type high-T_c superconducting power supply,” *IEEE Transactions on Applied Superconductivity*, vol. 9, no. 4, pp. 4708-4714, Dec. 1999.

73. S.K. Jeong, S.H. In and S.H. Kim, "Superconducting micro flux pump using a cryotron-like switch," *IEEE Transactions on Applied Superconductivity*, vol. 13, no. 2, pp. 668-671, June 2003.
74. D. Atherton, "Transformer-rectifier flux pump using inductive current transfer Nb_3Sn cryotrons," *Review Science Instrument*, vol. 50, pp. 1245-1248, 1979.
75. L.J.M. Klundert and H.H.J. Tenkate, "Fully superconducting rectifiers and flux pumps," *Cryogenics*, vol. 21, pp. 195-206, 1981.
76. W. Qiuliang, Y. Wang and Y.L. Yan, "Study of full-wave superconducting rectifier-type flux–pumps," *IEEE Transactions on Magnetics*, vol. 28, no. 1, pp. 2699-2702, 1996.
77. Y.D. Chung, I. Muta, T. Hoshino and T. Nakamura, "Performances of a linear type magnetic flux pump for compensating a little decremented persistent current of HTS magnets," *IEEE Transactions on Applied Superconductivity*, vol. 14, no. 2, pp. 1723-1726, June 2004.
78. Y.D. Chung, I. Muta, T. Hoshino, T. Nakamura and T.K. Ko, "Pumping-up current characteristics of linear type magnetic flux pump," *Journal of the Korea Institute of Applied Superconductivity and Cryogenics*, vol. 6, no. 2, pp. 29-34, May 2004.
79. Y.D. Chung, I. Muta, T. Hoshino, T. Nakamura and M.H. Sohn, "Design and performance of compensator for decremental persistent current in HTS magnets using linear type magnetic flux pump," *Cryogenics*, vol. 44, no. 11, pp. 839-844, Nov. 2004.
80. Y.D. Chung, I. Muta, T. Hoshino and T. Nakamura, "Characteristics of current compensator for persistent current in NMR magnets with use of linear type magnetic flux pump," *2004 National Convention IEE of Japan*, vol. 5, no. 5-038, pp. 44-45, March 2004.
81. Y.D. Chung, I. Muta, T. Hoshino, H.J. Jung and T. Nakamura, "Test of linear type magnetic flux pump for compensating persistent current in superconducting magnets under pre-charged operational current," *70th Meeting on Cryogenics and Superconductivity CSJ-2004*, *Yokohama Japan*, vol. 70, no. 1E-p21, pp. 75, May 2004.
82. J. Volger, "The generator of heavy currents in superconducting circuits," *Advanced Cryogenics*, *New York Plenum Press*, pp. 98-112, 1965.
83. I. Muta, H. Tsukiji, N. Handa, T. Hoshino and E. Mukai, "The effect of excitation methods on electrical characteristics of fully superconducting generator model," *IEEE Transactions on Magnetics*, vol. 30, no. 4, pp. 2030-2033, July 1994.
84. H. Tsukiji, I. Muta, T. Hoshino and E. Mukai, "Output power limiter of 200 MW class blushless superconducting generator excited with magnet flux-pump," *IEEE Transactions on Applied Superconductivity*, vol. 11, no. 1, pp. 2335-2338, March 2001.

85. J.V. Suchtelen, “The principle and performance of a superconducting dynamo,” *Cryogenics*, vol. 5, no. 10, pp. 256-266, 1965.
86. I. Muta, H. Tsukiji, Y. Tsutsui, T. Hoshino, E. Mukai and T. Furukawa, “Fully superconducting AC generator with brushless excitation system,” *11th International Conference on Magnet Technology*, vol. 1, pp. 568-573, Aug. 1990.
87. R. Kupferman, “Normal zone in large composite superconductors,” *Cryogenics*, vol. 32, no. 5, pp. 1190-1193, 1988.
88. I. Muta, H. Tsukiji, T. Itoh, S. Ishii, T. Hoshino and E. Mukai, “Superconducting dynamo and its application to superconducting generator,” *Cryogenics*, vol. 30, pp. 749-752, Sept. 1990.
89. S. Stintzing and W. Zwerger, “Ginzburg-Landau theory of superconductors with short coherence length,” *Physical Review B*, vol. 56, no. 14, pp. 9004-9014, 1997.
90. B.Y. Shapiro, I. Shapiro, B. Rosenstein and P.J. Lin, “Fast phase transition and shock waves of the vortex matter in type-II superconductors,” *Holon Academic Institute of Technology Journal of Science and Engineering*, vol. 1, no. 4, pp. 721-742, 2004.
91. M.N. Wilson, “Superconducting magnets,” *Clarendon Press*, pp. 143-144, 1983.
92. P.P. Silverster and R.L. Ferrari, “Finite elements for electrical engineers,” *Cambridge University Press*, pp. 35-42, 1996.
93. T. Nakada, “Numerical analysis of flux and loss distribution in electrical machinery,” *IEEE Transactions on Magnetics*, vol. 20, no. 5, pp. 1750-1755, 1984.
94. M.N.O. Sadiku, “Numerical techniques in electromagnetics,” *CRC Press*, pp. 2-46, 407-424, 1999.
95. Photo-series simulation program user manual, version 8.2, *Numerical simulation Tech Co. Ltd*, pp. 82-111, 2003.
96. R.P. Huebener, R.T. Kampwirth, R.L. Martin, T.W. Baebee and R.B. Zubeck, “Critical current density in superconducting niobium films,” *Journal of Low Temperature Physics*, vol. 19, no. 3, pp. 247-258, 1975.
97. S.A. Nasar and I. Boldea, “Linear motion electric machines,” *Wiley-Interscience Publication*, pp. 58-59, 1976.
98. J. Cathey, R. Calvin and A. Ayoub, “Transient load model of an induction machine,” *IEEE Transactions on Power Apparatus and System*, vol. 92, pp. 1399-1406, 1973.
99. M.S. Sarma, “Electric machines,” *West Publishing Company*, pp. 350-400, 1994.

100. D. Kelly, “Performance and control of electrical machines,” *McGraw Hill Book Company*, pp. 78-89, 1992.

101. P. Tixador, “Experimental behavior of a fully superconducting machine,” *Proceedings of ICEM ’92*, *Manchester UK*, pp. 1117-1121, Sept. 1992.

102. J.F. Gieras and Z.J. Piech, “Linear synchronous motors transportation and automation systems,” *CRC Press*, pp. 71-77, 2000.

103. H.K. Kang, J.H. Kim, J.H. Joo, Y.S. Yoon and T.K. Ko, “Fabrication and test of persistent current switch for HTS magnet system,” *Journal of the Korea Institute of Applied Superconductivity and Cryogenics*, vol. 5, no. 1, pp. 92-96, 2003.

104. D.K. Bae, Y.S. Yoon, M.C. Ahn, H.S. Ha, T.K. Ko and S.S. Oh, “Characteristic analysis of a heater-triggered switching system for the changing of Bi-2223 double-pancake load,” *IEEE Transactions on Applied Superconductivity*, vol. 13, no. 2, pp. 2227-2230, June 2003.

105. J.N. Brown and Y. Iwasa, “Temperature dependent stability and protection parameters in an adiabatic superconducting magnet,” *Cryogenics*, vol. 31, pp. 341-347, 1991.

106. R.K. Ko, J.H. Bae, K.D. Sim, E.Y. Lee, H.J. Kim, Y.K. Kwon and K.S. Ryu, “Performance test a persistent current switch insulated with cotton tape,” *IEEE Transactions on Applied Superconductivity*, vol. 11, no. 1, pp. 2425-2428, March 2001.

107. R.K. Ko, J.H. Bae and Y.K. Kwon, “Optimal design of thermally trigger controlled superconducting persistent current switch,” *Internal Conference on the Korean Institute of Electrical Engineers*, pp. 1587-1590, 2002.

108. K. Noto, Y. Kono, M. Matsukawa, M. Itagaki, T. Ishida and K. Chiba, “Development of a 50 A fast-response, magnetically controlled persistent current switch,” *IEEE Transactions on Applied Superconductivity*, vol. 5, no. 2, pp. 258-261, June 1995.

109. G. Mulder, H.T. Kate, H. Krooshoop and L. Klundert, “Development of a thermally switched superconducting rectifier for 100 kA,” *IEEE Transactions on Magnetics*, vol. 27, no. 2, pp. 2333-2336, March 1991.

110. R.A. French, “Intrinsic type-2 superconductivity in pure niobium,” *Cryogenics*, pp. 301-308, 1968.

List of Publications

Reviewed papers

1. **Yoondo Chung**, Itsuya Muta, Tsutomu Hoshino and Taketsune Nakamura, "Performances of a Linear Type Magnetic Flux Pump for Compensating a Little Decremented Persistent Current of HTS Magnets," *IEEE Transactions on Applied Superconductivity*, vol. 14, no. 2, pp. 1723-1726, June 2004.
2. **Yoondo Chung**, Itsuya Muta, Tsutomu Hoshino, Taketsune Nakamura and M.H. Sohn, "Design and performance of compensator for decremental persistent current in HTS magnets using linear type magnetic flux pump," *Cryogenics*, vol. 44, no. 11, pp. 839-844, Nov. 2004.
3. Young-Sik Jo, Taketsune Nakamura, Tsutomu Hoshino, **Yoondo Chung**, Jung-Pyoo Hong and Young-Kil Kwon, "Characteristic study and three dimensional magnetic field analysis of the superconducting synchronous rotating machine," *Physica C*, vol. 416, no. 3, pp. 108-114, Dec. 2004.
4. **Yoondo Chung**, Itsuya Muta, Tsutomu Hoshino and Taketsune Nakamura, "Characteristics of a Persistent Current Compensator for Superconducting NMR Magnets using Linear Type Magnetic Flux Pump," *IEEE Transactions on Applied Superconductivity*, vol. 15, no. 2, pp. 1338-1341, June 2005.
5. **Yoondo Chung**, Tsutomu Hoshino and Taketsune Nakamura, "Current Pumping Performance of Linear-type Magnetic Flux Pump with Use of Feedback Control Circuit System", *IEEE Transactions on Applied Superconductivity*, vol. 16, no. 2, pp. 1638-1641, June 2006.

Book

1. Takatesune Nakamura, **Yoondo Chung** and Tsutomu Hoshino, "Magnetic Behaviour of Superconducting Foil Utilized for Linear-Type Magnetic Flux Pump", *Electromagnetic Fields in Mechatronics, Electrical and Electronic Engineering* (IOS press) (edited by A. Krawczyk, S. Wiak and X.M. Lopez-Fernandez), ISBN 1-58603-627-0, ISSN 1383-7281 (2006) pp. 422-427.

International Conference

1. **Yoondo Chung**, Itsuya Muta, Tsutomu Hoshino and Taketsune Nakamura, "Performances of a Linear Type Magnetic Flux Pump for Compensating a Little Decremented Persistent Current of HTS Magnets," *18th International Conference of Magnet Technology*, *Morioka Iwate Japan*, no. 5C-a03, Oct. 2003.
2. **Yoondo Chung**, Itsuya Muta, Tsutomu Hoshino, Taketsune Nakamura and M.H Sohn, "Characteristics of a Persistent Current Compensator for Superconducting NMR Magnets using Linear Type Magnetic Flux Pump," *ASC-2004*, *Florida USA*, no. 3LS06, Oct. 2004.
3. Tsutomu Hoshino, **Yoondo Chung**, Taketsune Nakamura, Takashi Teramoto, Itsuya Muta and Tae Kuk Ko, "Pumping Current Rate of Linear-Type Magnetic Flux Pump," *Asian Conference on Applied superconductivity and Cryogenics 2004*, *Miyazaki Japan*, Dec. 2004.
4. Tsutomu Hoshino, **Yoondo Chung**, Itsuya Muta, Taketsune Nakamura and Tae Kuk Ko, "Theoretical Analysis of Pumping Current in the Linear Type Magnetic Flux Pump," *Korea-Japan Seminar on 'large scale application of superconductivity science and technology'*, *Miyazaki Japan*, pp. 37, Dec. 2004.
5. Taketsune Nakamura, **Yoondo Chung** and Tsutomu Hoshino, "Magnetic Behavior of Superconducting Foil Utilized for Linear-Type Magnetic Flux Pump," *International Symposium on Electromagnetic Fields in Electrical and Electronic Engineering*, *Spain*, Sept. 2005.
6. **Yoondo Chung**, Tsutomu Hoshino and Taketsune Nakamura, "Current Pumping Performance of Linear-type Magnetic Flux Pump with Use of Feedback Control Circuit System," *19th International Conference on Magnet Technology*, *Genova Italy*, no. MOA04PO06, Sept. 2005.

Domestic Conference

1. **Yoondo Chung**, Itsuya Muta, Tsutomu Hoshino and Taketsune Nakamura, "Preparatory FEM Analysis of a Linear Type Magnetic Flux Pump for Compensating a Little Decremental Persistent Current of HTS Magnets," *Kansai-Section Joint Convention of IEEJ*, *Osaka Japan*, G4-7, pp. G123, Nov. 2002.
2. **Yoondo Chung**, Itsuya Muta, Tsutomu Hoshino and Taketsune Nakamura, "Magnetic Field Distributions of a Linear Type Magnetic Flux Pump to Compensate a Little Decremental Persistent Current of HTS Magnets for NMR using FEM," *2003 National Convention IEEJ*, *Sendai Japan*, vol. 5, no. 5-199, pp. 278-279, March 2003.
3. **Yoondo Chung**, Itsuya Muta, Tsutomu Hoshino and Taketsune Nakamura, "Characteristics of Current Compensator for Persistent Current in NMR Magnets with Use of Linear Type Magnetic Flux Pump," *2004 National Convention IEEJ*, *Sagamihara Japan*, vol. 5, no. 5-038, pp. 44-45, March 2004.
4. **Yoondo Chung**, Itsuya Muta, Tsutomu Hoshino, Hun-June Jung and Taketsune Nakamura, "Test of Linear Type Magnetic Flux Pump for Compensating Persistent Current in Superconducting Magnets under Pre-charged Operational Current," *70th Meeting on Cryogenics and Superconductivity CSJ-2004*, *Yokohama Japan*, vol. 70, no. 1E-p21, pp. 75, May 2004.
5. **Yoondo Chung**, Takashi Teramoto, Itsuya Muta, Tsutomu Hoshino, Hun-June Jung and Taketsune Nakamura, "Test for Compensating Persistent Current of Superconducting Magnets using Linear Type Magnetic Flux Pump under Various Frequencies of AC Current," *Technical Meeting on Application of Superconductivity IEEJ*, *Yokosuka Japan*, ASC-04-47, pp. 19-24, June 2004.